DESIGN OF AN YTTERBIUM-169 BRACHYTHERAPY SOURCE FOR GOLD NANOPARTICLE-AIDED RADIATION THERAPY

A Dissertation
Presented to
The Academic Faculty

By

Francisco J. Reynoso

In Partial Fulfillment
of the Requirements for the Degree
Doctor of Philosophy in the
The George W. Woodruff School of Mechanical Engineering

Georgia Institute of Technology
August 2014

DESIGN OF AN YTTERBIUM-169 BRACHYTHERAPY SOURCE FOR GOLD NANOPARTICLE-AIDED RADIATION THERAPY

Approved by:

Dr. Sang Hyun Cho, Advisor
School of Mechanical Engineering,
NRE/MP Department
Georgia Institute of Technology

Dr. C.-K. Chris Wang, Co-advisor
School of Mechanical Engineering,
NRE/MP Department
Georgia Institute of Technology

Dr. Eric Elder
Department of Radiation Oncology
Emory School of Medicine

Dr. Chaitanya S. Deo
School of Mechanical Engineering,
NRE/MP Department
Georgia Institute of Technology

Dr. Younan Xia
School of Biomedical Engineering
Georgia Institute of Technology

Date Approved: April 28, 2014

ACKNOWLEDGEMENTS

I would like to express my deepest appreciation to my advisor and mentor, Dr. Sang Hyun Cho, for taking a chance on me and giving me the opportunity to work with him. His guidance and persistent support were instrumental in completing the work presented here. I am also grateful to my lab mate, roommate and friend, Nivedh Manohar for all of his helpful discussion and advice, and providing the NOREC calculations necessary to complete my work. I would also like to extend my gratitude to Dr. Bernard "Tripp" Jones and all previous members of the lab for laying the groundwork and giving me the tools necessary to make this work possible. I acknowledge funding support from the DOD/PCRP grant W81XWH-12-1-0198.

I would like to express my sincere gratitude to my co-advisor Dr. C.-K. Chris Wang and the rest of the reading committee, Dr. Eric Elder from Emory University, and Dr. Chaitanya S. Deo and Dr. Younan Xia from Georgia Tech, for volunteering their time and their suggestions for completing my dissertation. I would also like to thank Dr. Gavin Poludniowki from the University of Surrey for providing the SpekCalc software.

To my dear, Dr. Sarah Bryan Reynoso, thank you for your continuous words of encouragement, love and support. Together we have been on a nine year journey that has entailed five states, four universities, and thousands of miles; this work represents a successful end to that journey. Thank you. A mi mamá, Neldys, gracias por todos tus sacrificios y enseñanzas; tu apoyo incondicional es esencial para todos mis logros. Te amo. To my brothers, Angel and Alfredo, thank you for your never-ending support and inspiration.

TABLE OF CONTENTS

Acknowledgements iii

List of Tables vi

List of Figures vii

List of Abbreviations x

List of Symbols xi

Summary xiii

Chapter 1 Introduction 1

1.1 Gold Nanoparticles in Cancer Therapy 1

1.2 Gold Nanoparticles and Radiation Dose Enhancement 2

1.3 Ytterbium-169 4

1.4 Overview of the Research 5

Chapter 2 Ytterbium-169 Source Encapsulation Design 7

2.1 Yb-169 Source Design 7

2.2 Monte Carlo Model 9

2.3 Photon Spectra from Various Encapsulation Designs 12

2.4 Macroscopic Dose Enhancement Factors 14

2.5 Correlation between MDEF and Spectral Characteristics of Each Source 16

2.6 Secondary Electron Spectra and Microscopic Dose Enhancement 19

2.7 Discussion 25

Chapter 3 TG-43 Characterization of Ytterbium-169 Sources 29

3.1 TG-43 Formalism for Brachytherapy Dose Calculation 29

3.1.1 Air-Kerma Strength 31

3.1.2 Dose-Rate Constant 31

3.1.3 Geometry Function 32

3.1.4 Radial Dose Function 32

3.1.5 Anisotropy Function 33
3.2 Monte Carlo Calculation 33
3.3 Results and Discussion 37
Chapter 4 Monte Carlo Model of A Phillips RT-250 Orthovoltage Machine 42
4.1 Monte Carlo Model 43
4.2 Experimental Validation of Photon Spectrum 45
4.3 Experimental Validation of Percent Depth Dose 53
Chapter 5 Ytterbium-169 Source Emulation 62
5.1 Photon Spectrum Approximation 62
5.2 Percent Depth Dose Comparison 68
5.3 Secondary Electron Spectra 70
5.4 Discussion 73
Chapter 6 Conclusions 75
Appendix A PhotoElectron Spectra 78
Appendix B Reconstructed Incident Spectra of Phillips RT-250 Orthovoltage Machine 80
References 82

LIST OF TABLES

Table 2.5.1 Spectral and dose enhancement characteristics of the different Yb-169 encapsulation designs. The results show direct correlation between MDEF and spectral characteristics of each source design. 17

Table 2.6.1 Total yield of photoelectrons (PE) and Auger/Coster-Kronig electrons (AE) and intensity-weighted total energy from gold and tissue for a tumor loaded with 7 mg Au/g of tissue for each encapsulation design. Auger/Coster-Kronig electrons are only produced in gold. All values listed in the table are normalized per source photon. 23

Table 3.2.1 Yb-169 photon spectrum including all photons with yields greater than 0.1 % and ignoring all dosimetrically irrelevant gamma rays below 5 keV. 33

Table 3.3.1 Calculated geometry function $G_L(r,\theta)$ for both Ti-6Al-4V titanium and 304 stainless steel source encapsulation designs. 38

Table 3.3.2 Radial dose function $g_L(r,\theta)$ values for the Ti-6Al-4V titanium and 304 stainless steel source designs. 39

Table 3.3.3 2D Anisotropy function $F(r,\theta)$ values for the Ti-6Al-4V titanium design. 40

Table 3.3.4 2D Anisotropy function $F(r,\theta)$ values for the 304 stainless steel design.... 40

Table 5.1.1 Available beams from the Phillips RT-250 orthovoltage machine. 62

Table 5.3.1 Total yield of photoelectrons (PE) and Auger/Coster-Kronig electrons (AE) and intensity-weighted total energy from gold and tissue for a tumor loaded with 7 mg Au/g of tissue for each separate beam. Auger/Coster-Kronig electrons are only produced in gold. All values listed in the table are normalized per source photon. 71

LIST OF FIGURES

Figure 2.1.1 Yb-169 source geometries for MCNP simulations. LEFT: Single encapsulation geometry with capsule made of 6061 aluminum, Ti-6Al-4V titanium or 304 stainless steel. RIGHT: Double encapsulation geometry with inner 6061 aluminum capsule and external Ti-6Al-4V titanium capsule. This model adds a 0.025 cm thick outer titanium shell to the inner aluminum capsule. All dimensions are shown in centimeters. 8

Figure 2.2.1 MCNP geometry which consists of the brachytherapy source centered on a 30 cm spherical phantom. The tumor region is defined as a 3.5 cm-radius sphere centered on the larger phantom. Concentric square (0.1 cm × 0.1 cm) annuli serve as tally regions to compute the radial dose distribution along the transverse plane of the source..... 9

Figure 2.2.2 Yb-169 photon energy spectrum histogram from Ref. 45 simplified to include only those gamma rays with intensity yields that are greater than 0.01% and ignoring all dosimetrically irrelevant gamma rays below 10 keV. 10

Figure 2.3.1 Photon spectra comparing absorption through different source filter materials. The intensity-weighted average energy of each spectrum before and after being filtered by encapsulation material reflects the differences in spectral hardening for each design. 14

Figure 2.4.1 The calculated macroscopic dose enhancement factors for various encapsulation materials of the Yb-169 source as a function of radial distance along the transverse axis of the source. 15

Figure 2.5.1 MDEF 1 cm away from the source as a function of source design. The percentage of photons between 10 keV and 110 keV are shown in the same graph to demonstrate a strong correlation between the two. 18

Figure 2.6.1 Spectrum of photoelectrons released in the tumor region for the Ti-6Al-4V titanium encapsulation design. The figure shows the spectrum from gold and tissue for the tumor loaded with 7 mg Au/g tissue and from tissue only. 21

Figure 2.6.2 Spectrum of photoelectrons released in the tumor region for the 304 stainless steel encapsulation design. The figure shows the spectrum from gold and tissue for the tumor loaded with 7 mg Au/g tissue and from tissue only. 21

Figure 2.6.3 LEFT: Spectrum of photoelectrons released in the tumor region from gold and tissue for a tumor loaded with 7 mg Au/g of tissue for the 304 stainless steel and the Ti-6Al-4V titanium encapsulation design. RIGHT: Low energy region below 100 keV. 22

Figure 2.6.4 Microscopic dose enhancement factor (mDEF) for the Ti-6Al-4V titanium and 304 stainless steel source encapsulation designs for Yb-169. 25

Figure 3.1.1 Geometry and coordinate system used to define the TG-43 dose calculation formalism for brachytherapy sources from Ref. 53. 30

Figure 3.2.1 MCNP tally geometry for computing the air kerma strength at $\theta_o = 90^o$ and $d = 100\ cm$. The source is centered on a spherical region *in vacuo* with a radius of *130 cm.* 34

Figure 3.2.2 MCNP tally geometry for computing the dose distribution around the Yb-169 source. 37

Figure 3.3.1 Calculated radial dose function for the Ti-6Al-4V titanium source design and 5th degree polynomial fit along with corresponding fitting parameters. 39

Figure 3.3.2 2D Anisotropy function $F(r,\theta)$ at $r = 0.5\,cm$ for both source encapsulation designs..... 41

Figure 4.1.1 MCNP geometry for Phillips RT-250 orthovoltage machine model. LEFT: Cross-sectional view of machine head model. Geometry includes vacuum region, beryllium exit window, copper and lead cone collimators, and square lead collimators. RIGHT: Three-dimensional view of the MCNP geometry used for simulation showing the position of the water phantom at 50 cm SSD..... 44

Figure 4.2.1 Detector geometry for measurements of the incident spectra of the Phillips RT-250 orthovoltage machine. 46

Figure 4.2.2 X-ray detection system for photon spectra measurements. 47

Figure 4.2.3 Full energy absorption peak efficiency of Amptek AXR CdTe detector. ... 48

Figure 4.2.4 Measured 90^o spectrum and reconstructed incident spectrum for the 250 kVp beam filtered by 0.25 mm Cu..... 51

Figure 4.2.5 Photon spectrum validation of 250 kVp beam. 52

Figure 4.2.6. Photon spectrum validation of 125 kVp beam. 52

Figure 4.2.7 Photon spectrum validation of 75 kVp beam**.** 53

Figure 4.3.1 Dose calibration curve for the 250 kVp beam for all three color channels. 56

Figure 4.3.2 Dose sensitivity curve for the 250 kVp beam for all three color channels.. 57

Figure 4.3.3 Percent depth dose validation for 250 kVp beam. MC results are compared against film and chamber measurements. 58

Figure 4.3.4 Percent depth dose validation for 125 kVp beam. MC results are compared against film and chamber measurements. 61

Figure 4.3.5 Percent depth dose validation for 75 kVp beam. MC results are compared against film and chamber measurements. 61

Figure 5.1.1 Photon spectrum and intensity-weighted average energy for all available beams from the Phillips RT-250 orthovoltage machine. 63

Figure 5.1.2 Photon spectrum of 250 kVp (Cu) compared to the same beam after the addition of a 0.25 mm erbium filter. The strong characteristic lines of tungsten on the original beam are suppressed and replaced with those of erbium at 49.1 keV and 55.7 keV. 65

Figure 5.1.3 Photon spectrum of 250 kVp (Cu) after the addition of a 0.25 mm erbium filter compared to the photon spectra of Yb-169. The fluorescence photons from erbium at 49.1 keV and 55.7 keV match the strongest part of the Yb-169 spectrum. 66

Figure 5.1.4 Photon spectrum of the Er-filtered 250 kVp calculated by MC results compared to measured results reconstructed from 90^{o} Compton scattering. 67

Figure 5.2.1 Percent depth dose comparison for all available beams from the Phillips RT-250 machine as well as a hypothetical Yb-169. 68

Figure 5.2.2 Percent depth dose data for the Cu-filtered 250 kVp beam and the Er-filtered 250 kVp beam. 69

Figure 5.3.1 Spectra of photoelectrons released in the tumor region for each photon beam. The figure shows the spectrum from gold and tissue for the tumor loaded with 7 mg Au/g tissue. 71

LIST OF ABBREVIATIONS

PTV	Planning target volume
OAR	Organs at risk
IMRT	Intensity-modulated radiation therapy
IGRT	Image-guided radiation therapy
GNPs	Gold nanoparticles
EPR	Enhanced permeability and retention
GNRT	Gold nanoparticle-aided radiation therapy
MC	Monte Carlo
AAPM	American Association of Physicists in Medicine
TG	Task Group
PDD	Percent depth dose
HDR	High dose rate
MCNP	Monte Carlo N-particle code
ICRU	International Commission on Radiation Units of Measurements
MDEF	Macroscopic dose enhancement factor
EGS	Electron gamma shower
mDEF	Microscopic dose enhancement factor
SSD	Source-to-surface distance
MCA	Multichannel analyzer
TIFF	Tagged image file format
netOD	Net optical density

LIST OF SYMBOLS

Z	Atomic Number
Au	Gold
τ	Photoelectric cross section
E	Energy
Yb	Ytterbium
I	Iodine
Pd	Palladium
Ir	Iridium
Yb_2O_3	Ytterbium oxide
Tm	Technetium
Er	Erbium
nm	Nanometer
keV	Kilo electron-volt
kVp	Peak kilovoltage
Ci	Curie
mm^3	Cubic millimeter
A_{app}	Apparent Activity
Be	Beryllium
Cu	Copper
Pb	Lead
W	Tungsten
Ti	Titanium
Al	Aluminum
CdTe	Cadmium telluride
CdZnTe	Cadmium Zinc Telluride
HP-Ge	High purity Germanium
C	Carbon

In	Indium
Pt	Platinum
c	Speed of light in vacuum
Mo	Molybdenum
Rh	Rhodium

SUMMARY

Gold nanoparticles can serve as an ideal radiosensitizer for radiation therapy due to the high-atomic-number nature of gold and the increased tumor specificity in nanoparticle form. The degree of radiosensitization is highly dependent on both the local gold nanoparticle concentration in the tumor and the radiation source type. Previous Monte Carlo simulations have demonstrated that the gamma-ray energy spectrum of Ytterbium-169 is a strong candidate for a high dose rate brachytherapy implementation of gold nanoparticle-aided radiation therapy. Therefore, the current study focuses on the design of a high dose rate Ytterbium-169 source that would maximize dose enhancement during gold nanoparticle-aided radiation therapy; while meeting the practical constraints for the production of a clinically relevant brachytherapy source. Different encapsulation materials are studied in order to determine its effect on the dosimetric characteristics of the source. Specifically, the photon spectra, secondary electron spectra, and dose enhancement characteristics are calculated via Monte Carlo simulations to elucidate the effects on potential radiosensitization during gold nanoparticle-aided radiation therapy. Furthermore, this project involves a study into the modification of external x-ray beams from a Philips RT-250 orthovoltage x-ray machine in an attempt to match the dosimetric characteristics of the Ytterbium-169 brachytherapy source. This investigation will enable the production of an external beam that can serve as a good surrogate of an actual brachytherapy source and facilitate the pre-clinical investigation of gold nanoparticle-aided radiation therapy with Ytterbium-169.

CHAPTER 1

INTRODUCTION

1.1 Gold Nanoparticles in Cancer Therapy

Radiation therapy remains one of the most effective tools used for battling the numerous types of cancers. Radiation therapy techniques vary by radiation type (e.g. photons, electrons, protons, or heavy ions), application method (e.g. external beam vs. brachytherapy), and energy of the radiation source. Each type of radiation treatment has unique advantages and shortcomings that dictate the selection of a specific treatment modality and/or technique for a given clinical situation. Regardless of treatment modalities and techniques, the ultimate goal of radiation therapy remains the same; to maximize the dose delivered to the planning target volume (PTV) while keeping the dose to the organs at risk (OAR) at a minimum. This goal has traditionally been accomplished through improvements in treatment planning, radiation source equipment, and/or delivery techniques (e.g. intensity modulated radiation therapy (IMRT), image guided radiation therapy (IGRT), brachytherapy). The recent development of nanomaterials has provided an array of new tools with powerful medical applications and consequently given rise to nanomedicine, the medical application of such nanomaterials, as an important field of clinical research and development. Gold (Au) nanoparticles (GNPs) are one class of nanomaterials currently under active investigation for biomedical applications. GNPs can be synthesized in a wide variety of shapes (e.g. gold nanospheres, nanorods, nanoshells, and nanocages) and possess properties that can be exploited in medicine with powerful clinical implications.

The unique properties of nanoparticles have made GNPs an attractive choice for a wide assortment of medical applications that range from drug delivery [1], cancer imaging [2-4], thermal therapy [5-8], and radiation therapy [9-14]. The gold composition makes GNPs biologically compatible and allows for conjugation to a variety of biomarkers that enables active targeting in solid tumors [3]. Furthermore, as a key characteristic of all nanostructures, the small size of GNPs allows for selective accumulation in tumors via passive extravasation of GNPs through leaky tumor vasculature [15] because the size (1~100 nm) is smaller than the typical cutoff size (~400 nm) of pores within tumor vasculature [16]. This effect is commonly known as the enhanced permeability and retention (EPR) effect [17], and allows for passive targeting of tumors. The high-atomic number (Z) of gold (Z=79) and increased tumor specificity of GNPs make them an ideal radiosensitizing agent for what is now called gold nanoparticle-aided radiation therapy (GNRT). The high-Z of GNPs drastically alters the photon interaction probability within tumors, resulting in a clinically meaningful enhancement of the dose delivered to tumors.

1.2 Gold Nanoparticles and Radiation Dose Enhancement

Dose enhancement due to altered interaction probabilities of tissues was first observed in dose measurements during contrast agent imaging studies [18]. Since then, multiple efforts of dose enhancement through the use of high-Z materials have been put forth, but such efforts have mainly focused on iodine and gadolinium agents during kilo- and mega-voltage x-ray irradiation [19-26]. The key physical mechanism that greatly enhances the delivered dose with high-Z materials is the increased photoelectron

production within the tumor site. This effect comes as a direct result of the relationship among photoelectric absorption cross section, the energy of photons, and the atomic number of the target as described by:

$$\tau/\rho \propto Z^3/E^3 \tag{1.1.1}$$

This relationship highlights the prominent increase in photoelectron production with an increase in the atomic number or a decrease in the energy of the incident photon. Considering the higher atomic number of gold and the greater tumor specificity of gold in nanoparticle form, the use of GNPs for the purpose of dose enhancement is expected to be far more effective than previous attempts. The efficacy of GNP-mediated dose enhancement during radiation therapy was first demonstrated during animal studies using 250 kVp irradiation [11]. This study showed pronounced tumor regression and increased long-term survival for mice treated with GNPs as compared to those treated without. Furthermore, the rationale for GNRT has also been demonstrated to be more effective at treating radio-resistant tumors such as squamous cell carcinoma in mice [10].

The dose enhancement due to GNRT has also been quantified by numerous Monte Carlo (MC) studies [12-14, 27], showing that the dose enhancement characteristics of GNRT are not only dependent on the gold concentration within tumors, but also heavily dependent on photon beam quality. These studies conclude that dose enhancement may exceed several hundred percent for lower energy radiation sources (e.g. keV range photons). The dose enhancement due to the presence of GNPs is a direct result of the pronounced increase of photoelectric absorption in the tumor as specified by equation 1.1.1. Consequently, the increase in photoelectric absorption leads to an increase of up to two orders of magnitude in the number of photoelectrons and Auger/Coster-

Kronig electrons produced [13]. The extent of this increase and the subsequent dose enhancement is directly related to the energy spectrum of the photon source. Therefore, in order to maximize the dose enhancement effect of GNRT, the photon source spectrum and source design must be chosen carefully. Low-to-intermediate energy brachytherapy sources such as Palladium (Pd)-103, Iodine (I)-125, Ytterbium (Yb)-169, and Iridium (Ir)-192 are regarded as suitable sources for GNRT as such sources primarily produce photons in the keV range. Previous MC studies [13, 14] have investigated the dosimetric characteristics of each source type and demonstrated that a high-dose rate (HDR) Yb-169 brachytherapy source would be the best suited for GNRT. The intensity-weighted average energy of a bare Yb-169 source is about ~93 keV, just above the K-edge of gold but much lower than other HDR sources such as Ir-192 (~395 keV). Moreover, low-dose rate sources such as I-125 or Pd-103 would require multiple injections of GNPs or a sustained release of GNPs to induce the desired level of dose enhancement [13, 28], which makes the approach impractical for clinical translation.

1.3 Ytterbium-169

Yb-169 is produced in a nuclear reactor by neutron activation of Yb-168 in ytterbium oxide (Yb_2O_3) powder via Yb-168(n,γ)Yb-169, and decays with a half-life of 32 days by electron capture to stable thulium (Tm)-169. Yb-168 has a natural abundance of just 0.13 %, but the high thermal neutron capture cross-section and its availability in enriched form ($\gtrsim$ 20 %) allow for very high specific activity of up to 10 Ci/mm^3[29-31]. As a result, Yb-169 is appropriate for HDR brachytherapy applications and various designs of Yb-169 sources have been described in the published literature [29-39]. The

relatively low energy photon spectrum of Yb-169 is not only attractive for dose enhancement during GNRT, but would also add multiple advantages including the possibility of *in-vivo* shielding of essential organs and tissues, reduced radiation exposure to personnel, simplified HDR room shielding, streamlined after-loading units, and overall reduced costs [29-34, 37, 39]. Nevertheless, an Yb-169 brachytherapy source is neither commercially available in North America at the time nor has its design been carefully studied for the purpose of GNRT. Therefore, the current studies are aimed at the design of an Yb-169 source that would maximize the dose enhancement during GNRT while also meeting practical constraints for manufacturing a clinically-relevant brachytherapy source.

1.4 Overview of the Research

The research presented herein is based on various tasks aimed at the design and pre-clinical study of an Yb-169 brachytherapy source that would maximize dose enhancement during GNRT. The design must meet the practical constraints for producing a brachytherapy source appropriate for clinical translation while simultaneously being optimized for GNRT. The first task involves the encapsulation design of the Yb-169 source to ensure that the low energy portion of the photon spectrum is preserved for maximal dose enhancement. The designs are evaluated based on MC simulations of the resulting photon spectra, secondary electron spectra, and dose enhancement characteristics. The second task consists of the characterization of the optimized brachytherapy source via MC techniques to compute the American Association of Physicists in Medicine (AAPM) Task Group (TG)-43 dosimetric parameters: anisotropy

function, radial dose function, air kerma strength, and dose rate constant. The third task is to develop an MC model to modify a Phillips RT-250 orthovoltage x-ray beam to emulate the dosimetric characteristics of the Yb-169 brachytherapy source. The modified beam is to be evaluated using the resulting photon spectra, secondary electron spectra, and dose enhancement characteristics. The fourth task consists of validating the MC model of the Phillips RT-250 machine by comparing MC results with measured photon spectra and percent depth dose (PDD). The combination of these tasks will provide a thorough characterization of an HDR Yb-169 brachytherapy source optimized for GNRT, as well as a modified orthovoltage beam to emulate the Yb-169 source that can facilitate the pre-clinical study to investigate the efficacy of GNRT with the Yb-169 source.

CHAPTER 2

YTTERBIUM-169 SOURCE ENCAPSULATION DESIGN

2.1 Yb-169 Source Design

This investigation was conducted using a number of variations of an Yb-169 brachytherapy source design. The basic source design was modeled after a commercially available HDR Ir-192 source as used in previous studies [12, 40] and similar to that of an existing HDR Yb-169 source [37, 41, 42]. The source geometry was designed with an active source length of 3.5 mm, a diameter of 0.6 mm, and four different encapsulation designs as shown in Figure 2.1.1. The first three designs were all single capsule designs with three different capsule materials in alloy form: 6061 aluminum, Ti-6Al-4V (grade 5) titanium, and 304 stainless steel. The last design was a dual-capsule design with an inner aluminum capsule and an outer titanium capsule similar to that of an Yb-169 source developed for industrial applications [43]. The inner aluminum capsule allows for proper and safe encapsulation of Yb_2O_3 during neutron activation. The irradiated aluminum capsules containing the neutron-activated source can then be sealed in an outer titanium capsule to ensure a higher degree of safety and better means by which to attach to the source holder [44]. It should be noted that the aluminum encapsulation design is not a clinically relevant design because aluminum is not biocompatible and lacks the required strength to safely encapsulate the radioactive core; nevertheless this design was included to benchmark the characteristics of an idealized source encapsulation model in terms of photon transmission and filtration.

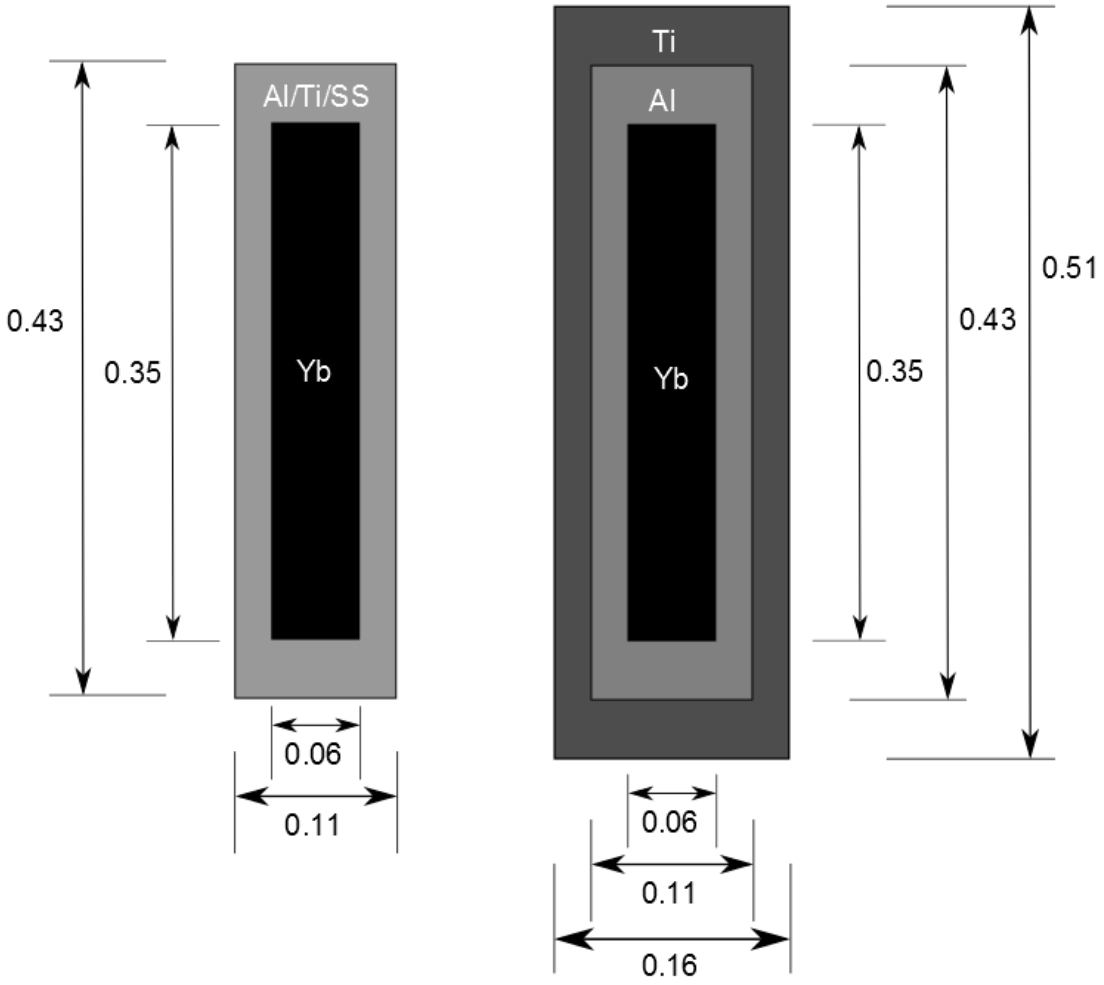

Figure 2.1.1 Yb-169 source geometries for MCNP simulations. LEFT: Single encapsulation geometry with capsule made of 6061 aluminum, Ti-6Al-4V titanium or 304 stainless steel. RIGHT: Double encapsulation geometry with inner 6061 aluminum capsule and external Ti-6Al-4V titanium capsule. This model adds a 0.025 cm thick outer titanium shell to the inner aluminum capsule. All dimensions are shown in centimeters.

2.2 Monte Carlo Model

In order to appropriately discriminate between source designs for GNRT, MC simulations were completed to determine changes to the gamma-ray energy spectrum of the bare source caused by the encapsulation design. The macroscopic dose enhancement factor (MDEF), defined as the ratio of the average dose in the tissue/tumor region with and without the presence of GNPs, is also used as an added tool to evaluate each source design.

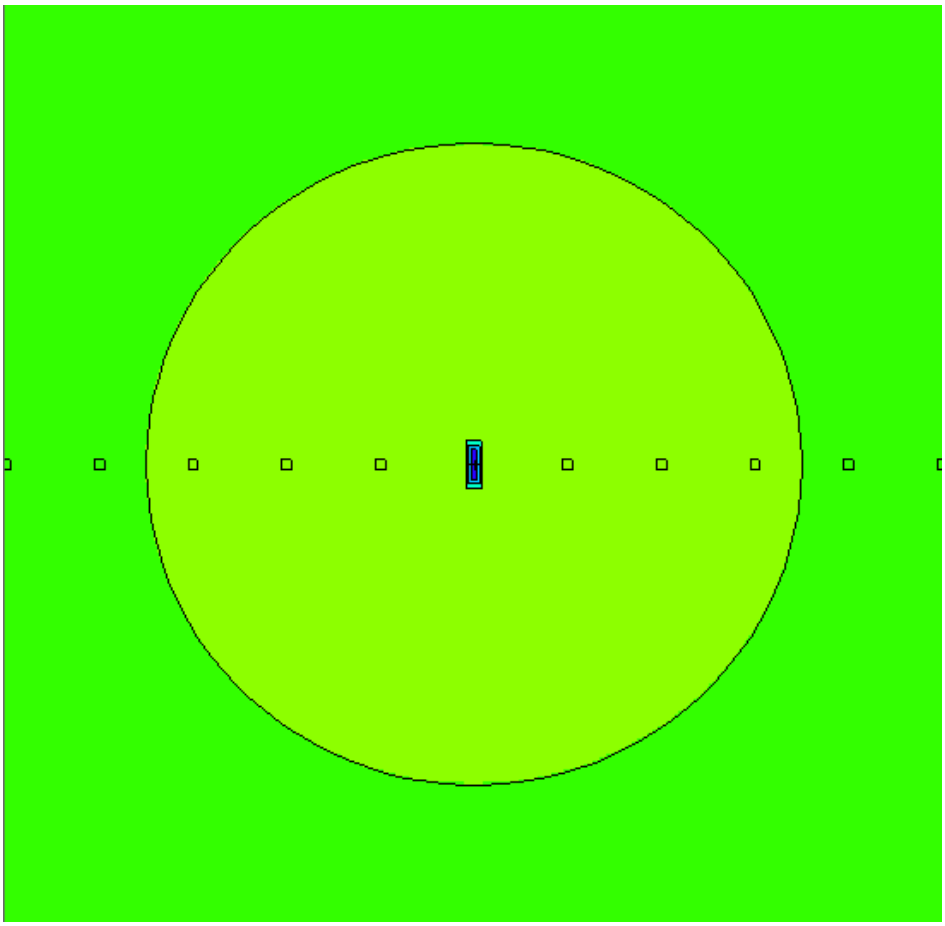

Figure 2.2.1 MCNP geometry which consists of the brachytherapy source centered on a 30 cm spherical phantom. The tumor region is defined as a 3.5 cm-radius sphere centered on the larger phantom. Concentric square (0.1 cm × 0.1 cm) annuli serve as tally regions to compute the radial dose distribution along the transverse plane of the source.

The phantom geometry and material composition are similar to those used in previous studies [12, 13] and represent the typical geometry used for MC characterization of brachytherapy sources (Figure 2.2.1). The geometry consists of a source located at the center of a 30 cm in radius spherical phantom. The tumor region for all source designs is taken as a 3.5 cm radius sphere centered at the origin of the larger sphere and excluding the source region. The source region was centered in the phantom where the geometry and material composition matched those specified in Figure 2.1.1. The intricate photon spectrum of Yb-169 of 62 gamma rays and 20 x-ray emission lines [45] was simplified as shown in Figure 2.2.2, by only taking into account photons with intensities greater than 0.1% and ignoring dosimetrically irrelevant gamma rays below 10 keV. The intensity-weighted average energy of this spectrum is just 92.7 keV.

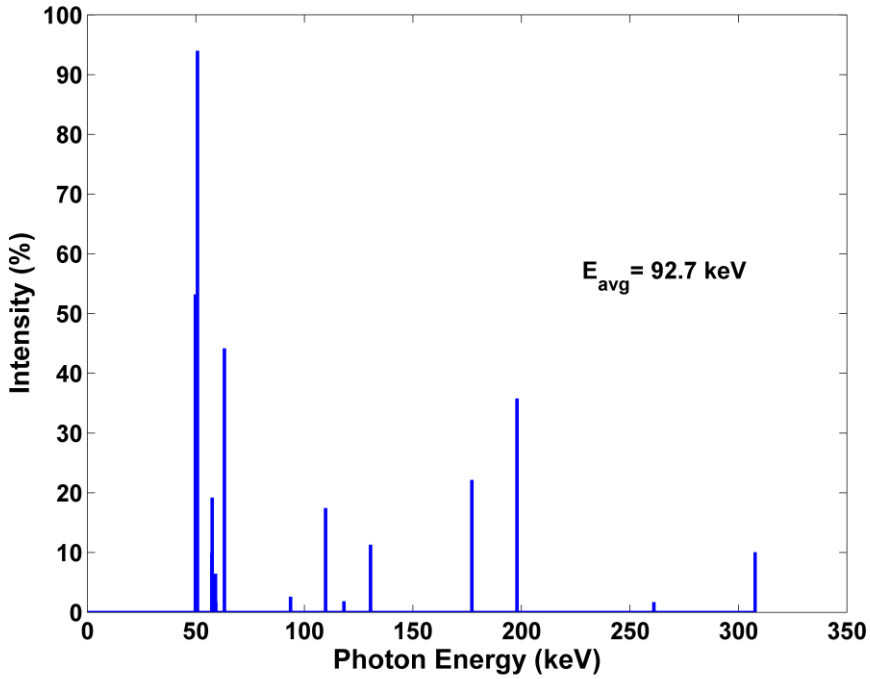

Figure 2.2.2 Yb-169 photon energy spectrum histogram from Ref. 45 simplified to include only those gamma rays with intensity yields that are greater than 0.01% and ignoring all dosimetrically irrelevant gamma rays below 10 keV.

The composition of the phantom and tumor was taken as that of four-component tissue: 10.1% hydrogen, 11.1% carbon, 2.6% nitrogen, and 76.2% oxygen, as defined by the International Commission on Radiation Units and Measurements (ICRU) [46]. The GNP-loaded tumors were replaced by the ICRU four-component tissue and GNPs at a concentration of 7 mg Au/g of tissue. This concentration was chosen based on previous animal studies [11] performed with 1.9 nm-diameter GNPs. The level of GNP-loading was not changed during the current work as the study was focused on the dose enhancement differences produced by each source design. The density of the GNP-loaded tissue was increased to reflect the added mass of the tissue from 1 g/cm^3 to 1.007 g/cm^3. The GNP-loaded tissues were assumed to contain a uniform distribution of GNPs with no physical interface between gold and tissue by applying a uniform mixture model. The model approximates a uniform distribution of GNPs with a uniform distribution of gold atoms among the atoms of other tissue elements. This approximation is not a realistic representation of GNP-loaded tissues but it is deemed practical and reasonable for MC estimates in the current comparative study of source encapsulation.

The MC calculations for all the source designs were performed with the Monte Carlo N-Particle Code version 5 (MCNP5) [47]. The default cross-sections of the MCNP5 system were used to generate particle interaction cross-sections for the gold-loaded tissues. Photon-transport was the only mode used for the MCNP5 calculations because the effect of electron transport is insignificant for the spectral and dose calculations performed in the current study. Photon histories were traced down to 1 keV, the default cutoff energy by the MCNP5 code. The radial dose distributions along the transverse axis of the source between 1 and 10 cm were collected using concentric annuli

(cross-sectional dimensions of 0.1 cm high and 0.1 cm wide) using the MCNP5 energy deposition F6 tally. The photon flux on the surface of the active source region (i.e. surface of Yb-169 source region) and on the surface of the capsule (i.e. past the encapsulation material) was collected using the average surface flux F2 tally as a function of photon energy in 0.5 keV bins. 1×10^9 particle histories were simulated, and the statistical uncertainty (1σ) was less than 0.1 % for all radial dose tally results. The statistical uncertainty was less than 0.1 % for all surface flux tally results for bins with a photon yield greater than 0.1 %. The intensity-weighted average energy of each spectrum was calculated as:

$$E_{avg} = \frac{\sum_{i=1}^{n} \varphi_i E_i}{\sum_{i=1}^{n} \varphi_i} \tag{2.2.1}$$

where E_i is the energy of the flux tally φ_i for the i^{th} bin computed by MCNP5. Additional details about the MC simulation and MCNP5 code can be found elsewhere [40, 47].

2.3 Photon Spectra from Various Encapsulation Designs

The MC results reflect the importance of careful consideration of the source design for a brachytherapy implantation of GNRT. The effects of source design can substantially alter the gamma-ray energy spectrum from the source and in turn lower the efficacy of dose enhancement through GNRT. The spectral variations arise due to the differences in effective atomic number and total thickness of the capsule that houses the active source region. The original Yb-169 photon spectrum shown in Figure 2.2.1 is hardened substantially due to self-absorption within the ytterbium region and subsequently through interaction with the capsule material. The original photon spectrum of Yb-169 has an intensity-weighted average energy of 92.8 keV with about 80 % of the

photons with energies below 100 keV. The MC results show strong spectral hardening through photon absorption within the source and capsule material. This is expected as photoelectric absorption is the dominant photon interaction mechanism within this energy regime for most materials and especially those used in the source design. The photon spectrum tallied on the surface of the active source length shows significant spectral hardening of 30 % when compared to the spectrum shown in Figure 2.2.1 with an average energy of 107.6 keV. This photon spectrum, unfiltered by the encapsulation material, is shown in Figure 2.3.1 and is referred to as the "unfiltered spectrum". This photon spectrum can change substantially based on the dimensions of the active core as self-absorption hardens the spectrum when the size increases.

Figure 2.3.1 shows the photon spectra and intensity-weighted average energy for each of the different source designs. The spectral characteristics that are important to note are not only the spectral hardening, but also the decreased fluence after filtration through the encapsulation material. Aluminum, with an atomic number of 13, showed spectral hardening of just 1.2 % with an average energy of 108.9 keV and a total transmission of 32 %. This was the smallest increase in average energy and the largest transmission of all the designs tested. This is expected from the aluminum source and demonstrates the change spectral characteristics of the source under optimal conditions. The titanium capsule showed a spectral hardening of 5.0 % with an average energy of 113.0 keV and a total transmission of 29 %. The dual-capsule design of aluminum and titanium showed a spectral hardening of 4.4 % with an average energy of 112.3 keV, but the added thickness of the dual-capsule design caused the total transmission to be just 16%. The stainless

steel design had the strongest spectral hardening of 14 % with a total transmission of 25 %.

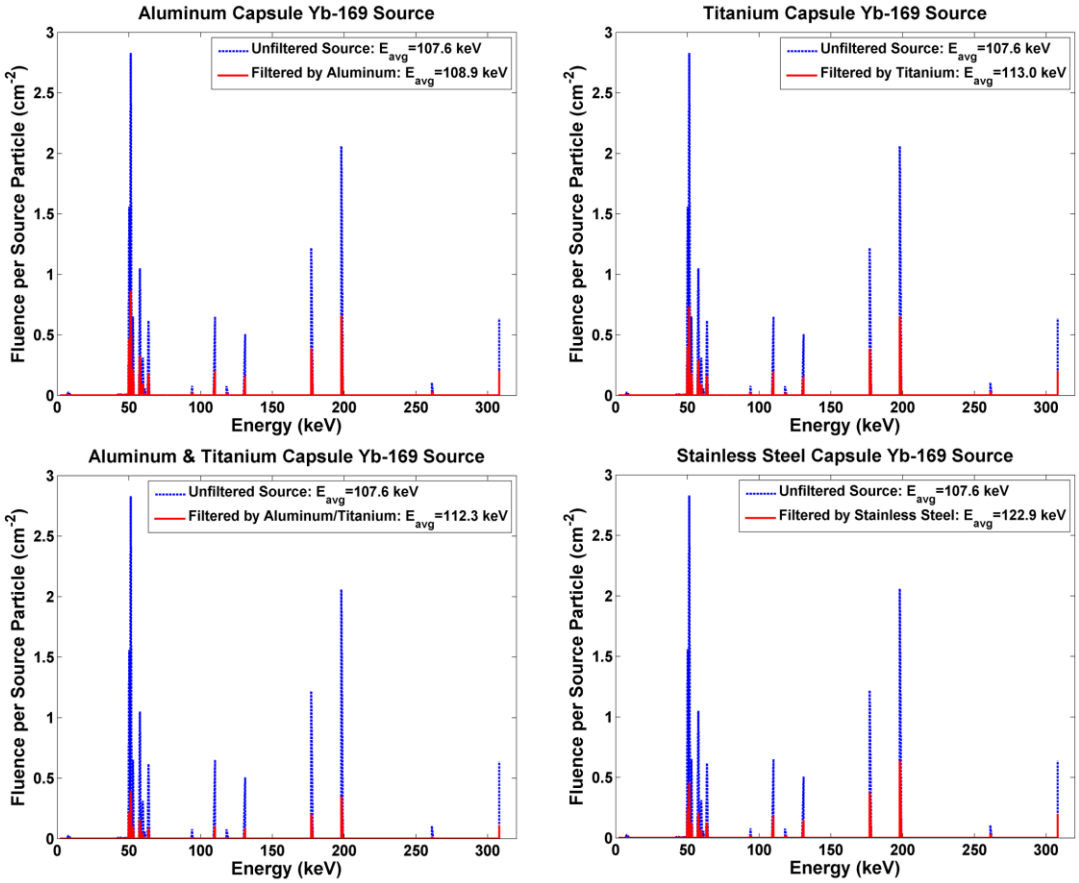

Figure 2.3.1 Photon spectra comparing absorption through different source filter materials. The intensity-weighted average energy of each spectrum before and after being filtered by encapsulation material reflects the differences in spectral hardening for each design.

2.4 Macroscopic Dose Enhancement Factors

The spectral differences of each source design had a direct effect on the radial dose profile of the source and subsequently on the dose enhancement characteristics of each source design. The MDEFs are shown in Figure 2.4.1 as a function of the radial distance from the center of the source along the transverse axis of the source. The calculated dose ratios beyond the gold-laden region are not strictly MDEF but simply the

ratio of the doses of the cases with and without GNPs; and show the reduction in dose beyond the gold-laden region. This dose reduction reached a maximum of 10% for the aluminum capsule design. The results show large dose enhancement within the GNP-laden region between 0 and 3.5 cm of up to 51.0 % at 1 cm for the aluminum capsule design. The titanium capsule design and the aluminum/titanium dual-capsule design had very similar dose enhancement profiles with a maximum of 49.3 % at 1 cm. The stainless steel capsule design showed the lowest dose enhancement with a maximum of 45.3 % at 1 cm.

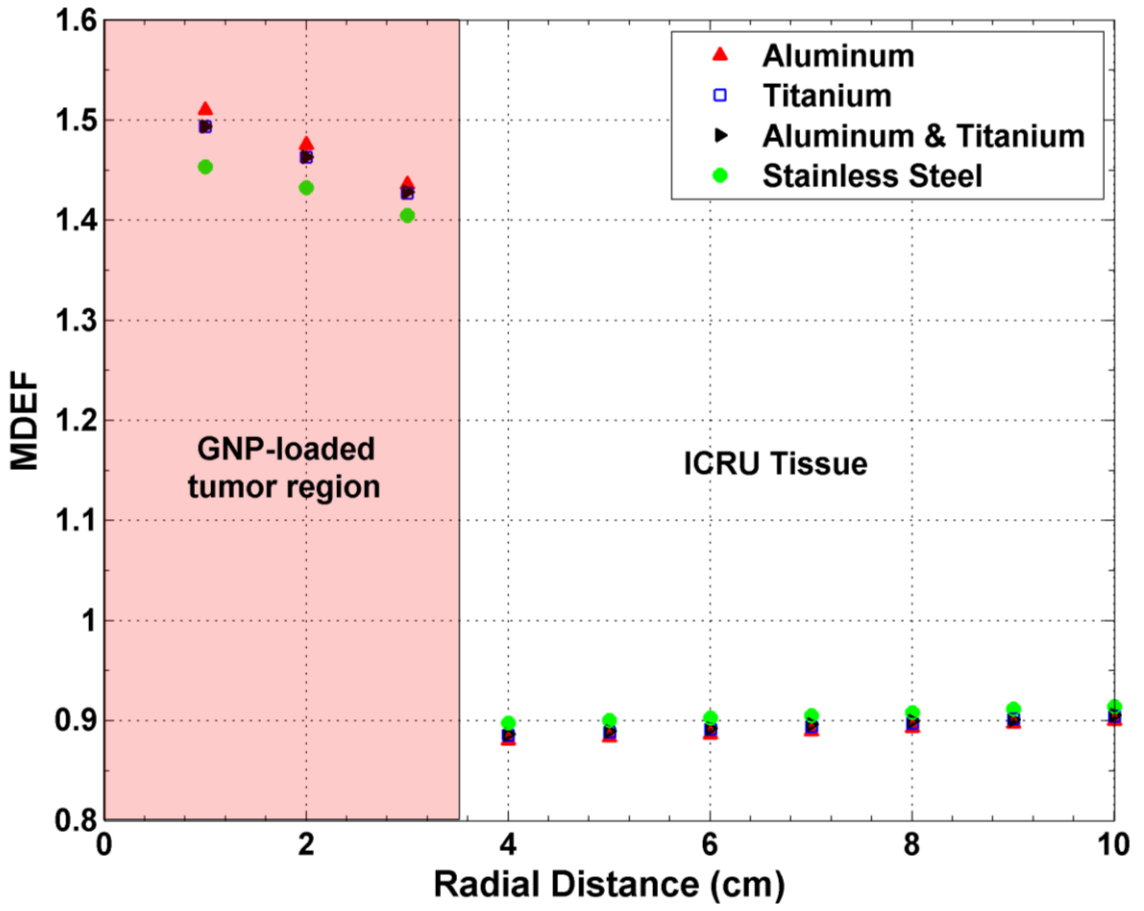

Figure 2.4.1 The calculated macroscopic dose enhancement factors for various encapsulation materials of the Yb-169 source as a function of radial distance along the transverse axis of the source.

As shown in previous studies [13], MDEFs are found to vary with radial distance as the photon spectrum changes accordingly. In the GNP-laden region, the MDEF falls off as the spectrum hardens within the tumor region. The high effective atomic number of the GNP-laden region results in more pronounced photoelectric absorption interactions with the low energy photon component of the spectrum. This means that the spectrum hardens substantially in the GNP-laden region and as a result the dose enhancement decreases by up to 14.5% from 51.0 % to 43.6 % for the aluminum source design. The dose enhancement fall-off is most pronounced for the designs that produce the softer photon spectra as spectral hardening would be more pronounced for these spectra; this is the case for the aluminum capsule design as compared to the stainless steel design. At depths beyond the GNP-laden region, the opposite effect can be observed but is far less pronounced, that is, dose enhancement shows a slight increase as the photon spectrum softens through the tissue. This happens because in the ICRU tissue Compton scattering is the dominant photon interaction mechanism and the scattered photons result in a softer photon spectrum, the opposite effect of what is observed in the GNP-laden tumor region.

2.5 Correlation between MDEF and Spectral Characteristics of Each Source

Table 2.5.1 summarizes all the spectral characteristics and the MDEF at 1 cm from the source for each source design. It can be observed from the results that as the photon spectrum hardens and the intensity-weighted average energy of the spectrum increases, the dose enhancement decreases. The importance of the low energy component of the photon spectrum is further demonstrated by looking at the number of photons below 110 and 50 keV and their relationship with the MDEF at 1 cm. The higher the

percentage of low energy photons present in the spectrum, the higher the dose enhancement. This is particularly expected between 10 and 110 keV as the total interaction cross sections of ICRU tissue loaded with 7 mg of gold per gram show a substantial increase in the interaction probability in this range. Figure 2.5.1 shows the correlation between MDEF and the percentage of photons between 10 and 110 keV present in the spectrum for each source encapsulation design.

Table 2.5.1 Spectral and dose enhancement characteristics of the different Yb-169 encapsulation designs. The results show direct correlation between MDEF and spectral characteristics of each source design.

Capsule Material	*E_{avg} (keV)*	*MDEF at 1 cm*	*No. of photons 10-110 keV (%)*	*No. of photons below 50 keV (%)*	*No. of photons below 100keV (%)*
Aluminum	*108.9*	*1.510*	*64.0%*	*2.1%*	*59.1%*
Aluminum & Titanium	*112.3*	*1.493*	*61.6%*	*2.7%*	*56.3%*
Titanium	*113.0*	*1.493*	*61.3%*	*2.0%*	*56.1%*
Stainless Steel	*122.9*	*1.453*	*54.8%*	*1.8%*	*48.9%*

The percentage of photons within 10-110 keV for each capsule design were 64.0, 61.6, 61.3 and 54.8 % for aluminum, aluminum/titanium, titanium and stainless steel respectively. The MDEF at 1 cm for each design were 1.510, 1.493, 1.493 and 1.453 respectively. The plot shown in Figure 2.5.1 illustrates how the two quantities vary with each source design and demonstrate a strong correlation between the two quantities.

The MC results illustrate how the choice of source design for a brachytherapy implementation of GNRT needs to be scrutinized. The main incentive behind GNRT is to take full advantage of the augmented photoelectric absorption of a GNP-laden tumor region. This effect is strongly dependent on low energy photons close to the L-edge (~12-14 keV) and the K-edge (~81 keV) of gold, and as a result the low energy component

within this region (~10-110 keV) needs to be maximized to obtain the highest dose enhancement during GNRT. Yb-169 has already been shown to be an excellent candidate as a brachytherapy source for GNRT [13] and the current study establishes how the source encapsulation strongly affects the dose enhancement characteristics.

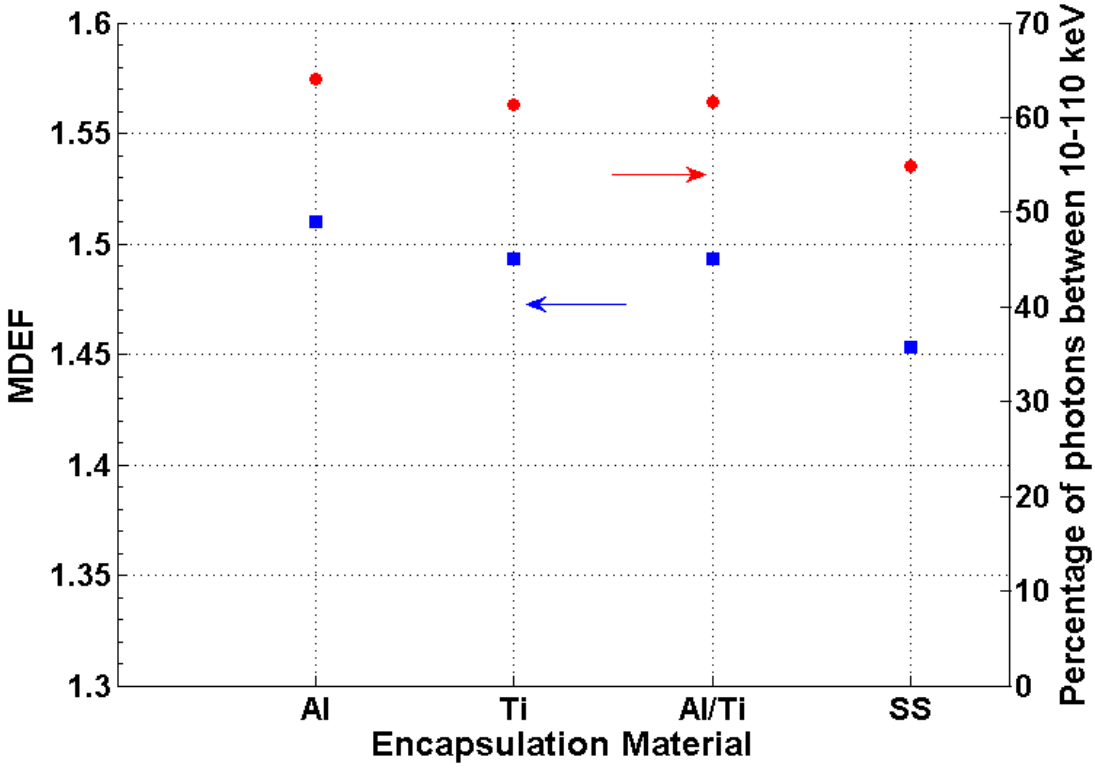

Figure 2.5.1 MDEF 1 cm away from the source as a function of source design. The percentage of photons between 10 keV and 110 keV are shown in the same graph to demonstrate a strong correlation between the two.

2.6 Secondary Electron Spectra and Microscopic Dose Enhancement

The resulting secondary electron spectra for all capsule designs were calculated and compared against each other. The condensed history Monte Carlo (MC) code EGSnrc [48] and user code DOSXYZnrc [49] were used to calculate the secondary electron spectrum for each one of the source encapsulation designs. The EGSnrc code was used for this task because the source code was immediately available for modification using a previously developed technique [13, 14, 27]. The code was modified to output the energy and origin of each electron liberated as a result of a photoelectric, Compton, or atomic relaxation events (Auger and Coster-Kronig with no differentiation between the two). This technique allows for the calculation of the secondary electron spectrum originating from gold atoms and tissue molecules separately in a GNP-laden tumor region. The resulting electron spectrum yields the average energy of all electrons released within the tumor taking into accounts changes in the photon spectrum through each encapsulation design and throughout the phantom. The electron spectra were collected using logarithmically spaced bins covering a minimum energy of 0.025 keV up to the maximum energy of 310 keV with a minimum bin width of 25 eV.

The MC simulation geometry closely matched that used in the MDEF simulations and consists of a source located at the center of a 30 cm-radius spherical phantom with the tumor region taken as a 3.5 cm-radius sphere centered at the origin of the larger sphere excluding the source region. The source region was defined as a $0.01 \times 0.01 \times 0.01\ cm^3$ region centered in the tumor representing the brachytherapy source. The source geometry was not modeled in detail and deemed not necessary as it was thoroughly modeled using MCNP. The MCNP generated photon spectrum just outside each capsule

design was used as the input spectrum for this simulation. The material composition of the tumor and phantom was taken as four-component ICRU tissue (i.e. 10.1 % hydrogen, 11.1 % carbon, 2.6 % nitrogen and 76.2 % oxygen). The spectrum of electrons released from gold atoms and tissue elements was computed separately using two independent simulations. The GNP-laden tumor was loaded with 7 mg of gold per g of tissue (0.7 % by weight) and the density was appropriately increased to 1.007 g/cm^3. The cross-section data used for all simulations were generated using the PEGS4 [50] code included in the EGSnrc software package. The electron and photon cutoff energies were chosen as 512 keV and 1 keV respectively for all simulations and 4×10^9 histories were computed for each simulation.

The resulting electron spectra for the titanium and stainless steel encapsulation are shown in Figures 2.6.1 and 2.6.2, respectively. The photoelectron spectra for the aluminum and aluminum/titanium dual encapsulation design are shown in Appendix A. These figures show the total number of electrons originating from photoelectric absorption interactions with and without the presence of gold (The contribution from atomic relaxations is not shown). The results show the remarkable increase in photoelectron yield across the entire range of energy due to the presence of GNPs in the tumor as previously reported in the literature [13, 14, 27]. It should be noted that the electron spectrum was also calculated for those electrons produced from Compton scattering events but are not shown in the figures shown below.

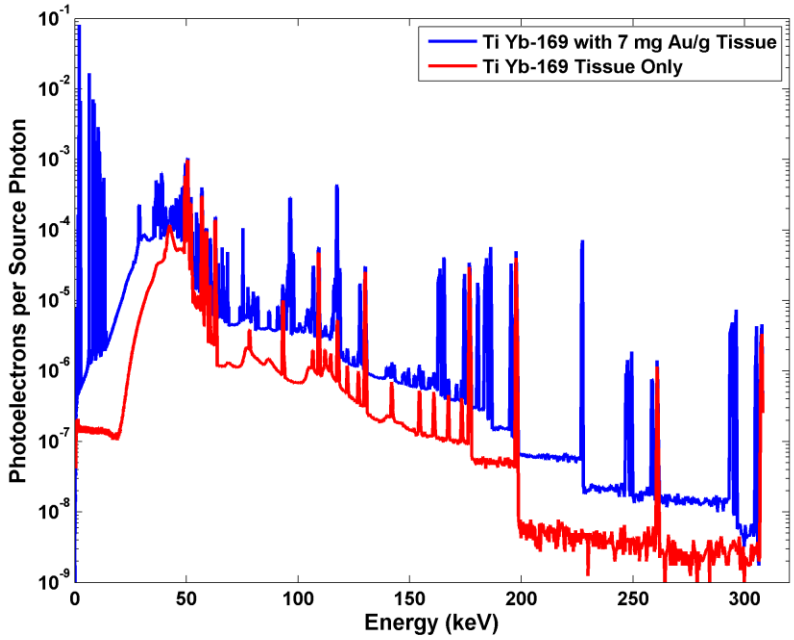

Figure 2.6.1 Spectrum of photoelectrons released in the tumor region for the Ti-6Al-4V titanium encapsulation design. The figure shows the spectrum from gold and tissue for the tumor loaded with 7 mg Au/g tissue and from tissue only.

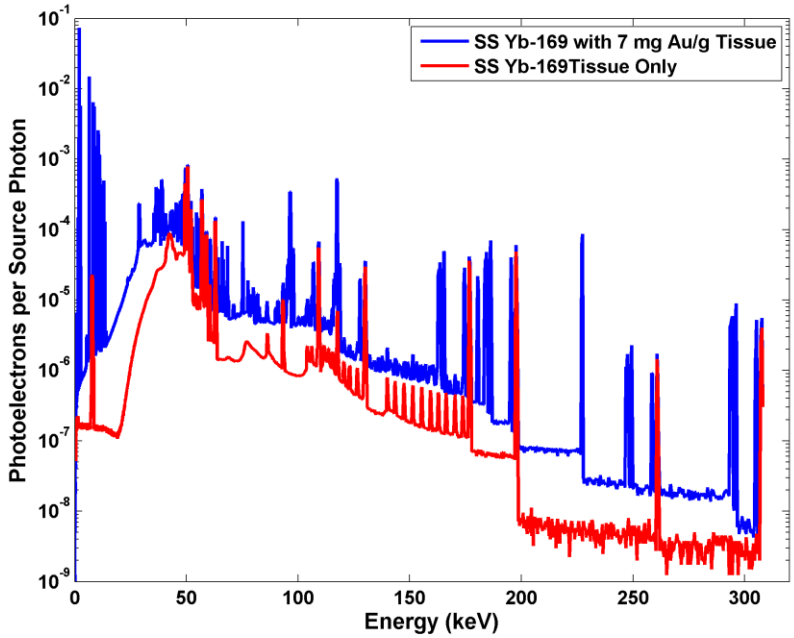

Figure 2.6.2 Spectrum of photoelectrons released in the tumor region for the 304 stainless steel encapsulation design. The figure shows the spectrum from gold and tissue for the tumor loaded with 7 mg Au/g tissue and from tissue only.

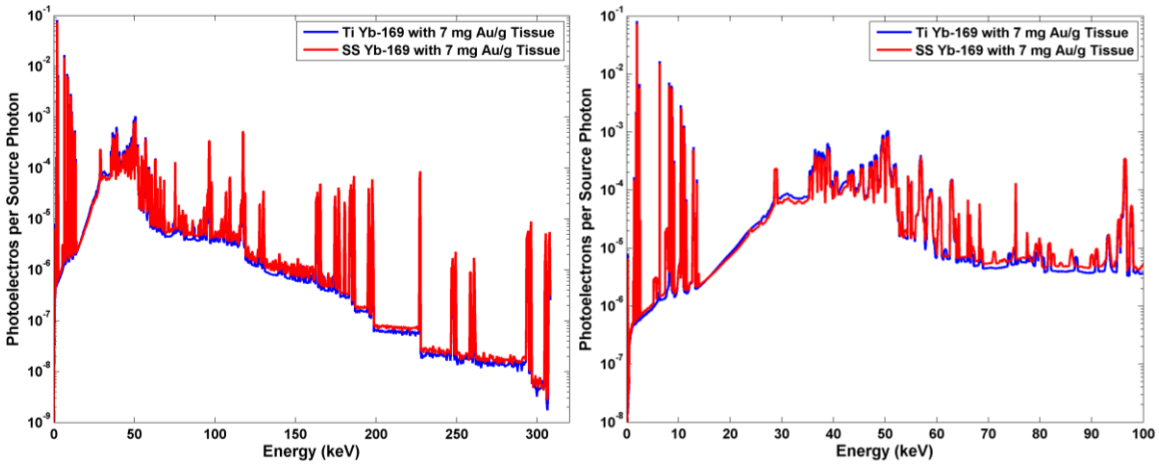

Figure 2.6.3 LEFT: Spectrum of photoelectrons released in the tumor region from gold and tissue for a tumor loaded with 7 mg Au/g of tissue for the 304 stainless steel and the Ti-6Al-4V titanium encapsulation design. RIGHT: Low energy region below 100 keV.

A similar pattern of photoelectron production is observed for all encapsulation designs, but some key differences can be observed in comparing the spectra for the stainless steel design and the titanium design as shown in Figure 2.6.3. In the lower energy region of < 50 keV, the titanium capsule design shows increased photoelectron yield which leads to superior dose enhancement from gold, consistent with the MCNP results. The spectra also show some distinct peaks consistent with the gamma-ray spectrum of Yb-169 and those related to the photoelectric absorption edges of gold. For the stainless steel encapsulation design, a strong peak around ~7.0 keV is present and consistent with fluorescence x-rays originating from the iron and nickel atoms present in the 304 stainless steel alloy. A quantitative look at the results is summarized in Table 2.6.1 highlighting some of the key differences between the encapsulation designs. All values listed in the table are normalized per source photon. The aluminum encapsulation design shows the highest photoelectron and Auger/Coster-Kronig electron yield and consequently the highest total energy deposition in both tissue and gold. This is expected

as aluminum represents an idealized situation for source encapsulation with minimal attenuation and spectral hardening. The aluminum/titanium dual encapsulation design and the single capsule titanium design show very similar photoelectron and Auger/Coster-Kronig electron yield for tissue and gold. The stainless steel design showed the lowest photoelectron yield and consequently the lowest energy deposition. On average, the titanium encapsulated source deposits 4.98 keV of energy per source photon in the tumor region; this compares to 4.52 keV of energy for the stainless steel encapsulation design.

Table 2.6.1 Total yield of photoelectrons (PE) and Auger/Coster-Kronig electrons (AE) and intensity-weighted total energy from gold and tissue for a tumor loaded with 7 mg Au/g of tissue for each encapsulation design. Auger/Coster-Kronig electrons are only produced in gold. All values listed in the table are normalized per source photon.

	Gold		***Tissue***			***Gold***	
Capsule Material	***Total PE Yield***	***Total PE Energy (keV)***	***Total PE Yield***	***Total PE Energy (keV)***	***Total PE Energy (keV)***	***Total AE Yield***	***Total AE Energy (keV)***
Aluminum	*0.0702*	*2.92*	*0.0485*	*1.73*	*4.65*	*0.130*	*0.487*
Aluminum/Titanium	*0.0684*	*2.87*	*0.0468*	*1.67*	*4.54*	*0.126*	*0.477*
Titanium	*0.0677*	*2.86*	*0.0462*	*1.65*	*4.51*	*0.125*	*0.472*
Stainless Steel	*0.0606*	*2.67*	*0.0404*	*1.42*	*4.09*	*0.112*	*0.429*

The differences in the secondary electron spectrum for each source design have direct consequences in the local energy deposition around the gold. In order to study this behavior at a smaller scale, the microscopic dose enhancement factor (mDEF) was calculated for the titanium and the stainless steel encapsulation designs. These two designs were chosen because they are the best candidates for an HDR brachytherapy source. The aluminum encapsulation design lacks the biocompatibility and structural integrity to encapsulate the source and the added thickness of the dual capsule design

weakens the strength of the source with no major gain in dose enhancement as shown in Table 2.6.1 and Figure 2.4.1.

The methodology used to calculate all mDEF values was previously developed by Jones, et al. [14] and relies on computing the electron point dose kernel due to the secondary electron spectrum using the event-by-event MC code NOREC [51]. This MC code calculates electron tracks in water. The method involves the calculation of the electron point dose kernel from the secondary electron spectra for gold atoms and tissue elements separately. The point dose kernels are obtained by modeling each source of secondary electrons as a point source of electrons and computing the dose deposited at different radial distances. These point dose kernels are used to compute the dose enhancement that results from replacing a single point of tissue with gold; this is quantified by the ratio of point dose kernels of gold to tissue and defined as the microscopic dose enhancement factor [14, 27].

The mDEF for the titanium and stainless steel source encapsulation designs are shown in Figure 2.6.4. The values are shown for radial distances between 1 and 100 μm with both designs showing a similar pattern of dose enhancement with a peak mDEF value at 15 μm. However, the titanium source encapsulation design shows consistent improvement of local dose enhancement with improved mDEF across the region between 1 and 20 μm. The biggest improvement is observed around the peak at 15 μm with the titanium design showing an mDEF value of 138 and the stainless steel design showing 119. These values represent a 16 % improvement in mDEF at 15 μm by replacing the stainless steel encapsulation with titanium. The cumulative effect from 1 to 20 μm shows a consistent improvement over that whole range.

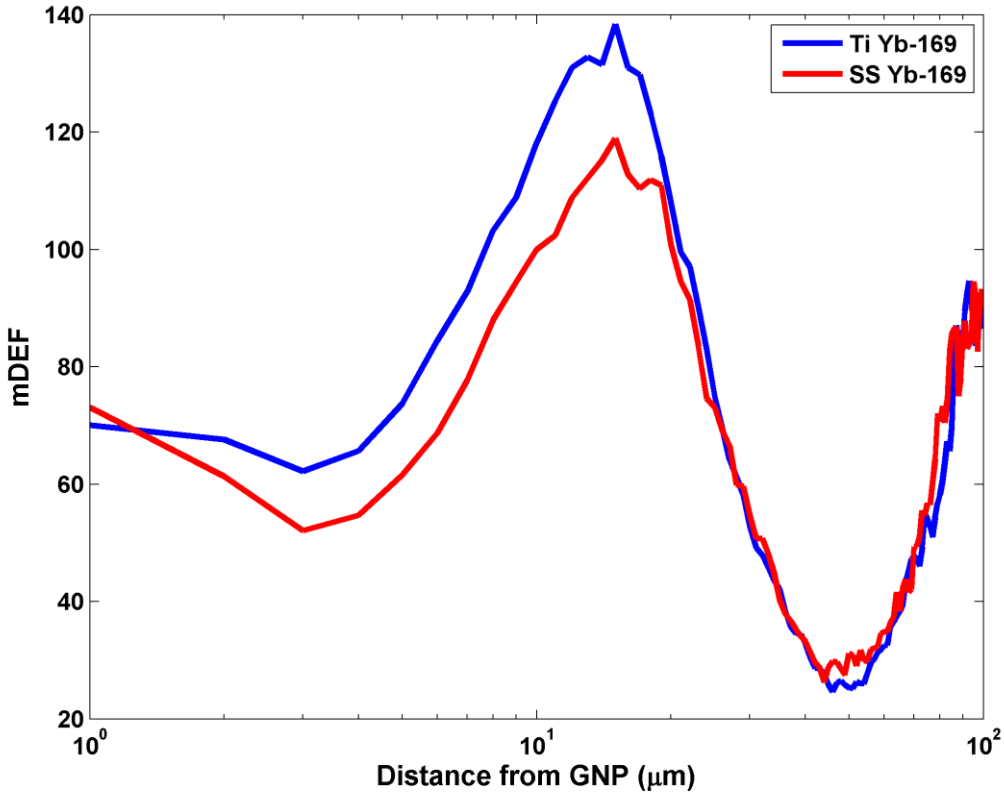

Figure 2.6.4 Microscopic dose enhancement factor (mDEF) for the Ti-6Al-4V titanium and 304 stainless steel source encapsulation designs for Yb-169.

2.7 Discussion

The spectral variations from each design considered in the study arise due to the attenuation and scattering of source photons traversing the source core and the encapsulation material. Consequently, a low-Z biocompatible material with the structural integrity to safely encapsulate the radioactive core of the source is preferred as the encapsulation material of any brachytherapy source considered for GNRT. Overall, the following aspects of each source design need to be taken into consideration for an optimum Yb-169 source design for GNRT. The aluminum, titanium and aluminum/titanium capsule designs resulted in somewhat comparable dose enhancement

characteristics but showed different transmission characteristics that would affect the strength of each source. Despite its superiority to other encapsulation materials in terms of producing an enhancement in dose, aluminum itself is not biocompatible and therefore not suitable as an encapsulation material for a brachytherapy source. Furthermore, an aluminum capsule lacks mechanical strength and would be susceptible to breakage, posing a major safety risk in clinical practice. Stainless steel, on the other hand, is a safe and biocompatible material but its use as a source encapsulation material produced the smallest amount of dose enhancement in this study. As a result, it is less desirable to adopt the stainless steel source design for GNRT. The dual encapsulation design with aluminum and titanium provides an adequate strength for the source as well as desirable dosimetric characteristics for GNRT and has been demonstrated as a feasible design for manufacturing [43]. However, the added filter thickness significantly decreases the photon transmission through the capsule, which hinders the production of an HDR source. Furthermore, if not manufactured carefully, the added complexity of having two layers of encapsulation would also increase the likelihood of geometrical distortions, potentially affecting the dosimetric characteristics of the source.

The titanium capsule design appears to meet the source design goals more favorably because it allows for a significant improvement in the dose enhancement characteristics when compared to the stainless steel capsule design, while avoiding some of the shortcoming of the aluminum and dual encapsulation source designs. Titanium provides excellent biocompatibility, high corrosion resistance, and exceptional strength for safe encapsulation of the activated Yb core. Moreover, the low density of titanium (~4.4 g/cm^3), about 45% lower than that of stainless steel (~8.0 g/cm^3), allows good

photon transmission through the source capsule, while preserving much of the low energy photon component in the Yb-169 spectrum. The added strength of titanium over stainless steel [52] also provides the opportunity to decrease the thickness of the capsule and potentially further improving the dose enhancement properties of the source.

The current MC results reflect the importance of careful consideration of the source design for a brachytherapy implementation of GNRT. As shown in this study, the source encapsulation can substantially alter the photon spectrum from the source and in turn affect the amount of dose enhancement achievable under the given irradiation scenario. The change in the source photon spectrum affects the dose enhancement not only macroscopically but also microscopically on a cellular scale. The results of this study consistently show the titanium encapsulation design would produce improved dose enhancement and radiosensitization during GNRT.

The current MC results showed that there were statistically significant variations among the investigated source capsule designs, in terms of photon spectrum, transmitted photon fluence, macroscopic dose enhancement, and microscopic dose enhancement. Specifically, under the identical source and phantom geometry, there was an increase in the average photon energy, a decrease in the photon transmission, and a decrease in the macroscopic and microscopic dose enhancement, respectively, as the encapsulation material changed from aluminum through titanium to stainless steel. Additionally, the aluminum/titanium dual capsule design exhibited dosimetric characteristics comparable to those associated with the titanium capsule design, except for a slight decrease in the photon transmission. In comparison with a more conventional stainless steel capsule design, all three other capsule designs considered in this study resulted in a significant

improvement (~10%) for the macroscopic and microscopic dose enhancement achievable under the given GNRT scenario. The increased structural integrity of titanium over stainless steel may also provide the opportunity to shrink the size of the capsule design, further improving the dose enhancement characteristics of the source.

CHAPTER 3

TG-43 CHARACTERIZATION OF YTTERBIUM-169 SOURCES

3.1 TG-43 Formalism for Brachytherapy Dose Calculation

The dose formalism for brachytherapy sources specified by the AAPM TG-43 was first presented in 1995. Earlier dose calculation formalisms were only dependent on apparent activity (A_{app}), exposure-rate constants, tissue-attenuation coefficients, and equivalent mass of radium. However, it did not account for differences in source geometry and it mainly depended on the type of radionuclide. TG-43 introduced a new set of dosimetric parameters that not only depended on the specific geometry of the brachytherapy source but could also be directly measured or calculated for each source. The new formalism introduced by TG-43 resulted in standardization of dose-calculation methods and dose distributions of brachytherapy sources [53].

The general formalism is based on the 2D dose-rate equation:

$$\dot{D}(r,\theta) = S_K \cdot \Lambda \cdot \frac{G_L(r,\theta)}{G_L(r_o,\theta_o)} \cdot g_L(r) \cdot F(r,\theta) \tag{3.1.1}$$

where r represents the distance (cm) from the point of interest to the center of the active source region, r_o is the reference distance defined as 1 cm, θ is the polar angle that defines the point of interest relative to the longitudinal axis of the source, and θ_o defines the reference angle at the traverse plane of the source, and specified to be 90^o. As shown in Figure 3.1.1 the point $P(r_o,\theta_o)$ defines the reference point that lies on the traverse bisector of the source. The quantities of interest that are needed to completely characterize the dose distribution of a brachytherapy sources are:

S_K the air-kerma strength of the source (μGy·m^2/h)

Λ the dose-rate constant in water (1/m^2)

$G(r,\theta)$ the geometry function (1/m^2)

$g_L(r)$ the radial dose function

$F(r,\theta)$ the anisotropy function

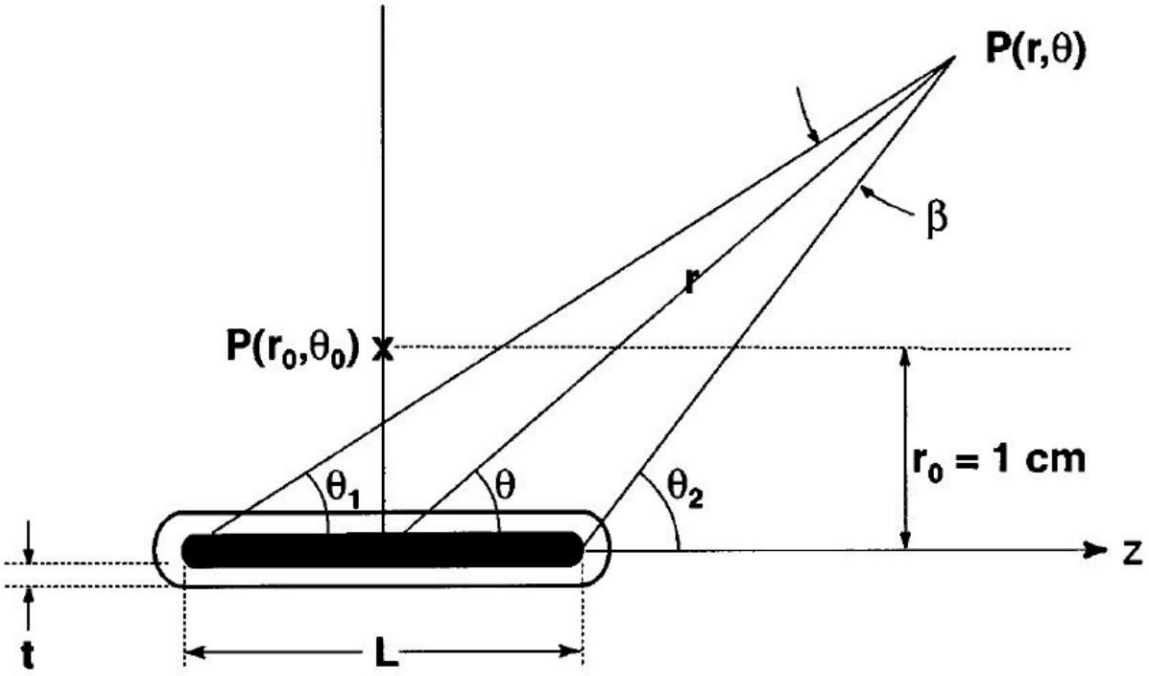

Figure 3.1.1 Geometry and coordinate system used to define the TG-43 dose calculation formalism for brachytherapy sources from Ref. 53.

3.1.1 Air-Kerma Strength

S_K is the air-kerma strength of the source and it is a quantity used to describe the strength of the source based on the air-kerma rate, at a distance large enough such that the source can be considered a point source. The air-kerma rate $\dot{K}$ is the sum of kinetic energy transferred to electrons and positrons per unit mass in air and time. The relationship between air-kerma rate and the air-kerma strength is:

$$S_k = \dot{K}_\delta(d) \cdot d^2 \tag{3.1.2}$$

where $\dot{K}_\delta(d)$ is the air-kerma rate *in vacuo* due to photons of energy greater than δ, at a distance d. The distance d is the distance from the center of the active source region to a point along the traverse plane of the source. This distance should be much larger than the greatest linear dimension of the source such that the source is considered a point source and typically chosen to be 100 cm. The cutoff energy δ excludes any low-energy contaminant photons that may contribute to $\dot{K}_\delta(d)$ without contributing to the dose at any distance beyond 1 mm in tissue. This contribution may arise from any characteristic x-ray peaks arising from the encapsulation material (e.g. titanium or stainless steel) [53].

3.1.2 Dose-Rate Constant

The dose rate constant Λ is defined as the dose rate to water at a distance of 1 cm on the transverse axis reference point (r_o, θ_o) per unit air-kerma strength:

$$\Lambda = \frac{\dot{D}(r_o, \theta_o)}{S_k} \tag{3.1.3}$$

The dose-rate constant accounts for the effects of source geometry, spatial distribution of radioactivity within the source itself, filtration by the source encapsulation, and scattering

in water surrounding the source. This definition now depends on both the radionuclide and the specific source geometry.

3.1.3 Geometry Function

The geometry function accounts for any geometric fall-off of the fluence with distance r and the spatial distribution of radioactivity within the source. The purpose of the function is to increase the accuracy in situations in which dose rates are approximated by interpolation of tabulated data. The geometry function does not take into account attenuation or scattering in the medium and it is an effective inverse square law correction. In the case of a line-source geometry like the ones proposed in the current work the geometry function is:

$$\begin{aligned} \mathrm{G_L}(\mathrm{r},\theta) &= \frac{\beta}{Lr\sin\theta} \quad \text{for } \theta \neq 0^o \\ \mathrm{G_L}(\mathrm{r},\theta) &= \frac{1}{r^2-\frac{L^2}{4}} \quad \text{for } \theta = 0^o \end{aligned} \tag{3.1.4}$$

where β is the angle measured in radians subtended by the tips of the source with respect to the point of interest $P(r,\theta)$ as shown in Figure 3.1.1 and L is the length of the active source region.

3.1.4 Radial Dose Function

The radial dose function accounts for dose fall-off along the transverse axis due to absorption and scatter in tissue. This function complements the definition of the geometry function that does not include scattering and attenuation in tissue.

$$\mathrm{g_L}(\mathrm{r}) = \frac{\dot{D}(r,\theta_o)}{\dot{D}(r_o,\theta_o)}\frac{G_L(r_o,\theta_o)}{G_L(r,\theta_o)} \tag{3.1.5}$$

3.1.5 Anisotropy Function

The anisotropy function accounts for the anisotropy of the dose distribution around the source as a function of the polar angle and defined as:

$$\mathrm{F(r,\theta)} = \frac{\dot{D}(r,\theta)}{\dot{D}(r,\theta_o)} \frac{G_L(r,\theta_o)}{G_L(r,\theta)} \tag{3.1.6}$$

The anisotropy function is defined as unity on the transverse plane and decreases as r increases, as θ approaches 0° or 180° and as the photon energy decreases.

3.2 Monte Carlo Calculation

Table 3.2.1 Yb-169 photon spectrum including all photons with yields greater than 0.1 % and ignoring all dosimetrically irrelevant gamma rays below 5 keV.

Energy (keV)	***Photons per disintegration***
49.77	*0.532*
50.74	*0.94*
57.30	*0.0993*
57.51	*0.192*
57.90	*0.00379*
59.03	*0.0647*
59.21	*0.0172*
63.12	*0.442*
93.62	*0.0261*
109.78	*0.1747*
118.19	*0.01869*
130.52	*0.1131*
177.21	*0.2216*
197.96	*0.358*
261.08	*0.01715*
307.74	*0.1005*
TOTAL	*3.32083*

The radiation transport code MCNP5 was used to compute all the necessary quantities to characterize the Yb-169 source as defined by TG-43. The source and encapsulation geometry were modeled exactly as shown in Figure 2.1.1. The active region of the source was modeled with a uniform activity distribution. The Yb-169 photon spectrum used is shown in Table 3.2.1 excluding all photons with intensity lower than 0.1 % and energy lower than 5 keV as specified in TG-43 [47]. Two different MCNP models were developed to compute all TG-43 parameters.

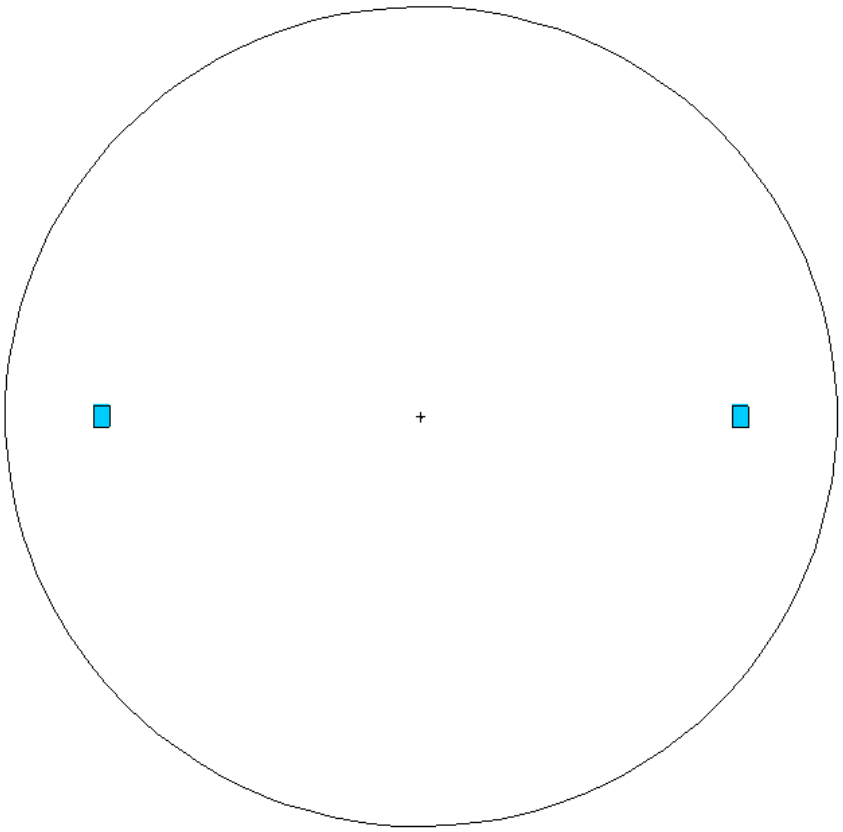

Figure 3.2.1 MCNP tally geometry for computing the air kerma strength at $\theta_o = 90^o$ and $d = 100\ cm$. The source is centered on a spherical region *in vacuo* with a radius of *130 cm.*

The air-kerma strength S_k was calculated with the Yb-169 source centered on a 130 cm radius spherical phantom *in vacuo*. The air-kerma rate was determined at the reference point $\theta_o = 90^o$ at a distance *d = 100 cm* using the MCNP5 energy deposition F6 tally with units of $MeVg^{-1}photon^{-1}$. This region was defined by first delineating the region at *d = 100 cm* from the center of the source by defining two concentric spheres with radii of 97.5 cm and 102.5 cm. The angular constraint of $\theta_o = 90^o$ was defined by using two cones with vertex angles of $\theta = 88^o$one aligned with the +z-axis and the other aligned with the –z-axis. This defines a *5 cm* ring tally centered at *d = 100 cm* with $\theta_o = 90^o \pm 2^o$ as shown in Figure 3.2.1. The MCNP output is the air-kerma per source photon (K_{MC}) in units of $MeV \cdot g^{-1} \cdot photon^{-1}$. The air-kerma rate is calculated from K_{MC} and converted to units of $cGy \cdot mCi^{-1} \cdot h^{-1}$ by:

$$\dot{K}(d,\theta) = K_{MC} \cdot I_\gamma \cdot 2.134 \times 10^3 \frac{cGy}{mCi \cdot h} \tag{3.2.1}$$

where I_γ is the total number of photons per disintegration of the source. The air-kerma rate may also be written in terms of the unit U ($cGy \cdot cm^2 \cdot h^{-1}$) as specified in TG-43 [53].

The dose distribution surrounding the source was computed by simulating the source centered in a spherical water phantom with a radius of 50 cm, an appropriate size to approximate full-scatter conditions of a semi-infinite water phantom. An array of tally regions was modeled to collect the dose at radial distances of 0.5 cm and 1-10 cm in 1 cm steps and at angles between $\theta = 0^o$ and $\theta = 180^o$ in 10^o steps. This was accomplished by generating spherical shells with mean radii at the desired radial distance (i.e. 0.5 cm and 1-10 cm in 1 cm steps). The thickness of each shell was calculated to be as thin as

possible to appropriately approximate the detection region while maximizing collection efficiency during the MC simulation. The criteria were developed by Luxton et al. [54] and compares the factor $R_V = (R_1^3 + R_2^3/2)^{\frac{1}{3}}$ that subdivides each shell bounded by the inner radius R_1 and outer radius R_2 into smaller shells of equal volume, with the mean radius of the shell $R_M = (R_1 + R_2)/2$. The calculated dose for a shell approximates the dose at that mean radius of the shell only if the two factors differ by less than 1 %, i.e. $|(R_V/R_M)^2 - 1| < 0.01$.

The angular dependence of each tally region was defined by using concentric cones about the +z-axis and –z-axis to restrict collection along the desired angle from $\theta = 0^o$ to $\theta = 180^o$ in 10^o steps. For the $\theta = 0^0$ region, a cone along the –z-axis with vertex angle of 2^o defined the $\theta = 0^o$ region; a similar cone along the +z-axis defined the $\theta = 180^o$. The regions between 10^o and 170^o are defined by concentric cones centered at the desired angle with an angular opening $\pm 4^o$, e.g. for the $\theta = 10^o$ two concentric cones centered along the –z-axis with vertex angles of 8^o and 12^o defined the desired tally region. The same method was used to define all of the angles and using concentric cones with the appropriate vertex angles to define each region in 10^o (i.e. $8^o, 12^o, 18^o, 22^o, 28^o, 32^o, \ldots$). The result is a series of ring tallies that collect the dose distribution surrounding the source as shown in Figure 3.2.2.

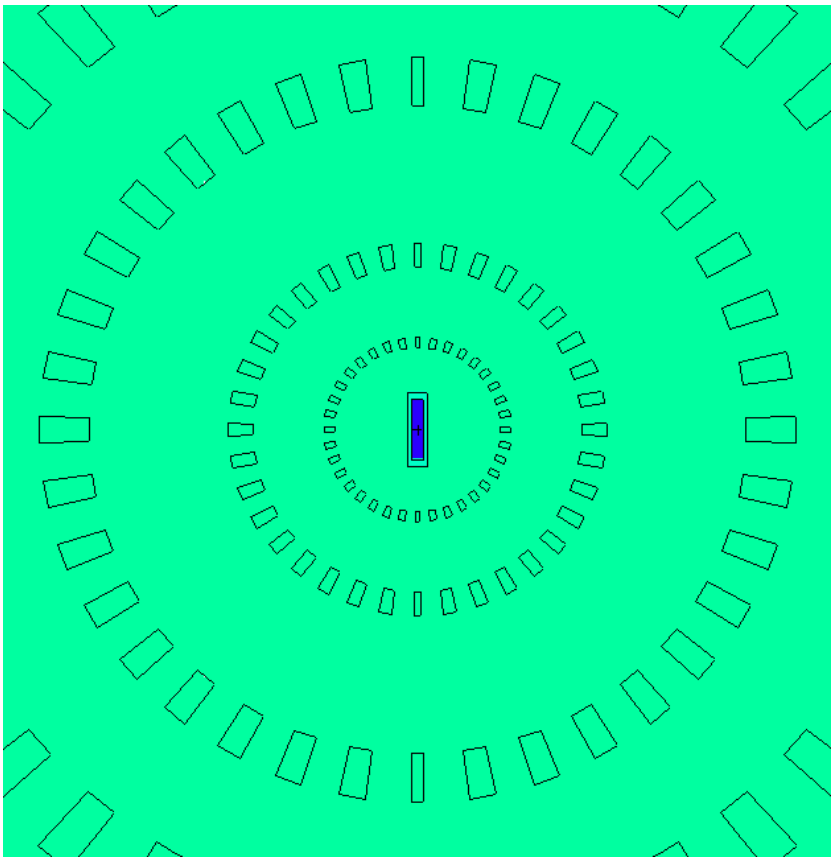

Figure 3.2.2 MCNP tally geometry for computing the dose distribution around the Yb-169 source.

3.3 Results and Discussion

The dosimetric characterization outlined in TG-43 was completed for the Ti-6Al-4V titanium source encapsulation design and the 304 stainless steel source encapsulation design as these two sources are the best candidates for an HDR brachytherapy source. The air-kerma strength calculated by MC resulted in $S_K = 1.12 \pm 0.03\ U \cdot mCi^{-1}$for the Ti-6Al-4V titanium design and $S_K = 1.02 \pm 0.03\ U \cdot mCi^{-1}$for the 304 stainless steel design. The dose rates at the reference point $\dot{D}(r_o, \theta_o)$ were calculated as $\dot{D}(r_o, \theta_o) = 1.33 \pm 0.02\ cGy \cdot mCi^{-1} \cdot h^{-1}$ for the Ti-6Al-4V titanium design and $\dot{D}(r_o, \theta_o) =$

$1.22 \pm 0.02\ cGy \cdot mCi^{-1} \cdot h^{-1}$ for the 304 stainless steel design. The dose-rate constants were calculated as $\Lambda = 1.19 \pm 0.03\ cGy \cdot h^{-1} \cdot U^{-1}$ for both source designs. This value compares well to other reported values for Yb-169 source models: $\Lambda = 1.210 \pm 0.050$ [31], $\Lambda = 1.204 \pm 0.004$ [55], $\Lambda = 1.19 \pm 0.03$ [37] $\Lambda = 1.170 \pm 0.010$, and $\Lambda = 1.191 \pm 0.007\ cGy \cdot h^{-1} \cdot U^{-1}$ [56].

Table 3.3.1 Calculated geometry function $G_L(r, \theta)$ for both Ti-6Al-4V titanium and 304 stainless steel source encapsulation designs.

Polar angle θ(deg.)	***r (cm)***										
	0.5	***1***	***2***	***3***	***4***	***5***	***6***	***7***	***8***	***9***	***10***
0	*4.558*	*1.032*	*0.252*	*0.111*	*0.063*	*0.040*	*0.028*	*0.020*	*0.016*	*0.012*	*0.010*
10	*4.530*	*1.030*	*0.252*	*0.111*	*0.063*	*0.040*	*0.028*	*0.020*	*0.016*	*0.012*	*0.010*
20	*4.450*	*1.026*	*0.252*	*0.111*	*0.063*	*0.040*	*0.028*	*0.020*	*0.016*	*0.012*	*0.010*
30	*4.337*	*1.021*	*0.251*	*0.111*	*0.063*	*0.040*	*0.028*	*0.020*	*0.016*	*0.012*	*0.010*
40	*4.212*	*1.014*	*0.251*	*0.111*	*0.063*	*0.040*	*0.028*	*0.020*	*0.016*	*0.012*	*0.010*
50	*4.092*	*1.006*	*0.250*	*0.111*	*0.063*	*0.040*	*0.028*	*0.020*	*0.016*	*0.012*	*0.010*
60	*3.989*	*1.000*	*0.250*	*0.111*	*0.062*	*0.040*	*0.028*	*0.020*	*0.016*	*0.012*	*0.010*
70	*3.912*	*0.995*	*0.250*	*0.111*	*0.062*	*0.040*	*0.028*	*0.020*	*0.016*	*0.012*	*0.010*
80	*3.864*	*0.991*	*0.249*	*0.111*	*0.062*	*0.040*	*0.028*	*0.020*	*0.016*	*0.012*	*0.010*
90	*3.848*	*0.990*	*0.249*	*0.111*	*0.062*	*0.040*	*0.028*	*0.020*	*0.016*	*0.012*	*0.010*

The geometry function $G_L(r, \theta)$ (Table 3.3.1) was equivalent for both designs because they shared the exact dimensions within the active source region. The function represents the effective inverse-square correction based on the line-source approximation outlined in equation 3.1.4. The function shows both sources effectively become point sources for r $\geq$ 5 cm. The radial dose functions are shown on Table 3.3.2 and the fit to 5th order polynomial as specified in [53] is shown in Figure 3.3.1 and are equivalent for both sources. The 2D anisotropy function for the Ti-6Al-4V titanium and the 304 stainless steel source encapsulation design are shown on Tables 3.3.3 and 3.3.4 respectively.

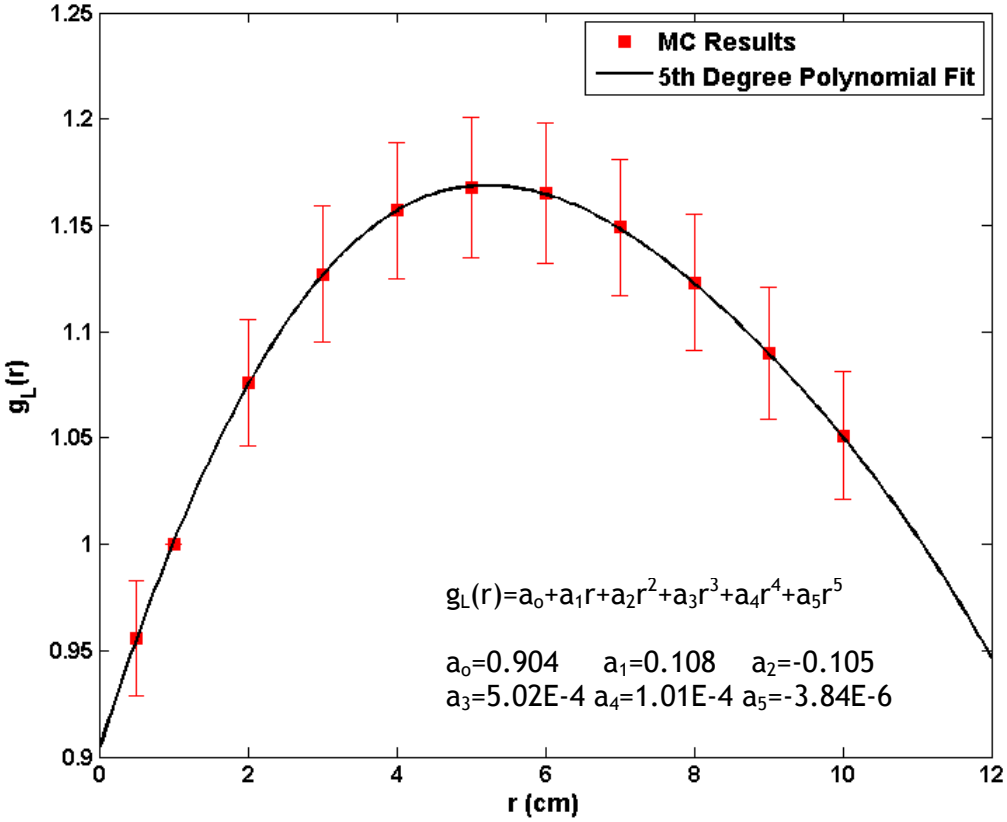

Figure 3.3.1 Calculated radial dose function for the Ti-6Al-4V titanium source design and 5th degree polynomial fit along with corresponding fitting parameters.

Table 3.3.2 Radial dose function $g_L(r,\theta)$ values for the Ti-6Al-4V titanium and 304 stainless steel source designs.

r (cm)	*$g_L(r)$ for Ti design*		*$g_L(r)$ for SS design*	
0.5	*0.952*	*± 0.027*	*0.956*	*± 0.027*
1	*1.000*	*± 0*	*1.000*	*± 0*
2	*1.076*	*± 0.030*	*1.076*	*± 0.030*
3	*1.127*	*± 0.032*	*1.127*	*± 0.032*
4	*1.157*	*± 0.033*	*1.157*	*± 0.032*
5	*1.168*	*± 0.033*	*1.168*	*± 0.033*
6	*1.165*	*± 0.033*	*1.165*	*± 0.033*
7	*1.149*	*± 0.032*	*1.149*	*± 0.032*
8	*1.123*	*± 0.032*	*1.123*	*± 0.032*
9	*1.090*	*± 0.031*	*1.090*	*± 0.031*
10	*1.051*	*± 0.030*	*1.051*	*± 0.030*

Table 3.3.3 2D Anisotropy function $F(r, \theta)$ values for the Ti-6Al-4V titanium design.

Polar angle θ (degrees)	*r (cm)*																			
	0.5		*1*		*2*		*3*		*4*		*5*		*6*		*7*		*8*		*9*		*10*	
0	0.568	± 0.018	0.566	± 0.018	0.618	± 0.020	0.662	± 0.021	0.700	± 0.022	0.729	± 0.023	0.750	± 0.024	0.770	± 0.024	0.786	± 0.025	0.799	± 0.025	0.809	± 0.026
10	0.630	± 0.020	0.642	± 0.020	0.690	± 0.022	0.727	± 0.023	0.756	± 0.024	0.777	± 0.024	0.795	± 0.025	0.810	± 0.025	0.822	± 0.026	0.832	± 0.026	0.842	± 0.026
20	0.737	± 0.023	0.746	± 0.023	0.779	± 0.024	0.804	± 0.025	0.823	± 0.026	0.837	± 0.026	0.849	± 0.027	0.859	± 0.027	0.867	± 0.027	0.874	± 0.027	0.880	± 0.028
30	0.823	± 0.026	0.828	± 0.026	0.848	± 0.027	0.864	± 0.027	0.876	± 0.027	0.886	± 0.028	0.893	± 0.028	0.900	± 0.028	0.905	± 0.028	0.909	± 0.029	0.913	± 0.029
40	0.887	± 0.028	0.888	± 0.028	0.901	± 0.028	0.911	± 0.029	0.918	± 0.029	0.924	± 0.029	0.929	± 0.029	0.932	± 0.029	0.935	± 0.029	0.938	± 0.029	0.941	± 0.029
50	0.933	± 0.029	0.933	± 0.029	0.940	± 0.029	0.946	± 0.030	0.950	± 0.030	0.953	± 0.030	0.956	± 0.030	0.958	± 0.030	0.960	± 0.030	0.961	± 0.030	0.963	± 0.030
60	0.963	± 0.030	0.964	± 0.030	0.968	± 0.030	0.971	± 0.030	0.973	± 0.031	0.975	± 0.031	0.976	± 0.031	0.977	± 0.031	0.978	± 0.031	0.979	± 0.031	0.980	± 0.031
70	0.983	± 0.031	0.985	± 0.031	0.987	± 0.031	0.988	± 0.031	0.989	± 0.031	0.990	± 0.031	0.990	± 0.031	0.990	± 0.031	0.991	± 0.031	0.991	± 0.031	0.991	± 0.030
80	0.996	± 0.031	0.995	± 0.031	0.997	± 0.031	0.997	± 0.031	0.998	± 0.031	0.998	± 0.031	0.998	± 0.031	0.998	± 0.031	0.998	± 0.031	0.998	± 0.031	0.998	± 0.030
90	1.000	± 0	1.000	± 0	1.000	± 0	1.000	± 0	1.000	± 0	1.000	± 0	1.000	± 0	1.000	± 0	1.000	± 0	1.000	± 0	1.000	± 0

Table 3.3.4 2D Anisotropy function $F(r, \theta)$ values for the 304 stainless steel design.

Polar angle θ (degrees)	*r (cm)*																			
	0.5		*1*		*2*		*3*		*4*		*5*		*6*		*7*		*8*		*9*		*10*	
0	0.570	± 0.018	0.566	± 0.018	0.611	± 0.020	0.653	± 0.021	0.689	± 0.022	0.718	± 0.023	0.738	± 0.024	0.758	± 0.024	0.774	± 0.025	0.788	± 0.025	0.799	± 0.026
10	0.615	± 0.020	0.621	± 0.020	0.666	± 0.022	0.705	± 0.023	0.734	± 0.024	0.757	± 0.024	0.776	± 0.025	0.791	± 0.025	0.805	± 0.026	0.816	± 0.026	0.827	± 0.026
20	0.704	± 0.023	0.715	± 0.023	0.750	± 0.024	0.777	± 0.025	0.799	± 0.026	0.815	± 0.026	0.829	± 0.027	0.840	± 0.027	0.849	± 0.027	0.858	± 0.027	0.865	± 0.028
30	0.793	± 0.026	0.799	± 0.026	0.822	± 0.027	0.841	± 0.027	0.855	± 0.027	0.866	± 0.028	0.876	± 0.028	0.883	± 0.028	0.890	± 0.028	0.896	± 0.029	0.901	± 0.029
40	0.866	± 0.028	0.866	± 0.028	0.881	± 0.028	0.892	± 0.029	0.902	± 0.029	0.909	± 0.029	0.915	± 0.029	0.920	± 0.029	0.923	± 0.029	0.927	± 0.029	0.931	± 0.029
50	0.920	± 0.029	0.918	± 0.029	0.927	± 0.029	0.933	± 0.030	0.939	± 0.030	0.943	± 0.030	0.946	± 0.030	0.949	± 0.030	0.951	± 0.030	0.954	± 0.030	0.956	± 0.030
60	0.957	± 0.030	0.956	± 0.030	0.960	± 0.030	0.964	± 0.030	0.967	± 0.031	0.968	± 0.031	0.970	± 0.031	0.972	± 0.031	0.973	± 0.031	0.974	± 0.031	0.976	± 0.031
70	0.981	± 0.031	0.981	± 0.031	0.983	± 0.031	0.985	± 0.031	0.986	± 0.031	0.987	± 0.031	0.987	± 0.031	0.988	± 0.031	0.988	± 0.031	0.989	± 0.031	0.990	± 0.030
80	0.995	± 0.031	0.995	± 0.031	0.996	± 0.031	0.996	± 0.031	0.997	± 0.031	0.997	± 0.031	0.997	± 0.031	0.997	± 0.031	0.997	± 0.031	0.997	± 0.031	0.998	± 0.030
90	1.000	± 0	1.000	± 0	1.000	± 0	1.000	± 0	1.000	± 0	1.000	± 0	1.000	± 0	1.000	± 0	1.000	± 0	1.000	± 0	1.000	± 0

The differences in filtration through the titanium encapsulation design are evident in the anisotropy function as shown in Figure 3.3.2. The values are reduced through polar angles that correspond to going through the most encapsulation material, at which the differences in composition are most pronounced. Dosimetric perturbations are more pronounced in the 2D anisotropy function for the stainless steel source design due to the increased density and attenuation through the stainless steel as opposed to the titanium. This translates to higher anisotropy in the dose distribution of the source around its end caps.

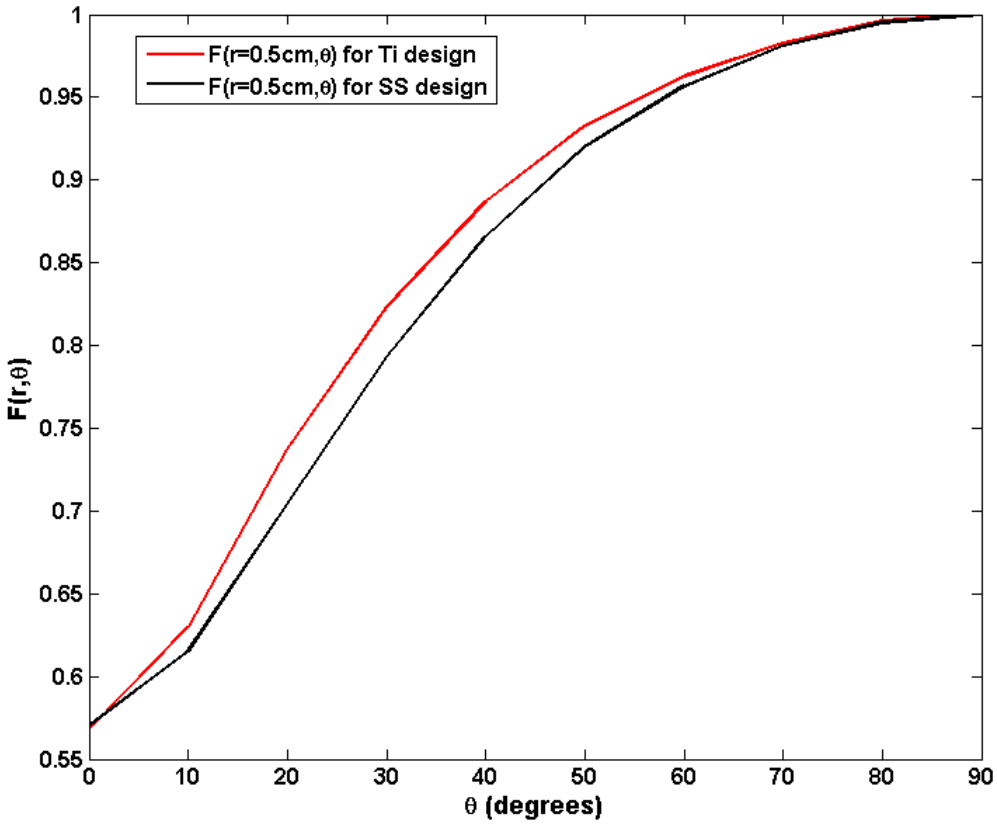

Figure 3.3.2 2D Anisotropy function $F(r,\theta)$ at $r = 0.5\,cm$ for both source encapsulation designs.

CHAPTER 4

MONTE CARLO MODEL OF A PHILLIPS RT-250 ORTHOVOLTAGE MACHINE

It has been demonstrated [13, 14, 27] that a low-energy photon spectrum such as that of an Yb-169 brachytherapy source results in the most favorable change in photoelectron yield, and a substantial increase in energy deposition during GNRT. In order to demonstrate the feasibility and effectiveness in actual GNRT scenarios, this finding needs to be investigated via *in-vivo* and *in-vitro* studies. A brachytherapy source design such as the one specified in Chapter 2 would be cost-prohibitive for such studies because it is currently unavailable from a commercial vendor, and would require significant design and manufacturing efforts for custom production. Moreover, the use of a brachytherapy source would significantly increase the complexity of the study by placing added requirements for adequate source handling and dosimetry. Thus, this part of the research is aimed at matching the general dosimetric characteristics of an Yb-169 source using an external x-ray beam from a Phillips RT-250 orthovoltage x-ray machine. This approach substantially reduces the source-related burden during radiobiology studies of GNRT with an Yb-169 source. In this study, an MC model of a Phillips RT-250 orthovoltage machine is developed and validated. A model of this type would allow for the study of beam filtration and subsequent modification of the photon spectrum. The goal is to obtain a flexible model that allows the freedom to place a filter of any material, of any size, at any location and rapidly determine its effects on the photon spectrum and PDD of the modified x-ray beam.

4.1 Monte Carlo Model

The original x-ray beam was studied through the development of an MCNP model of the Phillips RT-250 orthovoltage machine. The geometry of the machine housing, filtration, and applicators were defined in MCNP as shown in Figure 4.1.1. The model includes the vacuum region, beryllium window, all collimators, and the inherent copper filtration. The geometry of all the internal structures of the machine are not available from the manufacturer and were deduced from published literature [57] and physical measurements for MCNP modeling of the machine head. The bremsstrahlung production from the target was not modeled in the interest of computing efficiency. Instead, the bremsstrahlung spectrum released from the tungsten target was obtained from the software package SpekCalc [58-60], a well-validated x-ray spectrum generator that analytically computes the bremsstrahlung spectrum. The calculated x-ray spectrum was inserted into the model as a photon point source at the position where the electron beam would impact the tungsten target.

The Phillips RT-250 orthovoltage machine was modeled for the following three kilo-voltage beam settings: 75 kVp, 125 kVp, and 250 kVp. The 75 kVp and 125 kVp beams are filtered only by the inherent filtration of the machine, while the 250 kVp beam is filtered by 0.25 mm Cu as well as the inherent filtration of the machine. Figure 4.1.1 shows a cross-sectional view and a three-dimensional view of the machine head geometry used to model kilo-voltage beams from the Phillips RT-250 orthovoltage machine.

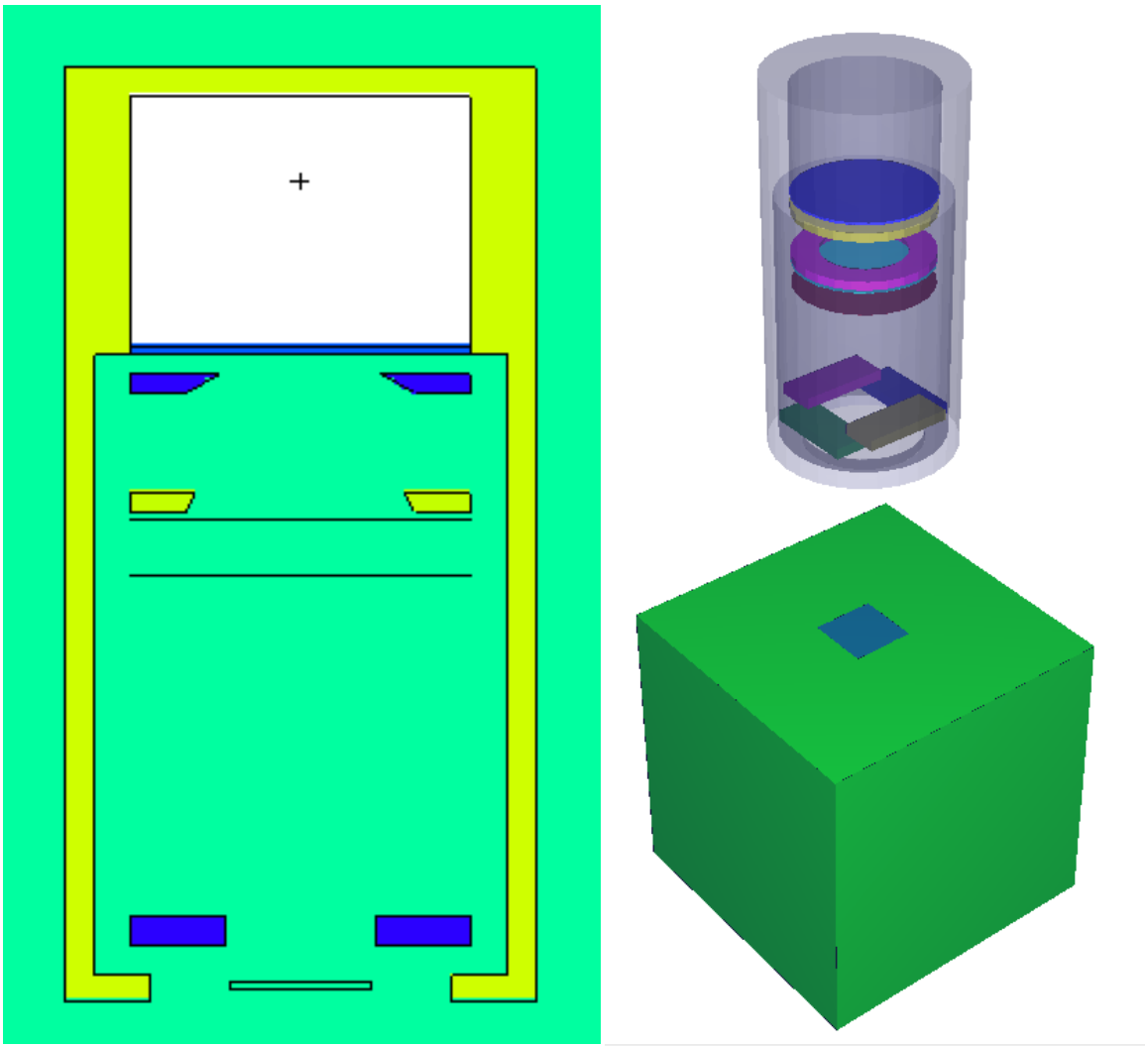

Figure 4.1.1 MCNP geometry for Phillips RT-250 orthovoltage machine model. LEFT: Cross-sectional view of machine head model. Geometry includes vacuum region, beryllium exit window, copper and lead cone collimators, and square lead collimators. RIGHT: Three-dimensional view of the MCNP geometry used for simulation showing the position of the water phantom at 50 cm SSD.

The photon spectrum for each beam (i.e. 75 kVp, 125 kVp and 250 kVp) was calculated using the average flux MCNP F4 tally in air right after all collimation. A 30 x 30 x 30 cm^3 water phantom was used to compute the PDD along the central axis of the phantom for standards conditions of a $10\ cm \times 10\ cm$ field size at 50 cm SSD. Cylindrical cells of 4 cm in diameter were used along the central axis to act as photon dose detectors. The height of the each cell was kept at 0.1 cm for the 1 cm region close to the surface. The height was increased to 0.2 cm for the rest of the detectors along the central axis down to a depth of 20 cm. The MCNP5 energy deposition F6 tally was used to obtain the full depth dose data along the central axis. The number of histories used was set to $2x10^8$ in order to keep the relative uncertainty of each cell < 0.3%.

4.2 Experimental Validation of Photon Spectrum

The MC model was validated by comparing the spectra obtained via MC methods with measured x-ray spectra. The measurement of x-ray spectra can be a difficult task given the high photon flux of the source and the energy resolution requirements. Semiconductor detectors such as cadmium telluride (CdTe), cadmium zinc telluride (CdZnTe) and high-purity germanium (HP-Ge) are the preferred detector systems for x-ray spectrum measurements. HP-Ge detector systems require liquid nitrogen cooling systems that are expensive, large, and difficult to work with. CdTe and CdZnTe detector systems are capable of operating with a compact thermoelectric cooling system without the need of any external cooling. For this work, a CdTe detector system was chosen given its compact size, ease of operation, and readily available design.

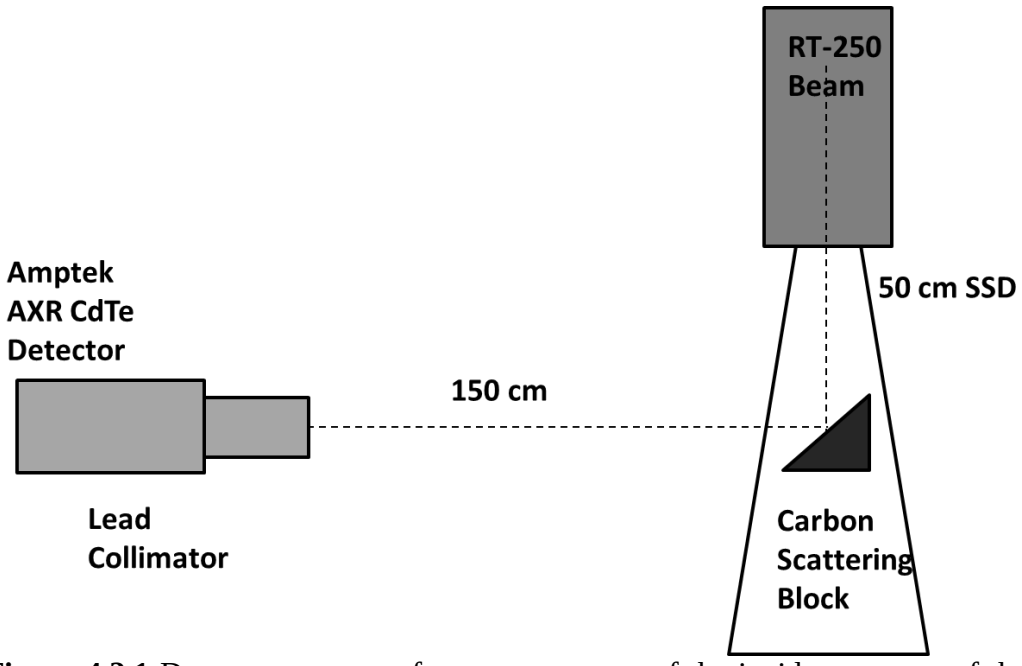

Figure 4.2.1 Detector geometry for measurements of the incident spectra of the Phillips RT-250 orthovoltage machine.

The choice of detection geometry remains another important aspect to consider in order to measure the x-ray spectrum properly. The high photon flux of the Phillips RT-250 orthovoltage source requires heavy collimation and large detector to source distances in order to avoid pulse pileup in the detector. These complications are avoided using a 90^o Compton scattering technique [61-64]. The technique requires a scattering medium and the measurement of the 90^o photon spectra that scatters off of the medium; this scattered spectrum is used to reconstruct the incident spectrum of the source. A low-Z scattering medium with no characteristic peaks such as Carbon (C) was chosen as the method developed by Maeda *et. al.* [65]. The detection geometry was arranged as shown in Figure 4.2.1 using a $3\ cm \times 3\ cm \times 3\ cm$ right triangular prism cut out of graphite, a common allotrope of C. The detection geometry also included a 2.5 mm-diameter lead collimator to ensure good discrimination of photons scattered at 90^o.

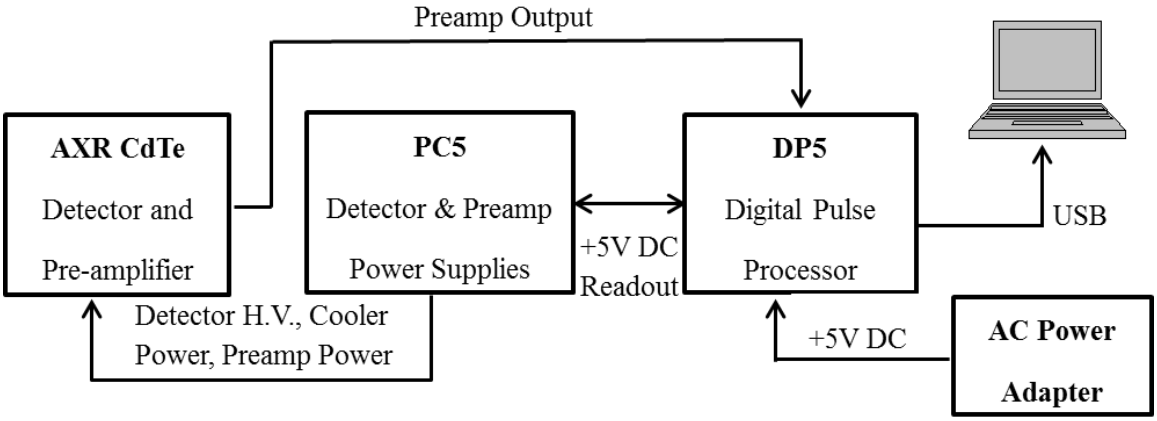

Figure 4.2.2 X-ray detection system for photon spectra measurements.

The detection system used is based on a pre-amplified and thermoelectrically cooled CdTe photodiode detector (AXR CdTe, Amptek Inc.). The detector crystal has a surface area of $5 \times 5\ mm^2$ and 1 mm in thickness with an energy resolution of < 1.5 keV at 122 keV (< 1.22 %) for ^{57}Co. The signal processing system (Figure 4.2.2) used in conjunction with the detector is composed of three major components: 1) a digital pulse detector (DP5, Amptek Inc.) that serves as the shaping amplifier and multichannel analyzer (MCA) and used in conjunction with the CdTe detector. 2) a detector power supply and PC interface board (PC5, Amptek Inc.) 3) a computer with Amptek DPPMCA display and acquisition software.

The collected spectra needs to be corrected for detector response, namely the escape of secondary x-rays and absorption efficiency. Each collected spectrum was corrected by applying a stripping procedure [65] specified by:

$$N_t(E_o) = \frac{N_d(E_o) - \sum_{E=E_o+0.5}^{E_{max}} R(E_o, E) N_t(E)}{R(E_o, E_o)} \tag{4.3.1}$$

where $N_t(E_o)$ is the true number of photons in energy E_o, $N_d(E_o)$ is the detected number

of scattered photons in energy E_o, E_{max} is the highest energy detected in the spectrum, $R(E_o, E)$ is the monoenergetic response function of the detector, and $R(E_o, E_o)$ is the full energy absorption efficiency. The process is applied step-wise starting at the maximum energy E_{max} down to the lowest energy $E_o + 0.5\ keV$.

The monoenergetic response functions and full-energy absorption efficiency for the CdTe detector was obtained via MC simulations using MCNP5. The model included the CdTe crystal ($5 \times 5 \times 1\ mm^3$), the top platinum (Pt) contact (0.2 μm), the bottom indium (In) contact (1 μm), and the Be window (100 μm). The detector geometry was exposed to 1 mm in radius monoenergetic beams of photons from 1 to 250 keV in 0.5 keV steps. The response function for each monoenergetic beam was calculated using the pulse height distribution MCNP F8 tally in the CdTe crystal. A total of 500 independent input decks were simulated to compute all of the necessary response functions and the full energy absorption peak efficiency as shown in Figure 4.2.3.

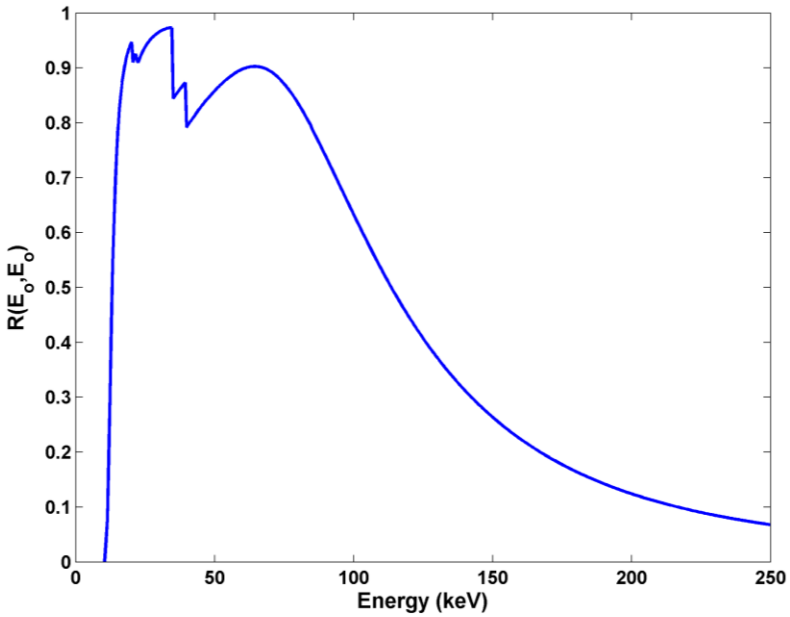

Figure 4.2.3 Full energy absorption peak efficiency of Amptek AXR CdTe detector.

The 90^o photon spectrum corrected for energy response is used to reconstruct the incident spectrum via the Klein-Nishina formula. The energy of an incident photon $h\nu$ scattered by 90^o and detected as $h\nu'$ is given by:

$$h\nu = \frac{h\nu'}{1 + {h\nu'}/{m_e c^2}} \tag{4.3.2}$$

where m_e is the rest mass of an electron and c is the speed of light in vacuum. The Klein-Nishina formula yields the differential cross section of photons scattered from a single electron per unit solid angle and written as:

$$\frac{d\sigma}{d\Omega} = Zr_o^2 \left(\frac{1}{1+\alpha(1-\cos\theta)}\right)^2 \left(\frac{1+\cos^2\theta}{2}\right) \times \left(1 + \frac{\alpha^2(1-\cos\theta)^2}{(1+\cos^2\theta)(1+\alpha(1-\cos\theta))}\right) \tag{4.3.3}$$

where Z is the atomic number of the scattering medium, $r_o$is the classical electron radius, $\alpha = h\nu \,/\, m_e c^2$, and θ is the scattering angle. The fraction of photons scattered into $\theta = 90^o$is given by:

$$\frac{d\sigma/d\Omega\,|_{\theta=\frac{\pi}{2}}}{d\sigma/d\Omega\,|_{\theta=0}} = \frac{1}{2}\left(\frac{1}{1+\alpha}\right)^2 \left(1 + \frac{\alpha^2}{1+\alpha}\right) \tag{4.3.4}$$

Therefore, the incident spectrum $\Phi_o(h\nu)$ can be reconstructed from the scattered 90^o spectrum $\Phi_s(h\nu')$ as [65]:

$$\Phi_o(h\nu) = \frac{\Phi_s(h\nu')}{\frac{1}{2}\left(\frac{1}{1+\alpha}\right)^2 \left(1 + \frac{\alpha^2}{1+\alpha}\right)} \tag{4.3.5}$$

The Klein-Nishina formula assumes an unbound and stationary electron in the derivation of equation 4.3.3. The drift velocities of electron in the scattering medium result in Doppler broadening of the characteristic peaks of the spectrum. This broadening can be removed by deconvolution of the characteristic peaks by [64]:

$$\Phi_o'(h\nu) = \Phi_o(h\nu) - \frac{T}{3m_e c^2}\left(\frac{h\nu}{h\nu'}\right)^2\left[\frac{d^2\Phi_o(h\nu)}{d(h\nu)^2}[(h\nu')^2 + (h\nu)^2] + 2h\nu\frac{d^2\Phi_o(h\nu)}{d(h\nu)^2}\right] \quad (4.3.6)$$

where T is the mean kinetic energy per electron in the scattering medium and equal to 0.2842 keV in carbon [66]. This quantity is deduced from the virial theorem, that states that the kinetic energy per electron is approximately equal to the absolute value of the biding energy per electron [67]. The deconvolution therefore looks at the first and second derivatives of the photon spectrum around each characteristic peak and should only be applied around the energy interval directly adjacent to the energy bins corresponding to a characteristic peak.

The 90^o measured spectrum and resulting final reconstructed spectrum are shown in Figure 4.2.4 for the 250kVp beam filtered by 0.25 mm Cu. The rest of the measured and reconstructed final spectra for 75 kVp, 100 kVp, and 125 kVp are shown in Appendix B. Figure 4.2.4 shows the measured spectrum by the detector (red dashed line) and the detector response-corrected spectrum (solid blue line). It can be appreciated after response correction there is an over-response in the lower energy region of the spectrum, and an under-response in the higher energy region as the absorption efficiency of the detector decreases. The Compton-corrected spectrum (black square-solid line) appropriately shifts the spectrum towards the higher energy of the incident spectrum. The

characteristic peaks are now shown in the correct region for tungsten, namely 59.3 keV (K_α) and 67.2 keV (K_β). The solid black curve shows the final reconstructed incident spectrum, correcting for the Doppler broadening of the characteristic peaks.

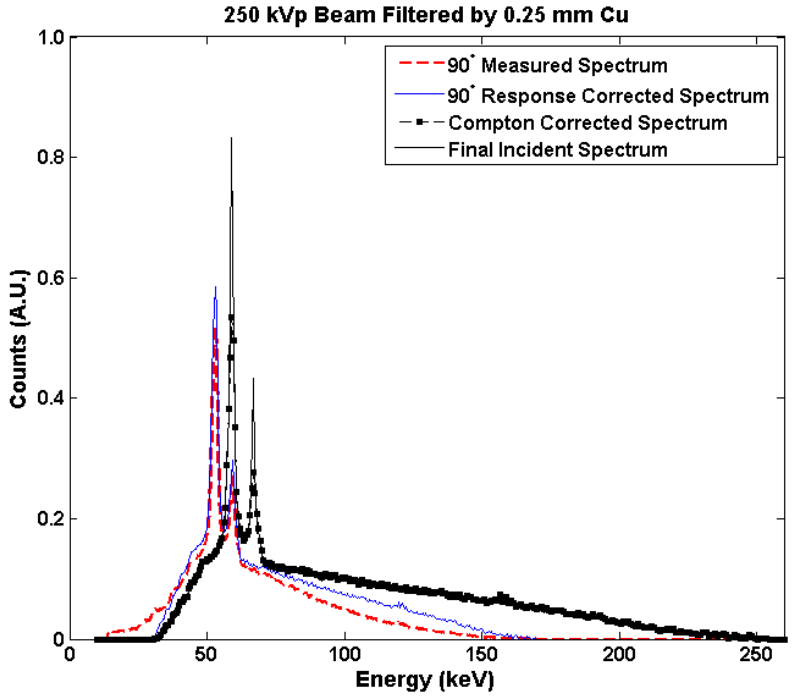

Figure 4.2.4 Measured 90^o spectrum and reconstructed incident spectrum for the 250 kVp beam filtered by 0.25 mm Cu.

The reconstructed incident spectrum for each beam was compared to the corresponding spectrum from MC simulations and shown in Figures 4.2.5-4.2.7. All of the results show reasonable agreement between the two spectra, validating the MC model for the Phillips RT-250 orthovoltage machine. Some disagreement is present due to errors arising from the complex nature of the measurement and reconstruction procedure. The poor energy resolution of the reconstructed spectra and any extra scatter due to the collimation geometry can also be attributed to the disagreement.

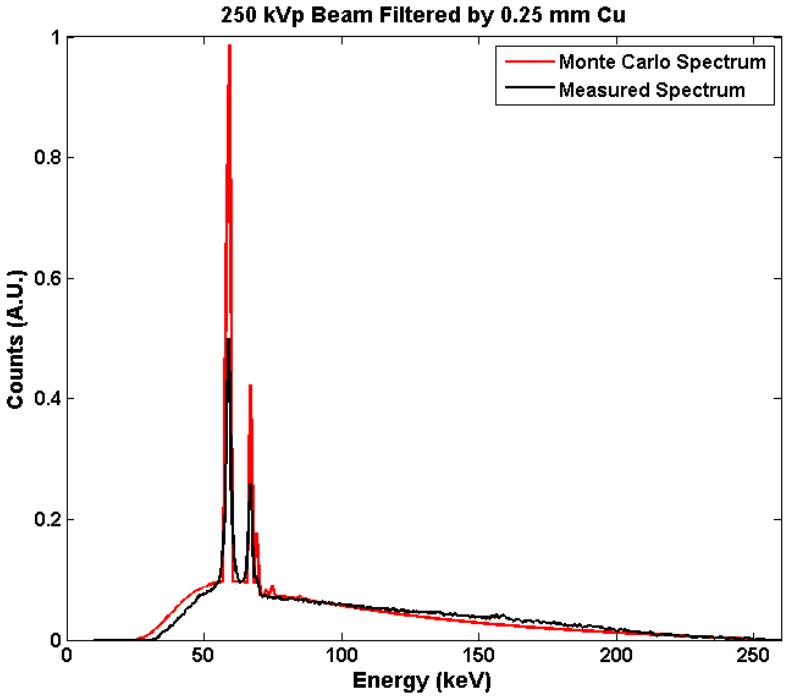

Figure 4.2.5 Photon spectrum validation of 250 kVp beam.

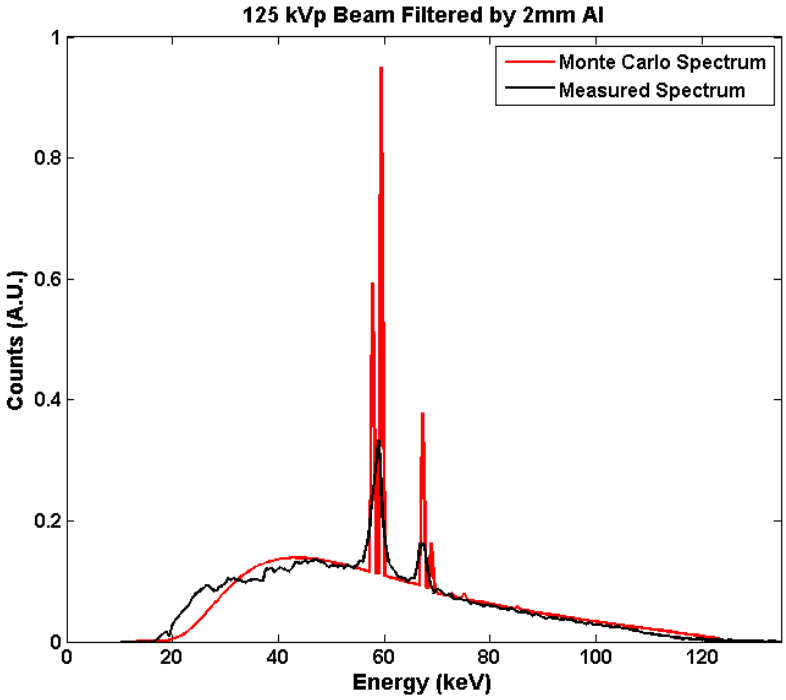

Figure 4.2.6. Photon spectrum validation of 125 kVp beam.

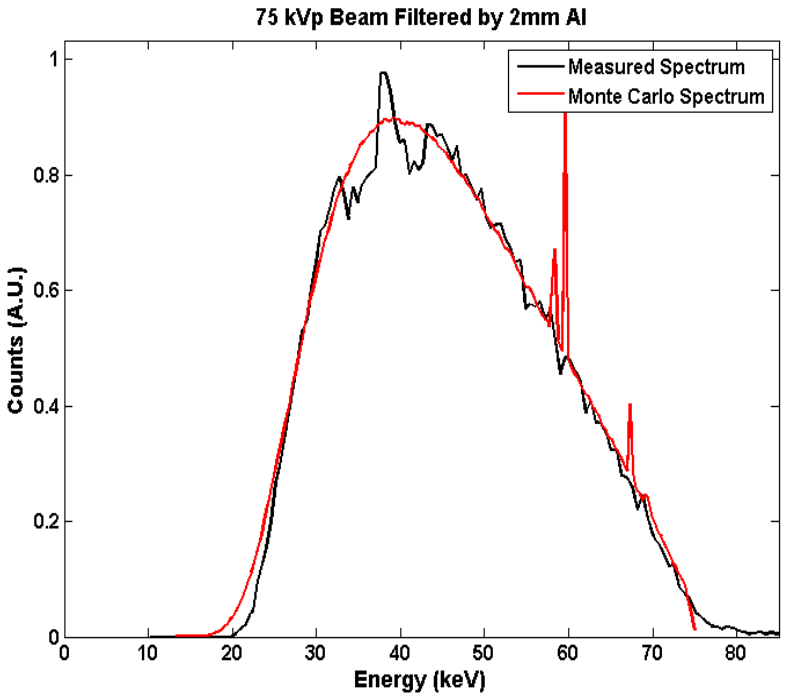

Figure 4.2.7 Photon spectrum validation of 75 kVp beam**.**

4.3 Experimental Validation of Percent Depth Dose

In order to further confirm the validity of the MC model of the Phillips RT-250 orthovoltage machine, PDD data were measured and compared against MC results. PDD is one of the key dosimetric quantities closely associated with the radiation quality of a radiotherapy beam and utilized as a means to verify the beam energy. Dose distribution can be measured using ion chambers, diode detectors or film dosimetry. Film dosimetry provides high spatial resolution and therefore is preferred for collecting dose information in high dose-gradient regions. Gafchromic EBT films (Ashland Inc., Covington, KY) are a type of radiochromic film that has the capability to provide relative and absolute dosimetry of radiotherapy beams. Radiochromic films instantly change color when exposed to ionizing radiation without the need of development or any post-processing.

The Gafchromic EBT film has low energy dependence [68], near-tissue equivalence [69], and a high spatial resolution (< 0.1 mm) [70].

The film was characterized and calibrated by establishing the dose response curve to convert net optical density (netOD) to dose following published methodologies [69, 71, 72]. For all film dosimetry measurements, films were taken from a single sheet of Gafchromic EBT film (lot # 47277-03I). For the calibration procedure 33 pieces ($4 \times 4\ cm^2$) were cut from a single sheet of film. The film was exposed to a range of doses from 0-7 Gy for the 250 kVp (0.25 mm Cu), three pieces for each dose level. The films were placed at a source-to-film distance of 50 cm and placed on top of a thin layer of transparent plastic tape, supported by a Styrofoam frame. The beam-output is determined following AAPM TG-61 [73] report which provides a formalism to calculate the dose at the surface of a full phantom using the following equation:

$$D_{w,z=0} = MN_k B_w P_{stem,air} \left[\left(\frac{\bar{\mu}_{en}}{\rho} \right)_{air}^{w} \right]_{air} \tag{4.4.1}$$

where M is the free-in-air chamber reading, corrected for temperature, pressure, ion recombination, polarity effect, and electrometer accuracy; N_k is the air-kerma calibration factor for the specific beam quality; B_w is the backscatter factor that accounts for phantom scatter; $P_{stem,air}$ is the chamber stem correction factor; and $[(\overline{\mu_{en}}/\rho)_{air}^{w}]_{air}$ is the ratio for water-to-air of the mean mass energy absorption coefficient averaged over the incident spectrum. Equation (4.4.1) yields the dose to water from a free-in-air chamber reading and the Accredited Dosimetry Calibration Laboratory (ADCL) provides the chamber calibration factor N_k in air. Consequently, by removing the backscatter

factor B_w, the dose in air to a water medium is obtained, and film pieces were exposed in air to known doses in a water medium [69].

The doses delivered to the films ranged from 0.4 to 7.0 Gy for a total of 10 dose levels with 3 film pieces for each exposure. The films were scanned approximately 24 hours after exposure using an Epson Expression 10000XL (Epson America, Inc. Long Beach, CA) flat-bed document scanner in transmission mode. The scanned images were obtained in 48-bit RGB color mode and saved in tagged image file format (TIFF). A cardboard template with a $4 \times 4\ cm^2$ cut-out was used on the scanner to position each film at a reproducible and central location on the scanner while blocking out the rest of the scanning area. The images were processed using the public domain imaging processing software ImageJ (National Institute of Health, Bethesda, MD) [74] to measure the intensity (I) and standard deviation (σ_I) for each film as a mean pixel intensity value over a centralized region of interest.

The $netOD^i$ value for each independent film exposed to a dose value D_k is defined as [71]:

$$netOD^i(D_k) = \log_{10}\left(\frac{I_{unexp} - I_{bckg}}{I_{\exp}(D_k) - I_{bckg}}\right) \tag{4.4.2}$$

where $I_{unexp}$is the film intensity for an unexposed film piece (i.e. $D = 0\ Gy$), I_{bckg} is the intensity with zero-light transmission, and $I_{exp}(D_k)$ is the film intensity for dose D_k. The average $netOD(D_k)$ is calculated as a weighted average of the three individual $netOD^i$:

$$netOD(D_k) = \frac{\sum_{i=1}^{3} netOD^i(D_k) \Big/ \left[\sigma^i_{netOD}(D_k)\right]^2}{\sum_{i=1}^{3} 1 \Big/ \left[\sigma^i_{netOD}(D_k)\right]^2} \tag{4.4.3}$$

The dose response curves for all three channels (red, green, and blue) are shown in Figure 4.3.1 and show the dose response of each separate channel as a function of dose delivered. Figure 4.3.2 shows the sensitivity curve for all three channels. The sensitivity curve was calculated by numerically taking the first derivative of the dose response curve. It can be observed from both curves that for all the dose levels used in this study, the red channel consistently yields the highest values of $netOD$ as well as sensitivity. At dose levels below $\leq 2\ Gy$ the sensitivity is anywhere between 50 – 85 % higher than the green channel and around 200 – 300 % higher than the green channel. The red and green channel yield similar sensitivities at doses above $5\ Gy$ and roughly 100 % higher than the blue channel. Therefore, the red channel was chosen to process all film dosimetry throughout this study.

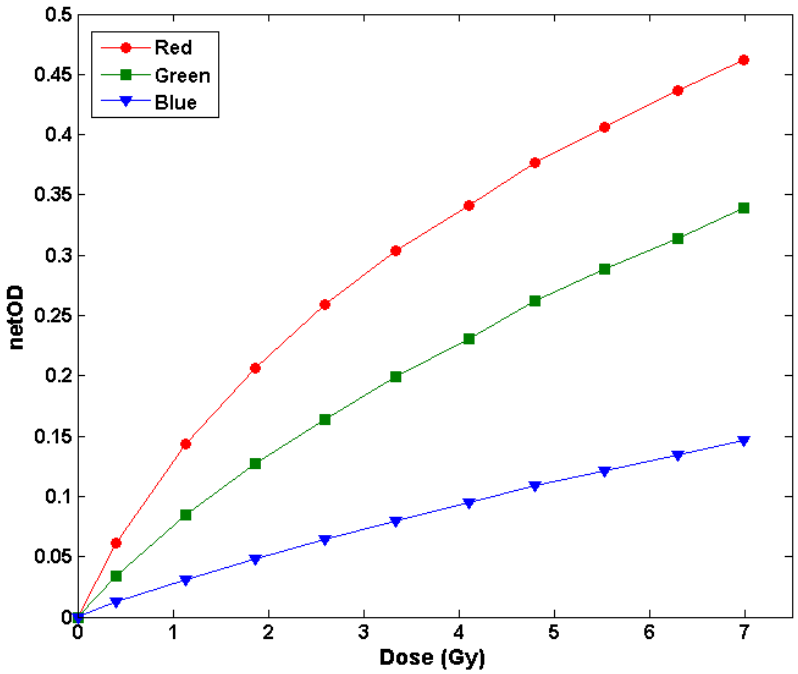

Figure 4.3.1 Dose calibration curve for the 250 kVp beam for all three color channels.

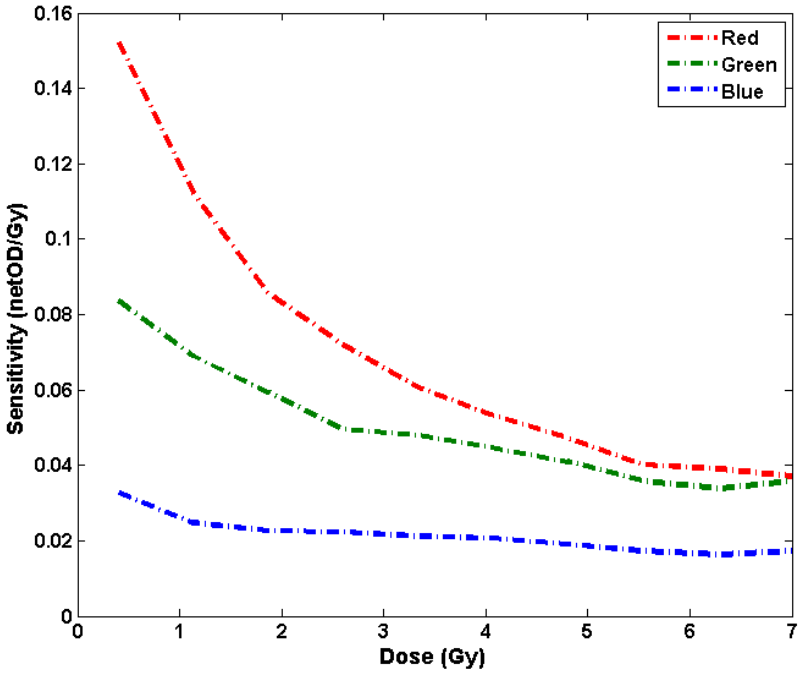

Figure 4.3.2 Dose sensitivity curve for the 250 kVp beam for all three color channels.

The PDD was measured using the calibrated EBT film from the same lot (lot # 47277-03I) cut into rectangular strips of $4 \times 20.3\ cm^2$. The strips were positioned in between 6 cm slabs of solid water (Gammex, Inc. Middleton, WI) and irradiated with the 0.25 mm Cu 250 kVp beam at reference condition (SSD 50 cm, $10 \times 10\ cm^2$). The solid water was chosen in order to perform quick measurements of the PDD, while avoiding the setup of a liquid water phantom. The films were scanned using the same procedure used in the calibration study, using a cardboard cut-out of 4×20.3 cm to consistently place the films on the center of the scanner. A post-processing script was written in MATLAB 7.13.0.564 (Mathworks ®, Natick, MA) to apply the dose calibration and extract the PDD curve. The PDD curve was measured twice and averaged to obtain the final measured PDD for the 0.25 mm Cu 250 kVp beam.

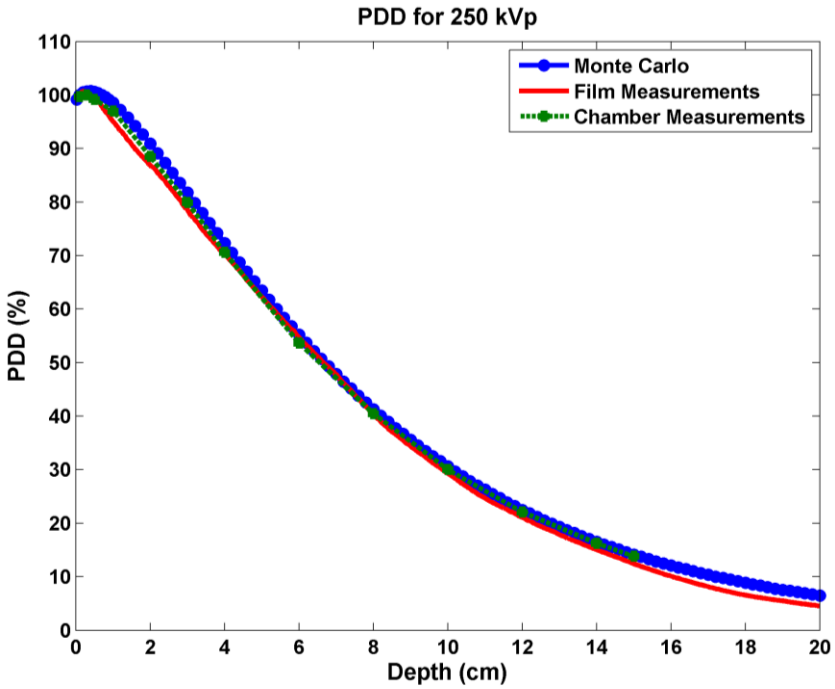

Figure 4.3.3 Percent depth dose validation for 250 kVp beam. MC results are compared against film and chamber measurements.

The MC results for the PDD curve of the 250 kVp beam were compared with film measurements and the comparison is shown in Figure 4.3.3. The match between the two curves was considered acceptable for all depths with a maximum difference between PDD values of 4 % at a depth of 2 cm (90.9 % versus 86.9 %) but remained under 2 % for most depths. This was considered acceptable given the limitations of the film measurement for orthovoltage beams and the use of solid water as opposed to performing measurements in a liquid water phantom. These limitations include beam attenuation of the orthovoltage beam through the film and solid water material which can lead to changes in the dose calibration of the film [72]. Other possible explanations for some of the disagreement are uneven surface contact between the film and the solid water. Although great care was taken to avoid air pockets between the film and the solid water,

this can still affect the measurements. Lastly, any small deviation in alignment can also affect the measurements specially when dealing with an orthovoltage beam.

The MC results and the film measurements for the 250 kVp beam were also compared with the ion-chamber-measured PDD data (CC-04, Scandatronix/Wellhofer, Schwarzenbruck, Germany) obtained from the machine data book and deduced from published literature [72]. The agreement with the ion-chamber measurements was an improvement over the film measurement (Figure 4.3.3) with a maximum difference between PDD values of 2.1 % (88.8 % versus 90.9 %) at a depth of 2 cm. The disagreement between the two curves remained under 1.5 % for all other depths. This agreement was acceptable again considering the orthovoltage nature of the beam and the volume averaging errors that arise from the ion-chamber measurements. The poor spatial resolution of the ion-chamber measurements around the build-up region give rise to discrepancies in the PDD curve that do not exist in the MC results.

The MC PDD curves were also compared with ion-chamber data for the 75 kVp and 125 kVp beams and the results are shown in Figures 4.3.4 and 4.3.5. The results show close agreement between both curves with some discrepancies similar to those of the 250 kVp. The 125 kVp PDD data reached a maximum disagreement of 3 % (73.2 % versus 70.2 %) at a depth of 2 cm and remained under 2.5 % for all other depths. The 75 kVp PDD data reached a maximum disagreement of 2.2 % (86.6 % versus 88.8 %) at a depth of 0.5 cm but remained under 1 % for all other depths.

Overall, the MC PDD results and ion-chamber measurements showed good agreement for the whole range of kilo-voltage settings (75 kVp through 250 kVp). This agreement demonstrates the robustness and validity of the current MC model for the

Phillips RT-250 orthovoltage machine. The model is able to reproduce the spectral and dosimetric characteristics of the beam for any kilo-voltage setting and filtration, and allows the freedom to add any custom filter or setup. The model is able to accomplish this without the need to model the bremsstrahlung production of x-rays in the machine head. This step significantly reduces computation time by at least a couple of orders of magnitude, allowing for a flexible and fast simulation of the x-ray machine. Improvements in the accuracy of the model can be expected with improved information about the machine head geometry.

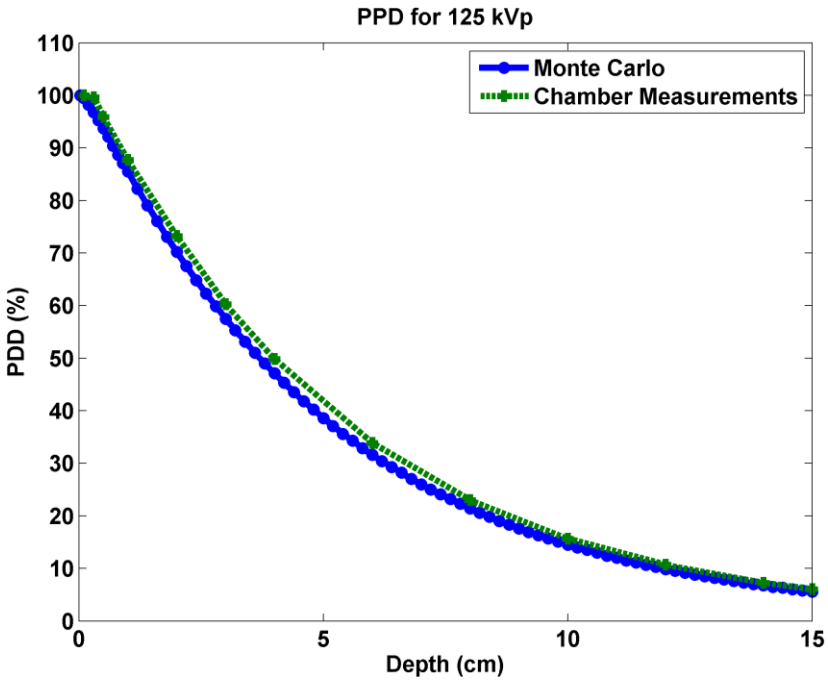

Figure 4.3.4 Percent depth dose validation for 125 kVp beam. MC results are compared against film and chamber measurements.

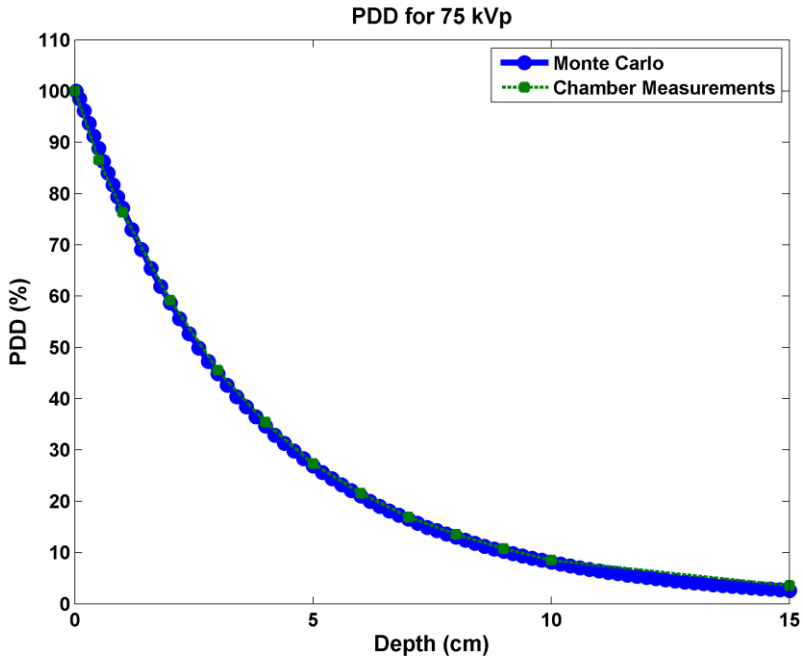

Figure 4.3.5 Percent depth dose validation for 75 kVp beam. MC results are compared against film and chamber measurements.

CHAPTER 5

YTTERBIUM-169 SOURCE EMULATION

This part of the project is aimed at emulating the dosimetric and spectral characteristics of an Yb-169 brachytherapy source using a Phillips RT-250 orthovoltage x-ray machine. The fundamental differences between a brachytherapy source and an external source of radiation make the development of a perfect replacement for the source an unlikely outcome, and not the intended purpose of the study. Thus, this task seeks to establish the best available surrogate of the Yb-169 brachytherapy source using the orthovoltage x-ray machine, such that it facilitates *in-vitro* and *in-vivo* studies of GNRT. The gamma-ray spectrum of Yb-169 has an intensity-weighted average energy of just 92.8 keV, with more than half of the photons with energies between 49 and 63 keV. Therefore, the initial goal of the project is to reproduce the region around 49 to 63 keV photons via filtration of the RT-250 orthovoltage beam, thereby reproducing the general characteristics of the photon spectrum.

5.1 Photon Spectrum Approximation

Table 5.1.1 Available beams from the Phillips RT-250 orthovoltage machine.

Peak kilovoltage (kVp)	***Filtration***
75	*inherent*
100	*inherent*
125	*inherent*
250	*0.25 mm Cu*
250	*0.4 mm Sn + 0.25 mm Cu*

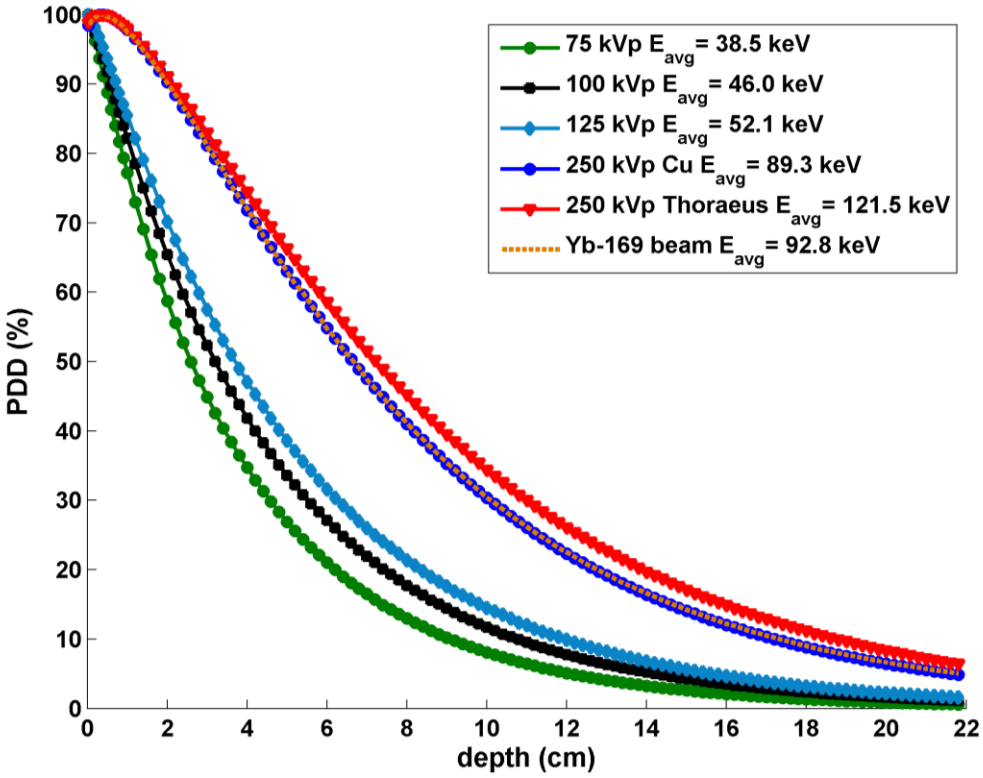

Figure 5.1.1 Photon spectrum and intensity-weighted average energy for all available beams from the Phillips RT-250 orthovoltage machine.

The model and methodology described in the previous chapter was used to compute the photon spectrum for all available x-ray beams on the Phillips RT-250 x-ray machine outlined in Table 5.1.1. The results presented in Figure 5.1.1 show the photon spectrum of each beam along with its corresponding intensity-weighted average energy. The average energy ranges from 38.5 keV for the 75 kVp beam all the way up to 121 keV for the thoraeus-filtered (0.4 mm Sn + 0.25 mm Cu) 250 kVp beam. The copper filtered 250 kVp beam has an average energy of 89.3 keV, the closest to that of the Yb-169 gamma-ray spectrum (92.8 keV). This beam would generate the strongest agreement with the dosimetric behavior of Yb-169 when compared to all other beam available from the RT-250 x-ray machine. However, the most intense part of the spectrum lies around the

characteristic x-rays from the tungsten target at around 59.3 keV (K_α) and 67.2 keV (K_β), higher than the major peaks in the Yb-169 gamma-ray spectrum (Figure 1.1.1). The region around these major peaks contains about two-thirds of all photons in the Yb-169 gamma-ray spectrum and is mostly responsible for the dose enhancement expected from the use of an Yb-169 source during GNRT. Therefore, while the copper-filtered 250 kVp beam yields a close approximation to the Yb-169 spectrum in terms of the average energy, an attempt is made to improve this approximation by reproducing the strong spectral lines of the Yb-169 around ~49 and ~63 keV by further filtering the copper-filtered 250 kVp beam.

The filtering of any x-ray beam normally results in the hardening of the beam with an overall increase in the average energy of the spectrum. However, many metals can affect the properties of the spectrum in many different ways. This is accomplished by exploiting the K-edge and subsequent increase in attenuation above certain energies. Furthermore, some metals are capable of producing fluorescence photons in the kilo-voltage region that can be used to produce photons at a specific energy. This technique would serve to replace a portion of the attenuated photons in the original x-ray spectrum with fluorescence x-rays at a lower energy, effectively tuning the quality of the x-ray spectrum. A similar technique is routinely used in mammography imaging studies [75-77] to filter the high energy portion of a spectrum with the aim of improving contrast and reducing the dose to the patient. This method is known as K-edge filtering and it involves the use molybdenum (Mo) or rhodium (Rh) to filter out photons above the K-edge of the filter material. Molybdenum and rhodium are chosen because the K-edge energies lie right below the region of the spectrum that needs to be filtered, and are equal to 20.0 keV

and 23.2 keV respectively, effectively tuning the photon spectrum to the desired level.

In the case of the current study, the x-ray spectrum needs to be modified to reproduce the strong spectral lines of Yb-169 at around ~50 keV. Following this logic, an erbium (Er) foil was chosen as a filter material because it has a K-edge energy of 57.49 keV which lies just below the characteristic peaks from the tungsten target in the RT-250 x-ray machine. More importantly, the K-edge fluorescence peaks of Er match the features of the Yb-169 gamma-ray spectrum with energies of 49.1 keV (K_α) and 55.7 keV (K_β). Figure 5.1.2 shows the resulting spectrum of the 250 kVp beam filtered by a 0.25 mm erbium foil compared to the original 250 kVp beam filtered by just copper.

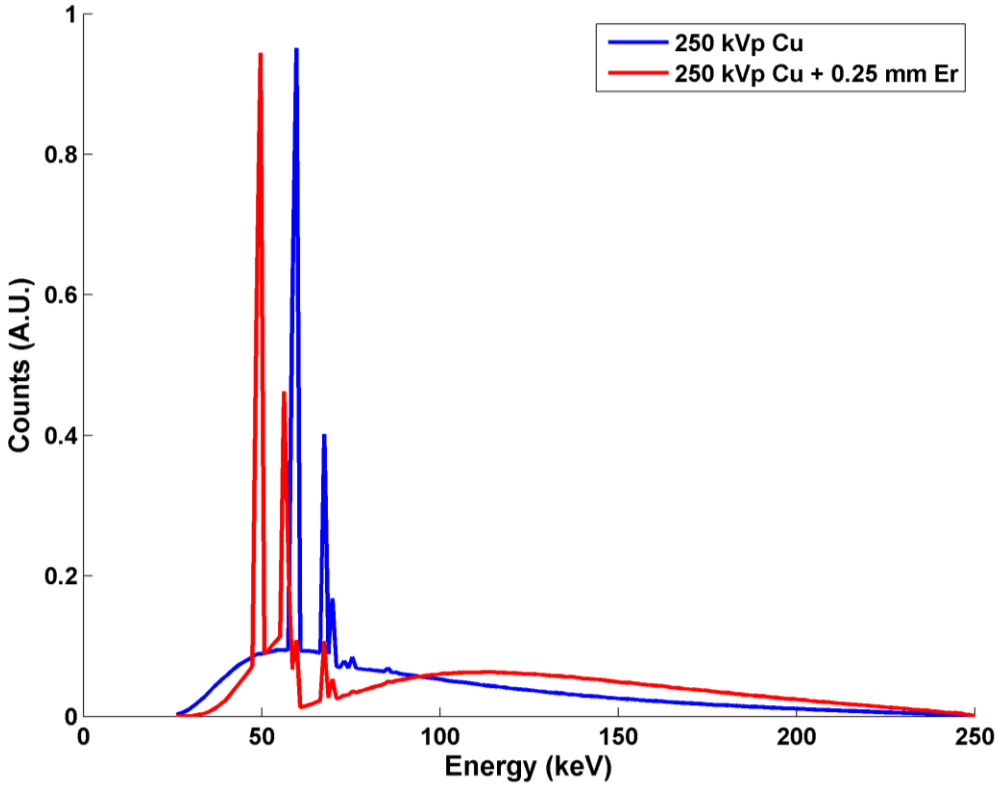

Figure 5.1.2 Photon spectrum of 250 kVp (Cu) compared to the same beam after the addition of a 0.25 mm erbium filter. The strong characteristic lines of tungsten on the original beam are suppressed and replaced with those of erbium at 49.1 keV and 55.7 keV.

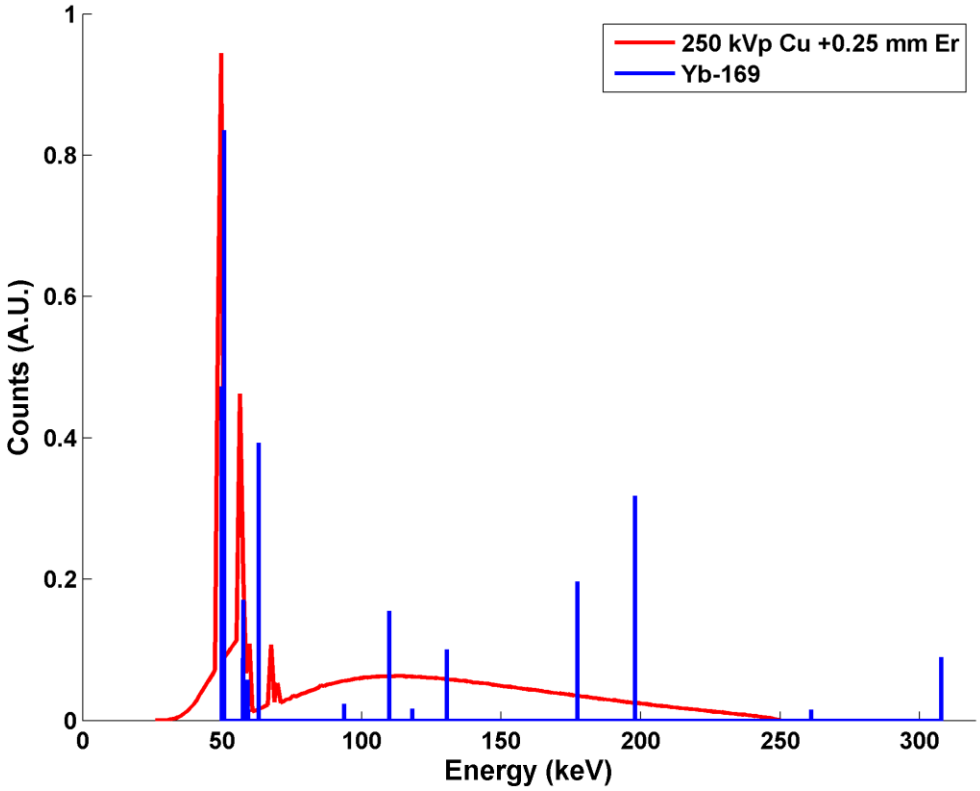

Figure 5.1.3 Photon spectrum of 250 kVp (Cu) after the addition of a 0.25 mm erbium filter compared to the photon spectra of Yb-169. The fluorescence photons from erbium at 49.1 keV and 55.7 keV match the strongest part of the Yb-169 spectrum.

Figure 5.1.3 compares the resulting spectrum with that of Yb-169 and illustrating the improved agreement in the desired region. The photon spectrum of the Er-filtered 250 kVp was measured using the 90^{o} Compton scattering technique described in the previous chapter. A $5\ cm \times 5\ cm \times 0.25\ mm$ Er foil (Sigma-Aldrich, St. Loius, MO) was placed along the beam path below the square lead (Pb) collimators on the machine head. The field size was set to $5\ cm \times 5\ cm$ at 50 cm SSD. The measured spectrum is shown in Figure 5.1.4 and is compared to the MC results. The results closely match each other demonstrating that the filtration technique is capable of producing the beam described

above. It should be noted that the measured spectrum lacks the necessary energy resolution to appropriately measure the fluorescence peaks of Er. This is a consequence of the Doppler broadening described in section 4.2 and the increased requirements on energy resolution placed by the deconvolution procedure defined by equation 4.3.6. The deconvolution procedure needs appropriate resolution around each characteristic peak in order to correctly deconvolve the spectrum and correct for the Doppler broadening on the carbon scatterer. Nonetheless, the agreement between the MC results and the measured spectrum is deemed acceptable considering the limitations of the technique.

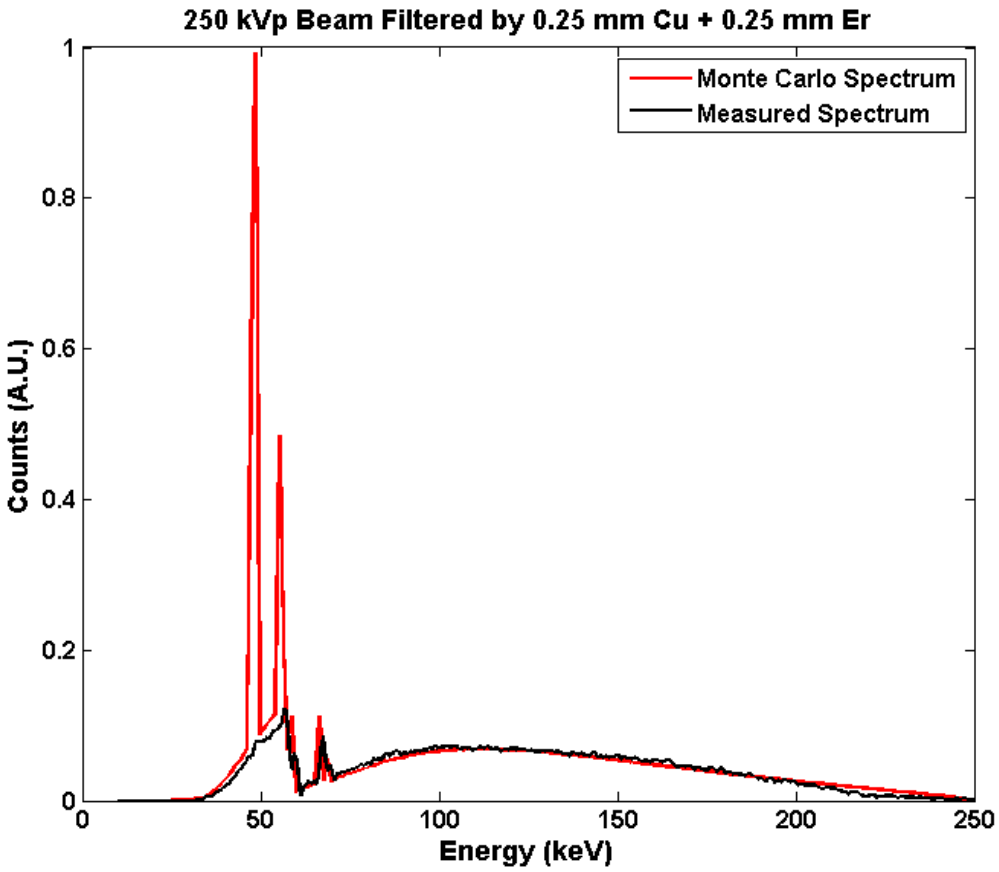

Figure 5.1.4 Photon spectrum of the Er-filtered 250 kVp calculated by MC results compared to measured results reconstructed from 90^{o} Compton scattering.

5.2 Percent Depth Dose Comparison

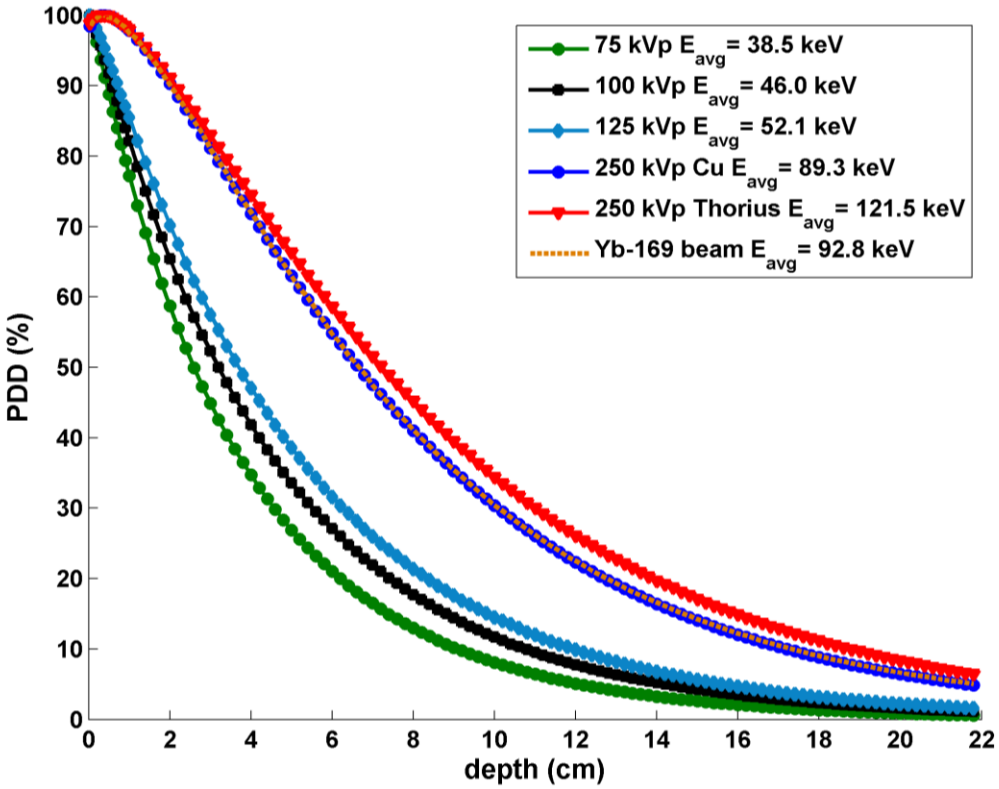

Figure 5.2.1 Percent depth dose comparison for all available beams from the Phillips RT-250 machine as well as a hypothetical Yb-169.

The PDD data for all available x-ray beams from the Phillips RT-250 orthovoltage machine were calculated using the MC model described in the previous chapter. In addition to the available beams, a hypothetical Yb-169 beam was created by replacing the photon point source of the orthovoltage machine with the photon spectrum of Yb-169. This beam was created in an attempt to investigate how the dosimetric characteristics of an Yb-169 brachytherapy source would compare to the available orthovoltage beams. Figure 5.2.1 shows the resulting PDD data for available beams along with the intensity-weighted energy of each beam. The 250 kVp beam filtered by 0.25 mm

of Cu showed remarkable agreement with the PDD curve of the hypothetical Yb-169 beam. This curve was also compared to the Er-filtered beam developed in section 5.1 and the results are shown in Figure 5.2.2. The results demonstrate that the addition of the Er filter modifies the photon spectrum of the orthovoltage machine without severely affecting the PDD curve of the 250 kVp Cu-filtered beam. Therefore, the modified beam is a better match to the Yb-169 source in terms of photon spectrum while still being able to emulate the PDD data of the Yb-169 source as demonstrated in Figure 5.2.2.

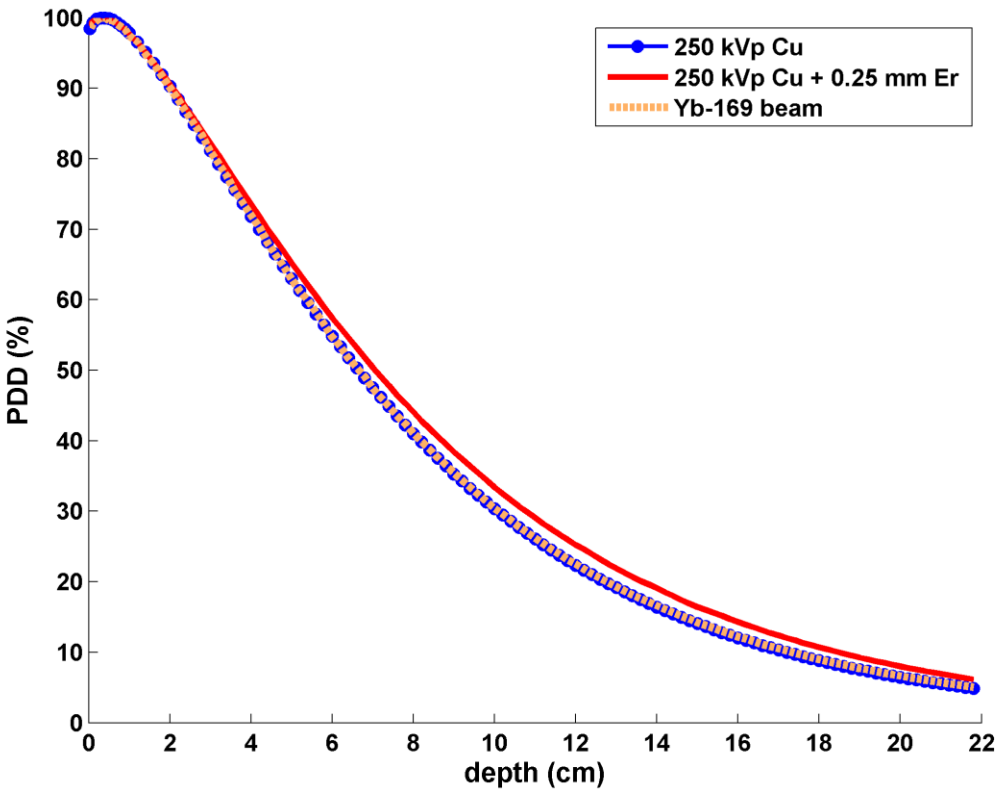

Figure 5.2.2 Percent depth dose data for the Cu-filtered 250 kVp beam and the Er-filtered 250 kVp beam.

5.3 Secondary Electron Spectra

In order to further evaluate if the filtered photon spectrum would more closely match the dosimetric characteristics of the bare Yb-169 spectrum during GNRT, the secondary electron spectrum for each beam is also compared. The condensed history Monte Carlo (MC) code EGSnrc [48] and user code DOSXYZnrc [49] were used to calculate the secondary electron spectrum for each one of the beams. The EGSnrc code was used for this task because the source code is immediately available for modification using the techniques described in section 2.6. The electron spectra were collected using logarithmically spaced bins covering a minimum energy of 0.025 keV up to the maximum energy of each spectrum with a minimum bin width of 25 eV.

The methodology was used to compute the secondary electron spectra of a 1x1x1 cm^3 tumor on top of a 30x30x29 cm^3 phantom at 50 cm SSD. The source option used was that of a collimated rectangular beam from a point source with the photon spectrum defined as that obtained from the MCNP model. The material composition of the tumor and phantom was taken as four-component ICRU tissue (i.e. 10.1 % hydrogen, 11.1 % carbon, 2.6 % nitrogen and 76.2 % oxygen). The tumor was loaded with 7 mg of gold per g of tissue (0.7 % by weight) and the density appropriately increased to 1.007 g/cm^3. The spectrum was computed for the Cu and thoraeus-filtered 250 kVp beam, the Er-filtered beam and the hypothetical Yb-169 beam. The resulting photoelectron spectra shown in Figure 5.3.1 demonstrate the basic disparities between the spectra. The resulting electron spectra show the total number electrons originating from photoelectric absorption interactions for each beam (Electrons from atomic relaxation and Auger electron emission are not included in the spectra).

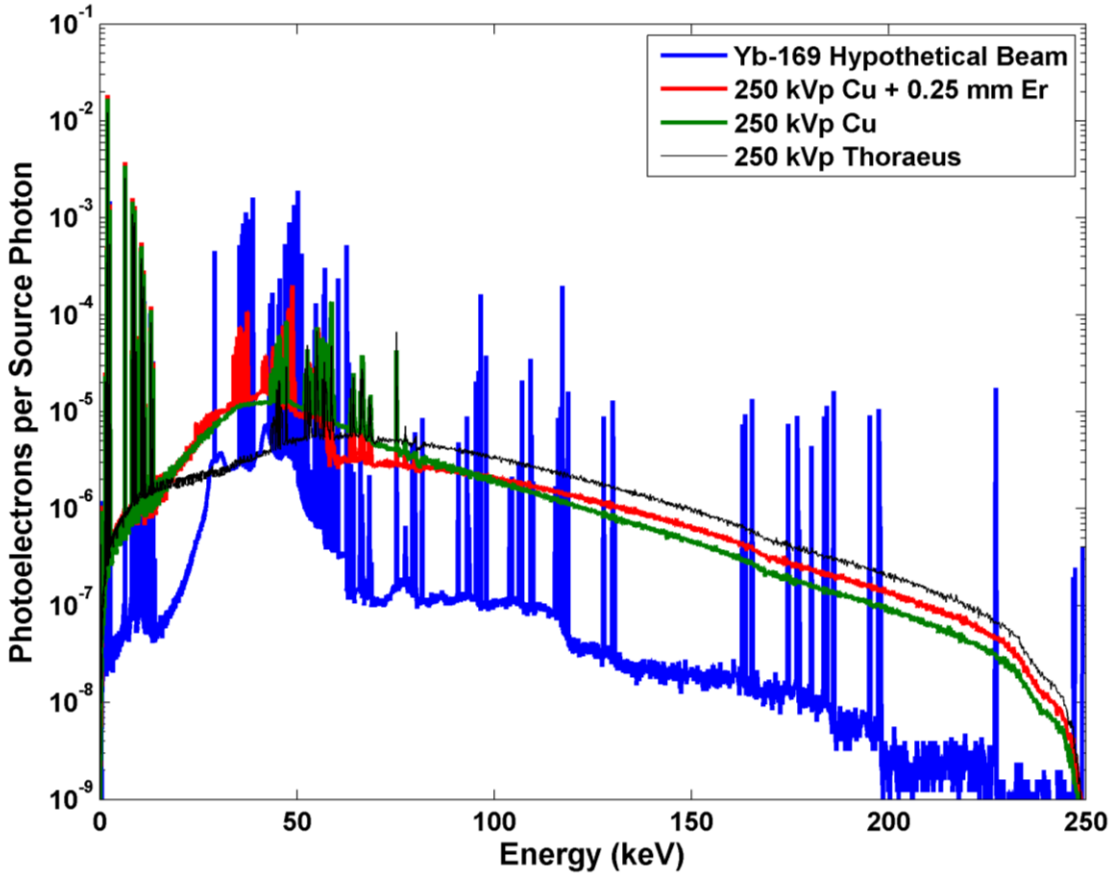

Figure 5.3.1 Spectra of photoelectrons released in the tumor region for each photon beam. The figure shows the spectrum from gold and tissue for the tumor loaded with 7 mg Au/g tissue.

Table 5.3.1 Total yield of photoelectrons (PE) and Auger/Coster-Kronig electrons (AE) and intensity-weighted total energy from gold and tissue for a tumor loaded with 7 mg Au/g of tissue for each separate beam. Auger/Coster-Kronig electrons are only produced in gold. All values listed in the table are normalized per source photon.

	Gold		*Tissue*			*Gold*	
Capsule Material	***Total PE Yield***	***Total PE Energy (keV)***	***Total PE Yield***	***Total PE Energy (keV)***	***Total PE Energy (keV)***	***Total AE Yield***	***Total AE Energy (keV)***
Yb-169	*0.0142*	*0.618*	*0.00930*	*0.365*	*0.983*	*0.0264*	*0.0983*
250 kVp Cu	*0.0139*	*0.564*	*0.00790*	*0.299*	*0.863*	*0.0257*	*0.101*
250 kVp Cu+Er	*0.0152*	*0.603*	*0.00964*	*0.334*	*0.937*	*0.0282*	*0.110*
250 kVp Thoraeus	*0.00999*	*0.464*	*0.00380*	*0.146*	*0.610*	*0.0186*	*0.0802*

The results presented in Figure 5.3.1 show the differences that arise in the photoelectron spectrum from the choice of each different beam. The thoraeus-filtered beam shows the largest disagreement with the Yb-169 source, as it fails to reproduce any of the strong spectral lines present in the photoelectron spectrum from the Yb-169 source. The Cu-filtered beam shows a much better agreement, corroborating the PDD and photon spectrum analysis as shown before. However, the Er-filtered beam manages to reproduce some of the strong spectral lines present in the Yb-169 spectrum around 50 keV, and show a much better agreement with the Yb-169 source. The Er-filtered secondary electron spectrum shows decreased photoelectron yield around ~57 keV due to the K-edge of Er and a sharp increase in the photoelectron yield around 50 keV due to the fluorescence photons, improving the matching with the Yb-169 spectrum.

Table 5.3.1 shows a quantitative assessment of the secondary electron spectrum for each one of the beams. The table lists the total photoelectron and Auger/Coster-Kronig electrons per source photon from gold and tissue separately, as well as the total energy from such electrons per source photon. This type of analysis gives insight into exactly how each beam locally deposits energy and how close the correlation is between each one of the x-ray beams and the Yb-169 source. The results show the Yb-169 beam with the highest total energy deposition of 1.08 keV per source photon. The thoraeus-filtered beam was in the largest disagreement depositing only 0.690 keV per source photon. This is stark difference between the two with a reduction of about 36 % in total energy transferred to electrons in the tumor region per source photons. The Cu-filtered beam showed much closer agreement with 0.964 keV deposited per source photon, but still 11 % lower than that of the Yb-169 source. On the other hand, the Er-filtered beam

showed the best agreement with the Yb-169 with a total of 1.05 keV deposited per source photon and just 2.7 % lower than the Yb-169 source.

5.4 Discussion

The best surrogate available for the Yb-169 source has been established as a 0.25 mm Er-filtered 250 kVp beam from the Phillips RT-250 orthovoltage machine. At a glance, the original Cu-filtered 250 kVp beam from the Phillips RT-250 machine may appear to be a good replacement with an intensity-weighted average energy of 89.3 keV, very close to the 92.8 keV of the Yb-169 source. An examination of the PDD data for each beam confirms remarkable agreement between the two and the best match out of all the standard beams from the Phillips RT-250 machine. However, a close approximation in PDD alone is insufficient to properly emulate the dosimetric characteristics of the Yb-169 source for *in-vivo* and *in-vitro* studies. As shown in this study, the incident photon spectrum plays a far more important role in reproducing the local energy deposition pattern of the Yb-169 source. Thus, a K-edge filtering and fluorescence production technique adopting an Er filter was used in this investigation to reproduce some of the gamma-ray lines of the Yb-169 spectrum. The presented results demonstrate a strong qualitative agreement between the spectra in the desired low energy region around 50 keV. The PDD data for this modified beam demonstrate that the addition of the Er filter does not dramatically affect the PDD of the original beam and, still closely matching the PDD between the two beams.

The analysis of the secondary electron spectrum for each one of the beams corroborates that the Er-filtered 250 kVp beam more closely matches the dosimetric

characteristics of the Yb-169 source. This type of analysis provides a better perspective for the local energy deposition pattern due to each source during GNRT, and serves as an effective tool to gauge which beam would work as the best surrogate. The results clearly demonstrate that the improved correlation between the initial photon spectra directly results in much better agreement in the local energy deposition pattern.

CHAPTER 6

CONCLUSIONS

The research presented herein is based on various investigations aimed at the design and pre-clinical study of an Yb-169 brachytherapy source within the context of GNRT. The source design must meet the practical constraints for producing a brachytherapy source that is appropriate for clinical translation, while simultaneously being optimized for GNRT. The first task involves the encapsulation design of the Yb-169 source to ensure that the low-energy portion of the photon spectrum is preserved for maximal dose enhancement. The study focused on a total of four encapsulation designs of various materials and configurations, and the effects of these designs on the dose enhancement and radiosensitization during GNRT were scrutinized via MC models.

The MC results reflect the importance of careful consideration of the source design for a brachytherapy application of GNRT. The change in the photon spectrum through the encapsulation of the source affects the dose enhancement not only macroscopically but also microscopically on a cellular scale. The changes in the photon spectrum directly translate to changes in the photoelectron yield and consequently, to changes in the local energy deposition during GNRT. The results of this study consistently show the titanium encapsulation design to have favorable properties in terms of further improving dose enhancement and radiosensitization effects during GNRT. Titanium is a low-weight, high-strength material with the necessary structural integrity and biocompatibility to encapsulate the radioactive core of an HDR Yb-169 brachytherapy source. Titanium is considered an optimal material to encapsulate the core

while allowing minimal loss of photons, and more specifically, low-energy photons, through the capsule. Furthermore, the increased strength of titanium might provide the opportunity to further decrease the thickness of the capsule, thereby improving the dose enhancement characteristics of the source.

The second task of the research consists of the characterization of the optimized brachytherapy source via MC techniques by computing the AAPM TG-43 dosimetric parameters: anisotropy function, radial dose function, air kerma strength, and dose rate constant. The characterization was performed for the titanium encapsulation design, which was deemed an ideal candidate for an HDR brachytherapy source for GNRT, and compared with a more conventional stainless steel design. The 2D anisotropy function for the stainless steel source design reflects increased dose perturbations due to higher attenuation through the stainless steel as opposed to titanium. The reduced attenuation through the titanium encapsulation also improves the strength of the source by 10 % when compared to the stainless steel design.

The third task involves the development and validation of an MC model of the Phillips RT-250 orthovoltage x-ray machine. The MC results were corroborated with measured photon spectra and PDD data, validating the MC model that was developed. The validated MC model of the Phillips RT-250 machine was used in the development of an external x-ray beam that would emulate the dosimetric characteristics of the Yb-169 brachytherapy source during GNRT. The most appropriate surrogate of the Yb-169 brachytherapy source was established as an Er-filtered 250 kVp beam from the Phillips RT-250 machine. The Er-filtered 250 kVp beam directly translated to improved correlation between the secondary electron spectra of the modified beam and Yb-169.

The adopted approach ensures improved emulation of the local energy deposition characteristics of Yb-169, and was the best surrogate for the Yb-169 brachytherapy source among the beams investigated in this study.

In conclusion, the major goals outlined in the introduction of this dissertation were accomplished. The encapsulation design for an Yb-169 brachytherapy source was optimized for GNRT. An external beam surrogate of the Yb-169 source was developed to facilitate *in-vitro* and *in-vivo* studies of GNRT. There are several future tasks that naturally arise from the results of the current work. The first is the *in-vitro*/*in-vivo* study to test the effectiveness of GNRT with an Yb-169 source using the source emulation techniques described herein. The second task is the production of a titanium-encapsulated Yb-169 brachytherapy source as specified by the design described in Chapter 2. Specifically, the manufacturing procedures and appropriate welding techniques that are necessary for a titanium encapsulated source need to be investigated. The third task is the characterization of the produced Yb-169 source for clinical brachytherapy dosimetry following the AAPM TG-43 report. The last task is the corroboration of the expected dose enhancement characteristics as predicted by the current study.

APPENDIX A
PHOTOELECTRON SPECTRA

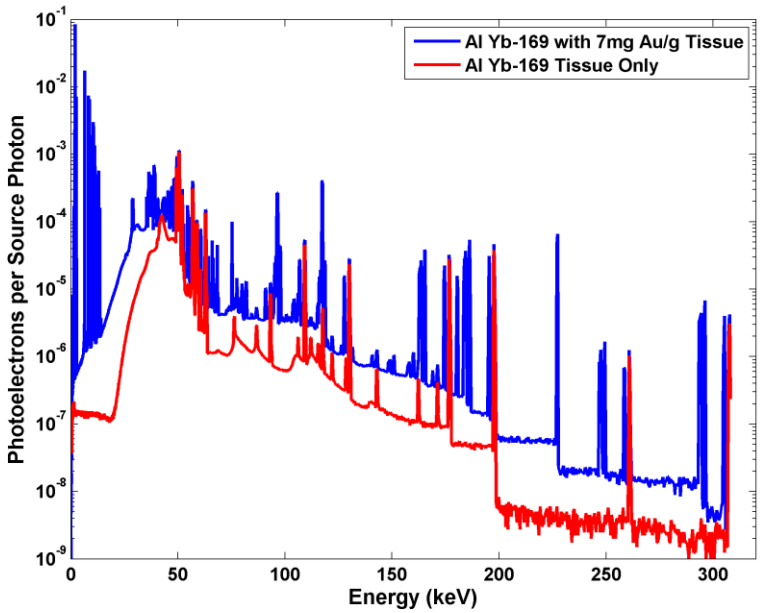

Figure A.1 Spectrum of photoelectrons released in the tumor region for the aluminum encapsulation design. The figure shows the spectrum from gold and tissue for the tumor loaded with 7 mg Au/g tissue and from tissue case.

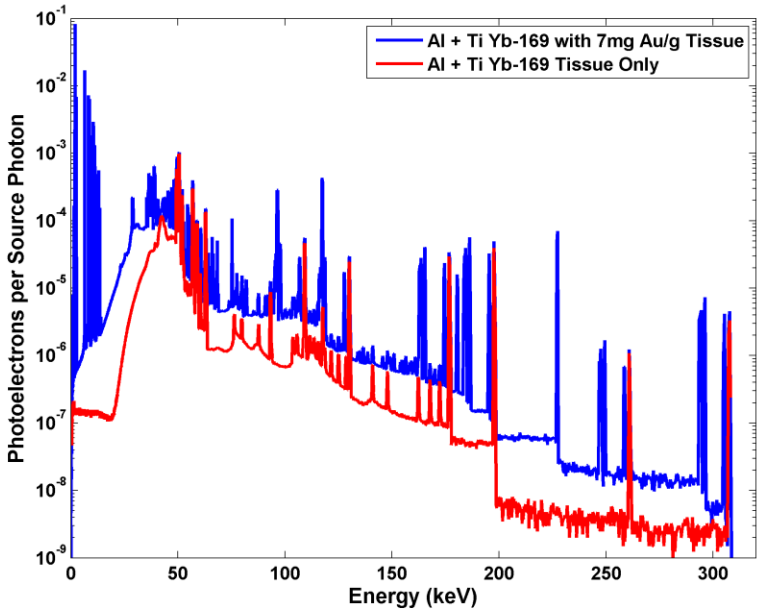

Figure A.2 Spectrum of photoelectrons released in the tumor region for the aluminum and titanium design encapsulation design.

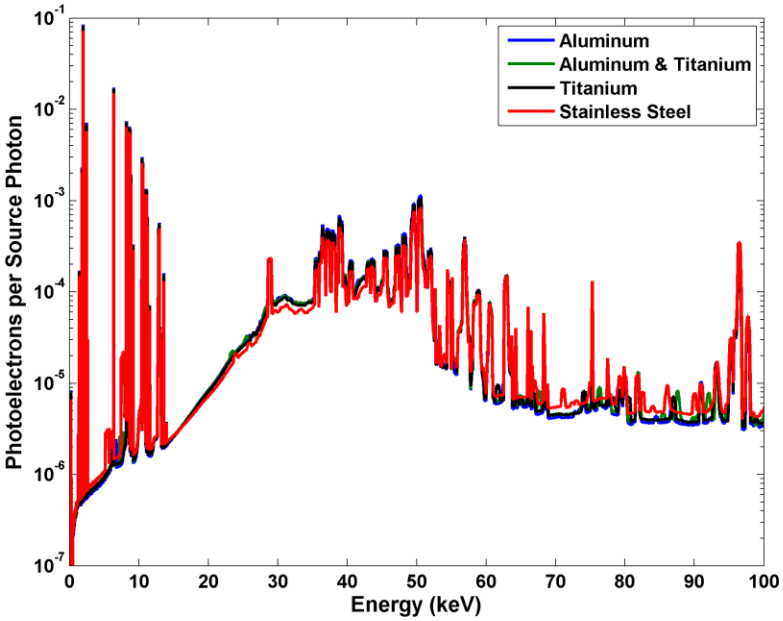

Figure A.3 Spectrum of photoelectrons released in the tumor region for the all encapsulation designs. The figure shows the spectra from gold and tissue for the tumor loaded with 7 mg Au/g tissue and from tissue only from 0.025 keV up to 100 keV. The pattern of photoelectrons for each source design is very similar with some differences noticed in the region below 100 keV. The aluminum, aluminum/titanium and titanium designs consistently show improved photoelectron yield throughout this region when compared with stainless steel.

APPENDIX B
RECONSTRUCTED INCIDENT SPECTRA OF PHILLIPS RT-250 ORTHOVOLTAGE MACHINE

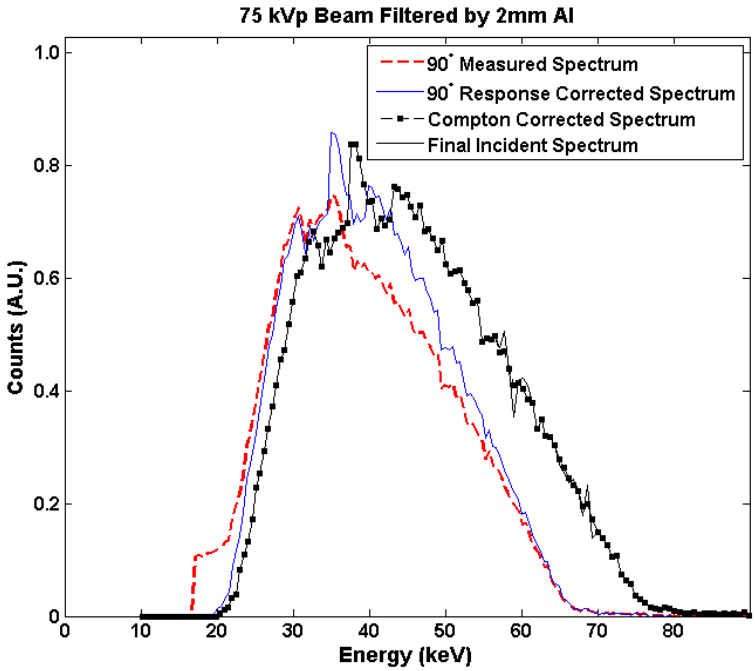

Figure B.1 Measured 90° spectrum and reconstructed incident spectrum for the 75 kVp.

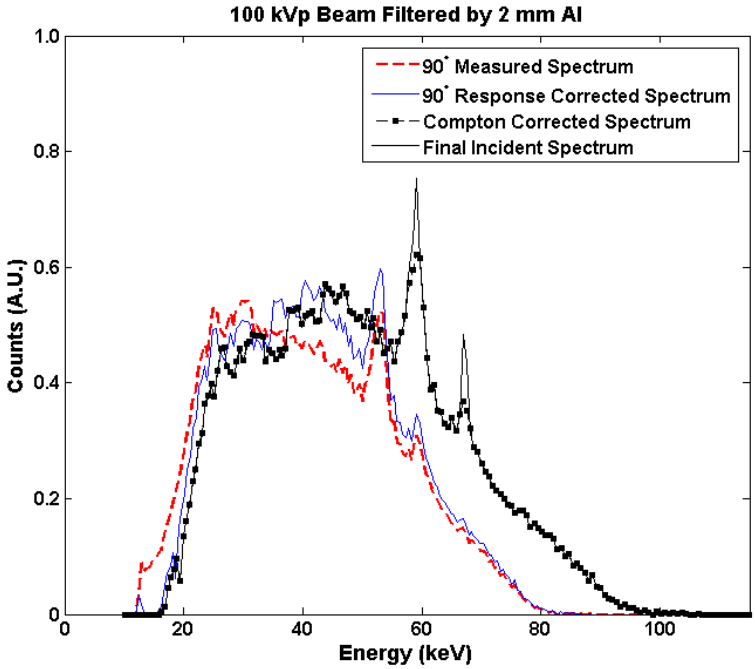

Figure B.2 Measured 90° spectrum and reconstructed incident spectrum for the 75 kVp.

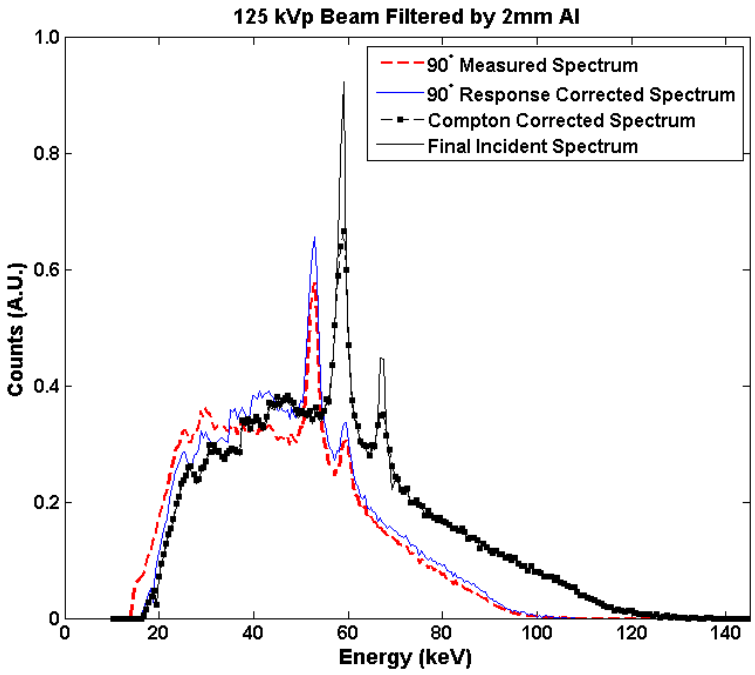

Figure B.3 Measured 90^{o} spectrum and reconstructed incident spectrum for the 125 kVp.

REFERENCES

[1] G. F. Paciotti, L. Myer, D. Weinreich, D. Goia, N. Pavel, R. E. McLaughlin, *et al.*, "Colloidal gold: a novel nanoparticle vector for tumor directed drug delivery," *Drug Deliv,* vol. 11, pp. 169-83, May-Jun 2004.

[2] K. Sokolov, M. Follen, J. Aaron, I. Pavlova, A. Malpica, R. Lotan, *et al.*, "Real-time vital optical imaging of precancer using anti-epidermal growth factor receptor antibodies conjugated to gold nanoparticles," *Cancer Research,* vol. 63, p. 1999, 2003.

[3] X. Qian, X. H. Peng, D. O. Ansari, Q. Yin-Goen, G. Z. Chen, D. M. Shin, *et al.*, "In vivo tumor targeting and spectroscopic detection with surface-enhanced Raman nanoparticle tags," *Nat Biotechnol,* vol. 26, pp. 83-90, Jan 2008.

[4] J. Hainfeld, D. Slatkin, T. Focella, and H. Smilowitz, "Gold nanoparticles: a new X-ray contrast agent," *British Journal of Radiology,* vol. 79, p. 248, 2006.

[5] L. R. Hirsch, R. J. Stafford, J. A. Bankson, S. R. Sershen, B. Rivera, R. E. Price, *et al.*, "Nanoshell-mediated near-infrared thermal therapy of tumors under magnetic resonance guidance," *Proc Natl Acad Sci U S A,* vol. 100, pp. 13549-54, Nov 11 2003.

[6] G. von Maltzahn, J. Park, A. Agrawal, N. Bandaru, S. Das, M. Sailor, *et al.*, "Computationally guided photothermal tumor therapy using long-circulating gold nanorod antennas," *Cancer research,* vol. 69, p. 3892, 2009.

[7] S. Krishnan, P. Diagaradjane, and S. H. Cho, "Nanoparticle-mediated thermal therapy: Evolving strategies for prostate cancer therapy," *International Journal of Hyperthermia,* pp. 1-15, 2010.

[8] P. Diagaradjane, A. Shetty, J. C. Wang, A. M. Elliott, J. Schwartz, S. Shentu, *et al.*, "Modulation of in vivo tumor radiation response via gold nanoshell-mediated vascular-focused hyperthermia: characterizing an integrated antihypoxic and localized vascular disrupting targeting strategy," *Nano Lett,* vol. 8, pp. 1492-500, May 2008.

[9] J. F. Hainfeld, F. A. Dilmanian, D. N. Slatkin, and H. M. Smilowitz, "Radiotherapy enhancement with gold nanoparticles," *J Pharm Pharmacol,* vol. 60, pp. 977-85, Aug 2008.

[10] J. F. Hainfeld, F. A. Dilmanian, Z. Zhong, D. N. Slatkin, J. A. Kalef-Ezra, and H. M. Smilowitz, "Gold nanoparticles enhance the radiation therapy of a murine squamous cell carcinoma," *Phys Med Biol,* vol. 55, pp. 3045-59, Jun 7 2010.

[11] J. F. Hainfeld, D. N. Slatkin, and H. M. Smilowitz, "The use of gold nanoparticles to enhance radiotherapy in mice," *Phys Med Biol,* vol. 49, pp. N309-15, Sep 21 2004.

[12] S. H. Cho, "Estimation of tumour dose enhancement due to gold nanoparticles during typical radiation treatments: a preliminary Monte Carlo study," *Phys Med Biol,* vol. 50, pp. N163-73, Aug 7 2005.

[13] S. H. Cho, B. L. Jones, and S. Krishnan, "The dosimetric feasibility of gold nanoparticle-aided radiation therapy (GNRT) via brachytherapy using low-energy gamma-/x-ray sources," *Phys Med Biol,* vol. 54, pp. 4889-905, Aug 21 2009.

[14] B. L. Jones, S. Krishnan, and S. H. Cho, "Estimation of microscopic dose enhancement factor around gold nanoparticles by Monte Carlo calculations," *Medical Physics,* vol. 37, pp. 3809-16, Jul 2010.

[15] H. F. Dvorak, J. A. Nagy, J. T. Dvorak, and A. M. Dvorak, "Identification and characterization of the blood vessels of solid tumors that are leaky to circulating macromolecules," *Am J Pathol,* vol. 133, pp. 95-109, Oct 1988.

[16] S. Unezaki, K. Maruyama, J. Hosoda, I. Nagae, Y. Koyanagi, M. Nakata, *et al.*, "Direct measurement of the extravasation of polyethyleneglycol-coated liposomes into solid tumor tissue by in vivo fluorescence microscopy," *International Journal of Pharmaceutics,* vol. 144, pp. 11-17, Nov 22 1996.

[17] H. Maeda, J. Fang, T. Inutsuka, and Y. Kitamoto, "Vascular permeability enhancement in solid tumor: various factors, mechanisms involved and its implications," *Int Immunopharmacol,* vol. 3, pp. 319-28, Mar 2003.

[18] F. H. Adams, A. Norman, R. S. Mello, and D. Bass, "Effect of Radiation and Contrast-Media on Chromosomes - Preliminary-Report," *Radiology,* vol. 124, pp. 823-826, 1977.

[19] R. S. Mello, H. Callisen, J. Winter, A. R. Kagan, and A. Norman, "Radiation-Dose Enhancement in Tumors with Iodine," *Medical Physics,* vol. 10, pp. 75-78, 1983.

[20] P. Dawson, M. Penhaligon, E. Smith, and J. Saunders, "Iodinated Contrast Agents as Radiosensitizers," *British Journal of Radiology,* vol. 60, pp. 201-203, Feb 1987.

[21] K. S. Iwamoto, S. T. Cochran, J. Winter, E. Holburt, R. T. Higashida, and A. Norman, "Radiation-Dose Enhancement Therapy with Iodine in Rabbit Vx-2 Brain-Tumors," *Radiotherapy and Oncology,* vol. 8, pp. 161-170, Feb 1987.

[22] J. H. Rose, A. Norman, M. Ingram, C. Aoki, T. Solberg, and A. Mesa, "First radiotherapy of human metastatic brain tumors delivered by a computerized tomography scanner (CTRx)," *Int J Radiat Oncol Biol Phys,* vol. 45, pp. 1127-32, Dec 1 1999.

[23] A. V. Mesa, A. Norman, T. D. Solberg, J. J. Demarco, and J. B. Smathers, "Dose distributions using kilovoltage x-rays and dose enhancement from iodine contrast agents," *Phys Med Biol,* vol. 44, pp. 1955-68, Aug 1999.

[24] J. L. Robar, S. A. Riccio, and M. A. Martin, "Tumour dose enhancement using modified megavoltage photon beams and contrast media," *Phys Med Biol,* vol. 47, pp. 2433-49, Jul 21 2002.

[25] F. Verhaegen, B. Reniers, F. Deblois, S. Devic, J. Seuntjens, and D. Hristov, "Dosimetric and microdosimetric study of contrast-enhanced radiotherapy with kilovolt x-rays," *Phys Med Biol,* vol. 50, pp. 3555-69, Aug 7 2005.

[26] J. L. Robar, "Generation and modelling of megavoltage photon beams for contrast-enhanced radiation therapy," *Phys Med Biol,* vol. 51, pp. 5487-504, Nov 7 2006.

[27] B. Jones, "Development of dosimetry and imaging techniques for pre-clinical studies of gold nanoparticle-aided radiation therapy," PhD, Nuclear and Radiological Engineering, Georgia Institute of Technology, Atlanta, GA, 2011.

[28] J. C. Roeske, L. Nunez, M. Hoggarth, E. Labay, and R. R. Weichselbaum, "Characterization of the theorectical radiation dose enhancement from nanoparticles," *Technol Cancer Res Treat,* vol. 6, pp. 395-401, Oct 2007.
[29] D. L. Mason, J. J. Battista, R. B. Barnett, and A. T. Porter, "Ytterbium-169: calculated physical properties of a new radiation source for brachytherapy," *Medical Physics,* vol. 19, pp. 695-703, May-Jun 1992.
[30] R. K. Das, V. Mishra, H. Perera, A. S. Meigooni, and J. F. Williamson, "A secondary air kerma strength standard for Yb-169 interstitial brachytherapy sources," *Phys Med Biol,* vol. 40, pp. 741-56, May 1995.
[31] A. Piermattei, L. Azario, G. Rossi, A. Soriani, G. Arcovito, R. Ragona, *et al.*, "Dosimetry of 169 Yb seed model X1267," *Phys Med Biol,* vol. 40, pp. 1317-30, Aug 1995.
[32] S. M. Loft, I. P. Coles, and R. G. Dale, "The potential of ytterbium 169 in brachytherapy: a brief physical and radiobiological assessment," *Br J Radiol,* vol. 65, pp. 252-7, Mar 1992.
[33] H. Perera, J. F. Williamson, Z. Li, V. Mishra, and A. S. Meigooni, "Dosimetric characteristics, air-kerma strength calibration and verification of Monte Carlo simulation for a new Ytterbium-169 brachytherapy source," *Int J Radiat Oncol Biol Phys,* vol. 28, pp. 953-70, Mar 1 1994.
[34] M. S. MacPherson and J. J. Battista, "Dose distributions and dose rate constants for new ytterbium-169 brachytherapy seeds," *Medical Physics,* vol. 22, pp. 89-96, Jan 1995.
[35] A. Piermattei, L. Azario, and P. Montemaggi, "Implantation guidelines for 169 Yb seed interstitial treatments," *Phys Med Biol,* vol. 40, pp. 1331-8, Aug 1995.
[36] G. Lymperopoulou, P. Papagiannis, A. Angelopoulos, P. Karaiskos, E. Georgiou, and D. Baltas, "A dosimetric comparison of 169Yb and 192Ir for HDR brachytherapy of the breast, accounting for the effect of finite patient dimensions and tissue inhomogeneities," *Medical Physics,* vol. 33, pp. 4583-9, Dec 2006.
[37] D. C. Medich, M. A. Tries, and J. J. Munro III, "Monte Carlo characterization of an ytterbium-169 high dose rate brachytherapy source with analysis of statistical uncertainty," *Medical Physics,* vol. 33, pp. 163-72, Jan 2006.
[38] G. R. Lazarescu and J. J. Battista, "Analysis of the radiobiology of ytterbium-169 and iodine-125 permanent brachytherapy implants," *Phys Med Biol,* vol. 42, pp. 1727-36, Sep 1997.
[39] G. Lymperopoulou, P. Papagiannis, L. Sakelliou, N. Milickovic, S. Giannouli, and D. Baltas, "A dosimetric comparison of 169Yb versus 192Ir for HDR prostate brachytherapy," *Medical Physics,* vol. 32, pp. 3832-42, Dec 2005.
[40] S. H. Cho, R. Muller-Runkel, and W. F. Hanson, "Determination of the tissue attenuation factor along two major axes of a high dose rate (HDR) 192Ir source," *Medical Physics,* vol. 26, pp. 1492-7, Aug 1999.
[41] M. J. Cazeca, D. C. Medich, and J. J. Munro III, "Monte Carlo characterization of a new Yb-169 high dose rate source for brachytherapy application," *Medical Physics,* vol. 37, pp. 1129-36, Mar 2010.

[42] D. C. Medich and J. J. Munro III, "Dependence of Yb-169 absorbed dose energy correction factors on self-attenuation in source material and photon buildup in water," *Medical Physics*, vol. 37, pp. 2135-44, May 2010.

[43] K. J. Son, J. S. Lee, U. J. Park, S. B. Hong, K. S. Seo, and H. S. Han, "Development of miniature radiation sources for medical and non-destructive testing applications," in *Production techniques and quality control of sealed radioactive sources of palladium-103, iodine-125, iridium-192 and ytterbium-169*. vol. IAEA-TECDOC-1512, ed Vienna: International Atomic Energy Agency, 2006.

[44] *Production Techniques and Quality Control of Sealed Radioactive Sources of Palladium-103, Iodine-125, Iridium-192 and Ytterbium-169*. Vienna: IAEA, 2006.

[45] R. B. Firestone and L. P. Ekström. (2004). *The Lund/LBNL Nuclear Data Search, Database Version 2.1, January 2004*.

[46] ICRU, "Tissue substitutes in radiation dosimetry and measurement," in *ICRU Report 44*, ed. Bethesda, MD: ICRU, 1989.

[47] X.-M. C. Team, "MCNP-A General Monte Carlo N-Particle Transport Code," 5 LA-UR-03-1987 ed. Los Alamos, NM, 2003.

[48] I. Kawrakow and D. Rogers, "The EGSnrc code system: Monte Carlo simulation of electron and photon transport," 2000.

[49] B. Walters, I. Kawrakow, and D. Rogers, "DOSXYZnrc users manual," *NRC Report PIRS*, vol. 794, 2005.

[50] W. R. Nelson, H. Hirayama, and D. W. O. Rogers, *The EGS4 Code System*. Stanford, California: Stanford Linear Accelerator Center, 1985.

[51] V. A. Semenenko, J. E. Turner, and T. B. Borak, "NOREC, a Monte Carlo code for simulating electron tracks in liquid water," *Radiation and Environmental Biophysics*, vol. 42, pp. 213-217, 2003/10/01 2003.

[52] T. S. Piwonka, *Casting Design and Quality Assurance: Metals Handbook Desk Edition*, Second Edition ed.: ASM International, 2004.

[53] M. J. Rivard, B. M. Coursey, L. A. DeWerd, W. F. Hanson, M. S. Huq, G. S. Ibbott, *et al.*, "Update of AAPM Task Group No. 43 Report: A revised AAPM protocol for brachytherapy dose calculations," *Medical Physics*, vol. 31, pp. 633-74, Mar 2004.

[54] G. Luxton and G. Jozsef, "Radial dose distribution, dose to water and dose rate constant for monoenergetic photon point sources from 10 keV to 2 MeV:EGS4 Monte Carlo model calculation," *Medical Physics*, vol. 26, pp. 2531-8, Dec 1999.

[55] R. K. Das, A. S. Meigooni, V. Misha, M. A. Langton, and J. F. Williamson, "Dosimetric characteristics of the Type 8 Ytterbium-169 interstitial brachytherapy source," *J. Brachytherapy Int.*, vol. 13, pp. 219-234, 1997.

[56] E. Mainegra, R. Capote, and E. Lopez, "Dose rate constants for I-125, Pd-103, Ir-192 and Yb-169 brachytherapy sources: an EGS4 Monte Carlo study," *Phys Med Biol*, vol. 43, pp. 1557-1566, Jun 1998.

[57] K. Babcock, N. Sidhu, V. Kundapur, and K. Ali, "Collimator design for experimental minibeam radiation therapy," *Med Phys*, vol. 38, pp. 2192-7, Apr 2011.

[58] G. Poludniowski, G. Landry, F. DeBlois, P. M. Evans, and F. Verhaegen, "SpekCalc: a program to calculate photon spectra from tungsten anode x-ray tubes," *Phys Med Biol,* vol. 54, pp. N433-8, Oct 7 2009.
[59] G. G. Poludniowski, "Calculation of x-ray spectra emerging from an x-ray tube. Part II. X-ray production and filtration in x-ray targets," *Med Phys,* vol. 34, pp. 2175-86, Jun 2007.
[60] G. G. Poludniowski and P. M. Evans, "Calculation of x-ray spectra emerging from an x-ray tube. Part I. electron penetration characteristics in x-ray targets," *Med Phys,* vol. 34, pp. 2164-74, Jun 2007.
[61] M. Yaffe, K. W. Taylor, and H. E. Johns, "Spectroscopy of diagnostic x rays by a Compton-scatter method," *Medical Physics,* vol. 3, pp. 328-334, 1976.
[62] G. Matscheko and G. A. Carlsson, "Compton spectroscopy in the diagnostic X-ray energy range: I. Spectrometer design," *Phys Med Biol,* vol. 34, p. 185, 1989.
[63] G. Matscheko, G. A. Carlsson, and R. Ribberfors, "Compton spectroscopy in the diagnostic X-ray energy range: II. Effects of scattering material and energy resolution," *Phys Med Biol,* vol. 34, p. 199, 1989.
[64] G. Matscheko and R. Ribberfors, "A Compton scattering spectrometer for determining X-ray photon energy spectra," *Phys Med Biol,* vol. 32, p. 577, 1987.
[65] K. Maeda, M. Matsumoto, and A. Taniguchi, "Compton-scattering measurement of diagnostic x-ray spectrum using high-resolution Schottky CdTe detector," *Medical Physics,* vol. 32, pp. 1542-1547, 2005.
[66] *Photoemission in Solids I: General Principles*: Springer-Verlag, Berlin, 1978.
[67] E. Merzbacher, *Quantum Mechanics*: Wiley, 1998.
[68] M. J. Butson, T. Cheung, and P. K. N. Yu, "Weak energy dependence of EBT gafchromic film dose response in the 50 kVp–10 MVp X-ray range," *Applied Radiation and Isotopes,* vol. 64, pp. 60-62, 2006.
[69] B. Arjomandy, R. Tailor, A. Anand, N. Sahoo, M. Gillin, K. Prado, *et al.*, "Energy dependence and dose response of Gafchromic EBT2 film over a wide range of photon, electron, and proton beam energies," *Medical Physics,* vol. 37, pp. 1942-1947, 2010.
[70] M. Martišíková, B. Ackermann, and O. Jäkel, "Analysis of uncertainties in Gafchromic® EBT film dosimetry of photon beams," *Phys Med Biol,* vol. 53, p. 7013, 2008.
[71] S. Devic, N. Tomic, C. G. Soares, and E. B. Podgorsak, "Optimizing the dynamic range extension of a radiochromic film dosimetry system," *Medical Physics,* vol. 36, pp. 429-437, 2009.
[72] B. Arjomandy, R. Tailor, L. Zhao, and S. Devic, "EBT2 film as a depth-dose measurement tool for radiotherapy beams over a wide range of energies and modalities," *Medical Physics,* vol. 39, pp. 912-921, 2012.
[73] C.-M. Ma, C. W. Coffey, L. A. DeWerd, C. Liu, R. Nath, S. M. Seltzer, *et al.*, "AAPM protocol for 40–300 kV x-ray beam dosimetry in radiotherapy and radiobiology," *Medical Physics,* vol. 28, pp. 868-893, 2001.
[74] C. A. Schneider, W. S. Rasband, and K. W. Eliceiri, "NIH Image to ImageJ: 25 years of image analysis," *Nat Meth,* vol. 9, pp. 671-675, 2012.

[75] S. Beaman, S. C. Lillicrap, and J. L. Price, "Tungsten anode tubes with K-edge filters for mammography," *Br J Radiol,* vol. 56, pp. 721-7, Oct 1983.
[76] C. P. McDonagh, J. L. Leake, and S. A. Beaman, "Optimum x-ray spectra for mammography: choice of K-edge filters for tungsten anode tubes," *Phys Med Biol,* vol. 29, pp. 249-52, Mar 1984.
[77] R. J. Jennings, R. J. Eastgate, M. P. Siedband, and D. L. Ergun, "Optimal x-ray spectra for screen-film mammography," *Medical Physics,* vol. 8, pp. 629-39, Sep-Oct 1981.